

POLITECNICO DI TORINO

Corso di Laurea Magistrale in Ingegneria Meccanica

Tesi di Laurea Magistrale



Calibration of a Low Temperature Lean NO_x Trap model for light-duty diesel engine exhaust aftertreatment applications

Relatore:

Prof. Federico Millo – Dipartimento Energia (DENERG)

Tutor Aziendali:

Claudio Cubito, Ph.D. – Punch Torino S.P.A

Paolo Ferreri – Punch Torino S.P.A

Marcello Rimondi – Punch Torino S.P.A

Candidato:
James Romagnolo

Anno Accademico 2019/2020

Non serve a niente rifugiarsi nei sogni e dimenticarsi di vivere

Albus Silente

Ringraziamenti

Voglio dedicare il risultato di questo lavoro a tutti coloro che mi sono stati vicini e mi hanno sostenuto nel corso di questi anni di studi, in particolar modo a mia madre, che, con il suo supporto costante, mi ha permesso di raggiungere questo obiettivo. Inoltre, voglio ringraziare Francesca, che mi ha accompagnato durante buona parte del percorso universitario permettendomi di affrontarlo con maggiore serenità.

Infine, voglio esprimere la mia riconoscenza al Prof. Federico Millo e a Marcello Rimondi per avermi permesso di effettuare questo lavoro in un ambiente professionale e stimolante, e a Claudio Cubito e Paolo Ferreri per tutto l'aiuto che mi hanno dato durante lo svolgimento della tesi.

Acknowledgments

I want to dedicate the result of this work to all those who have supported me during these years of studies, especially to my mother, who, with her constant support, has allowed me to achieve this goal. Furthermore, I want to thank Francesca, who accompanied me during a considerable part of my university career, enabling me to face with it with greater serenity.

Finally, I want to express my gratitude to Prof. Federico Millo and Marcello Rimondi for allowing me to perform this study in a professional and stimulating working environment, and to Claudio Cubito and Paolo Ferreri for all the help they gave me during the development of this thesis.

Sommario

Al giorno d'oggi, l'inasprimento dei limiti di inquinanti provenienti da veicoli dotati di motore a combustione interna ha spinto la ricerca nel campo delle tecnologie di post-trattamento dei gas combusti. Le nuove legislazioni hanno posto particolare enfasi nella riduzione degli ossidi di azoto (NO_x). Il rispetto dei nuovi standard sulle emissioni di inquinanti richiede l'uso di sistemi complessi, spesso composti da diverse tecnologie catalitiche. In particolare, ha assunto una certa rilevanza lo sviluppo di catalizzatori atti alla riduzione di NO_x , quali Selective Catalytic Reduction (SCR) e Lean NO_x Traps (LNT). Considerati gli elevati costi e l'elevato dispendio di tempo di un approccio di tipo sperimentale per la progettazione e l'ottimizzazione di questi sistemi, l'utilizzo di modelli di simulazione, con tutti i loro benefici, è considerato una valida alternativa.

Questo studio si concentra sullo sviluppo di un modello Low Temperature (LT) LNT 1D, con un approccio cinetico globale che simula le principali reazioni che si verificano sulla superficie del washcoat. Il modello conta quarantuno reazioni, che cercano di descrivere i principali fenomeni chimici che avvengono nel catalizzatore: ossidazione del monossido di carbonio (CO), idrocarburi (HC) e idrogeno (H_2), reazioni di water gas shift (WGS) e di steam reforming (SR), conversione di NO in NO_2 , assorbimento di NO_x e O_2 e la loro riduzione mediante H_2 , CO e C_3H_6 . La cinetica del modello è stata calibrata sulla base di diversi esperimenti eseguiti con l'ausilio di un Synthetic Gas Bench (SGB). L'ossidazione di specie ricche è stata studiata mediante esperimenti di Light-Off (LO), in cui una rampa di temperatura permette l'attivazione del campione di catalizzatore. Lo storage dell'ossigeno è stato testato con tests di Oxygen Storage Capacity (OSC), con temperatura costante e alternanza di atmosfere magre e ricche. Il comportamento per quanto riguarda l'assorbimento di NO_x è stato valutato tramite esperimenti di Temperature Programmed Desorption (TPD), in cui l'assorbimento isoterma è seguito da una rampa di temperatura fino al completo rilascio delle specie assorbite. Infine, la rigenerazione della trappola è stata testata attraverso esperimenti di NO_x Storage and Reduction (NSR), in cui è stata eseguita una serie di cicli magri/ricchi a temperatura costante. Il modello chimico così ottenuto è stato validato sulla base di cicli guida (WLTC e RDE) misurati al banco prova sul componente full-scale. I risultati della simulazione sottolineano l'applicabilità del modello su un'ampia gamma di condizioni operative, mostrando l'idoneità dell'approccio modellistico scelto.

Inoltre, l'analisi dei dati SGB, utilizzati per la calibrazione del modello, ha evidenziato alcuni limiti nella caratterizzazione delle prestazioni del catalizzatore e delle proprietà termiche. Il confronto dei risultati sperimentali di TPD e NSR ha mostrato disaccordo tra i due meccanismi di assorbimento. Queste incongruenze sono principalmente dovute a fenomeni di disattivazione catalitica inattesi, che si verificano durante esperimenti di assorbimento di NO_x su ampia scala temporale, come i TPD. L'indagine e la soluzione di questi problemi può essere un buono spunto per ulteriori miglioramenti nelle attività sperimentali SGB svolte con

l'obiettivo di ottenere dati ancora più affidabili per la calibrazione di modelli di post-trattamento dei gas di scarico.

Abstract

Nowdays, the tightening of motorized vehicles pollutant limits has boosted the research in the aftertreatment technologies field. New legislations posed particular emphasis in the reduction of nitrogen oxides (NO_x). The fulfillment of these emission standards expects the use of complex systems, always composed of several catalyst technologies. In particular, the development of catalysts suitable for NO_x reduction, such as Selective Catalytic Reduction (SCR) catalysts and Lean NO_x Traps (LNT) catalysts, assumed a certain relevance. Considering the high costs and time consumption of an experimental approach for the designing and optimization of these systems, the use of simulation models, with all its benefits, is considered as a valid alternative.

This work focuses on the development of a 1D Low Temperature (LT) LNT model, with a global kinetic approach describing all the reactions occurring on the washcoat surface. Forty-one reactions are considered, trying to describe all main processes in the catalyst: oxidation of carbon monoxide (CO), hydrocarbons (HC) and hydrogen (H_2), water gas shift (WGS) and steam reforming (SR) reactions, NO to NO_2 conversion, O_2 and NO_x storage and the consequent reduction of these ones by means of H_2 , CO and C_3H_6 . The chemical kinetics was calibrated on the base of several experiments on a Synthetic Gas Bench (SGB). The oxidation of rich species was investigated through Light-Off (LO) experiments, where a temperature ramp activates the catalyst core sample. The oxygen storage was tested with Oxygen Storage Capacity (OSC) tests, with constant temperature and lean/rich cycling. The NO_x storage behavior was evaluated through Temperature Programmed Desorption (TPD) experiments, where the isothermal adsorption is followed by a temperature ramp until complete release of stored species. Finally, the regeneration of the trap was tested through NO_x Storage and Reduction (NSR) experiments, where a series of lean/rich cycles was performed at constant temperature. The validation of the full-size LT-LNT model was done based on chassis dyno measurements over the WLTC and the RDE cycles. The simulation results underline the applicability of the model over a wide range of operating conditions, showing the suitability of the chosen modelling approach.

Furthermore, the analysis of SGB data, used for the model calibration, highlighted some limits in the characterization of catalyst performances and thermal properties. The comparison of TPD and NSR experimental results showed disagreement between the two storage behaviors. These incongruences are mostly due to unexpected deactivating phenomena occurring during long time scale NO_x adsorption experiments, such as TPDs. The investigation and solution of these problems can be a good insight for further improvements in SGB experimental activities performed with the aim to obtain even more reliable data for exhaust aftertreatment model calibration.

Contents

1	INTRODUCTION	27
1.1	Legislative framework for fuel economy and pollutant emission.....	27
1.1.1	North America.....	27
1.1.2	Europe.....	31
1.2	Technological path to reduce NO _x emissions.....	36
1.3	LNT technology.....	40
1.3.1	Overview	40
2	Experimental activity	50
2.1	Steady state tests.....	51
2.1.1	LO tests	51
2.1.2	OSC tests.....	53
2.1.3	TPD tests	56
2.1.4	NSR Tests.....	58
2.2	Transient tests	60
3	LT-LNT modeling and calibration.....	62
3.1	Modeling approach for automotive catalysts.....	62
3.2	Aftertreatment 1-D modeling	63
3.2.1	Thermal modeling.....	63
3.2.2	Chemical modeling.....	64
3.3	Calibration procedure.....	65
3.3.1	Reactions over PGM sites	66
3.3.2	Storage and oxidation reactions over Cerium sites	73
3.3.3	NO _x storage on LT-LNT	76
3.3.4	NO _x reduction.....	83

4	Model assessment	93
4.1	Model assessment on SGB tests (reactor scale component).....	93
4.1.1	Thermal model.....	93
4.1.2	LO assessment	94
4.1.3	OSC assessment.....	97
4.1.4	NO _x adsorption and desorption assessment	100
4.1.5	NO _x reduction assessment.....	109
4.2	Model assessment on full scale tests.....	124
4.2.1	WLTP cycles results	124
4.2.2	RDE cycles results.....	128
5	Conclusions	133
6	References	134

List of Figures

Figure 1 - Overview of pollutant regulations in Europe and North America for light duty passenger cars [1].....	27
Figure 2 - FTP75, US06 and SC03 driving cycles for type approval tests [2].....	29
Figure 3 - Comparison between NEDC, WLTC and RDE cycles vehicle acceleration VS vehicle speed points [5].....	32
Figure 4 - Comparison between NEDC (left) and WLTC (right) vehicle speed profiles [5].	33
Figure 5 - Example of an RDE test cycle recorded during road testing [2].....	34
Figure 6 - Possible applicable configurations to comply with light duty passenger cars Euro 6b (figures a, b) and Euro 6d (figure c) pollutant limits [8].	37
Figure 7 - Possible aftertreatment configuration to achieve ULN emissions [14].	39
Figure 8 - Possible aftertreatment configuration to achieve ULN emissions [15].	39
Figure 9 - Possible aftertreatment configuration to achieve ULN emissions [15].	40
Figure 10 - NO _x adsorption and desorption/reduction behaviors on a Pt-Ba/Al ₂ O ₃ based LNT catalyst [17].	41
Figure 11 - Bell shaped storage capacity dependency from temperature over a Pt/Ba based LNT catalyst [19].....	42
Figure 12 - NO _x release profile in a generic NSR catalyst [17].	45
Figure 13 - NSR test, performed at T = 200°C, SV = 30,000 1/h, 15 min lean (300 ppm NO, 10% O ₂ , 5% H ₂ O, 5% CO ₂ , balance N ₂), 10 min rich (625 ppm CO, 375 ppm H ₂ , 5% H ₂ O, 5% CO ₂ , balance N ₂) [17].	47
Figure 14 - Samples extraction from full scale LNT catalyst.	51
Figure 15 - CO and NMHC tailpipe traces during a generic light-off test.....	52
Figure 16 - Chemical behavior during a generic OSC test.	53
Figure 17 - Simplified example of NO and NO ₂ in/out traces during a TPD experiment. ..	56

Figure 18 - Generic NSR test behavior.	58
Figure 19 - Original inlet reductant trace (green dashed line) compared with experimental out reductant trace (blue continuous line). The red dashed line represents the inlet reductant profile after the valve dynamic correction.	60
Figure 20 - Volume discretization along component length [13].....	63
Figure 21 - Simplified representation of thermal intermediate approach modeling [40]. ..	64
Figure 22 - Arrhenius plot: red dots represent reaction rate in correspondence of different temperatures, the black line represents the interpolating line used by calibrator to match rates at all temperatures [40].....	66
Figure 23 - Example of a LO test with CO as inlet species. The green dashed line represents the inlet concentration, while the blue line the outlet one. The orange dotted line represents the temperature profile.	68
Figure 24 - Arrhenius terms associated to CO and HCs oxidation reactions. The red line represents the reaction rate for CO oxidation, the blue line depicts the C ₃ H ₆ one, the green line refers to C ₈ H ₁₀ oxidation rate and the pink line illustrates the oxidation rate for C ₁₂ H ₂₆	69
Figure 25 - Arrhenius plot for NO oxidation reaction, medium concentrations of NO in the inlet feeding gas.	70
Figure 26 - Arrhenius plot for WGS reaction.....	72
Figure 27 - Arrhenius plot for SR reaction.....	73
Figure 28 - Example of two OSC tests: with CO as reductant, performed at 300°C (573°K) (left) and with C ₃ H ₆ , performed at 400°C (right). The green line represents the CO inlet concentration, while the blue line the outlet one. The orange dotted line represents the temperature profile.....	74
Figure 29 - Arrhenius plot for C ₃ H ₆ (blue) and CO (red) oxidation through O ₂ stored on the catalyst. The dotted lines represent the Arrhenius term in lean conditions (high percentages of O ₂ in the atmosphere), while continuous lines represent the Arrhenius term in rich conditions (no O ₂ in the atmosphere composition).....	76
Figure 30 - NO and NO ₂ experimental traces, Test 1: T=100°C, Test 5: T=150°C, Test 7: T=200°C, Test 13: T=250°C. Low SV conditions, NO medium concentration, NO ₂ /NO = 0. The green line represents the inlet NO concentration, while the red and blue ones represent	

respectively the NO and NO₂ outlet experimental traces. The orange line depicts the inlet temperature profile..... 78

Figure 31 - NO and NO₂ experimental traces, Test 24: T=300°C, Test 31: T=350°C, Test 32: T=400°C, Test 33: T=450°C. Low SV conditions, NO medium concentration, NO₂/NO = 0. The green line represents the inlet NO concentration, while the red and blue ones represent respectively the NO and NO₂ outlet experimental traces. The orange line depicts the inlet temperature profile..... 79

Figure 32 - Arrhenius terms of adsorption and desorption reactions associated to nitrite formation (Barium-II). The blue line represents the adsorption rate, while the red one the desorption rate. 80

Figure 33 - Arrhenius terms of adsorption and desorption reactions associated to nitrate formation (Barium-I), the continuous blue line corresponds to adsorption rate with associated coverage equal to zero, while the dashed one corresponds to full site. The red line represents the desorption rate..... 81

Figure 34 - Arrhenius terms of adsorption and desorption reactions associated to nitrate formation (Barium-III). The blue line represents the adsorption rate, while the red one the desorption rate. 82

Figure 35 - Arrhenius terms for NO (blue) and NO₂ (red) desorption related to Barium-I and Barium-III sites in lean conditions (continuous lines) and in rich conditions, with high concentrations of C₃H₆ (dashed lines), where inhibition function G24 increase the rate.... 83

Figure 36 - NSR Test 3 (a), at T=200°C, and Test 9 (b), at T=350°C, C₃H₆ as reductant (see Table 14). The blue continuous lines represent the NO outlet concentration traces, while the green dashed ones the inlet NO concentration profiles..... 86

Figure 37 - NSR Test 2 (a), at T=200°C, and Test 8 (b), at T=350°C, CO as reductant (see Table 14). The blue continuous lines represent the NO outlet concentration traces, while the green dashed ones the inlet NO concentration profiles..... 86

Figure 38 - Arrhenius plot for reduction reactions 35/36 (blue lines, related to Barium-I site), 37 (red line, related to Barium-II site) and 38/39 (green lines, related to Barium-III site), with C₃H₆ as reductant (see Table 21). The continuous lines refer to rate of reactions that lead to complete reduction of barium site with N₂ release, while the dashed ones represent the rate of partial nitrate/nitrite reduction with NO release..... 88

Figure 39 - Arrhenius plot for reduction reactions 30 (blue line, related to Barium-I site), 31/32 (red lines, related to Barium-II site) and 33 (green line, related to Barium-III site), with CO as reductant (see Table 21). The continuous lines refer to rate of reactions that lead to

complete reduction of barium site with N_2 release, while the dashed ones represent the rate of partial nitrate/nitrite reduction with NO release. 88

Figure 40 - NSR Test 1 (a), at $T=200^\circ C$, and Test 7 (b), at $T=350^\circ C$, H_2 as reductant (see Table 14). The blue continuous lines represent the NO experimental outlet concentration traces, while the green dashed ones the inlet NO experimental concentration profiles..... 89

Figure 41 - Arrhenius plot for reduction reactions 21 (blue line, related to Barium-I site), 22 (red line, related to Barium-II site) and 24 (green line, related to Barium-III site), with H_2 as reductant (see Table 21). 90

Figure 42 - Arrhenius plot for reduction reactions 25 (blue line, related to Barium-I site), 26/27 (red lines, related to Barium-II site) and 23/28 (green lines, related to Barium-III site), with CO as reductant (see Table 21). The continuous lines refer to rate of reactions that lead to complete reduction of barium site with N_2 release, while the dashed ones represent the rate of partial nitrate/nitrite reduction with NO release. 90

Figure 43 - Effect of inhibition function G17 on reduction reaction 33 of Table 21, in lean atmosphere with high percentages of oxygen. The blue dashed line represents the reduction reaction rate in lean conditions, while the continuous one is the rate profile in rich environments. 91

Figure 44 - N_2O out traces from NSR tests of Table 13: Test 1 at $T=200^\circ C$ (Left), Test 4 at $T=250^\circ C$ (Center), Test7 at $T=350^\circ C$ (Right). The blue lines represent the experimental outlet N_2O and the dashed green lines the inlet NO concentrations. 92

Figure 45 - Arrhenius plot for reduction reactions 29 (blue line, related to Barium-I site) with NH_3 as reductant, 34 (red line, related to Barium-I site) with CO as reductant and 41 (green line) with C_3H_6 as reductant (see Table 21). 92

Figure 46 - NSR Test 1 (red), at $T=200^\circ C$, Test 4 (blue), at $T=250^\circ C$, Test 7 (green), at $T=350^\circ C$, H_2 as reductant (see Table 14). Continuous lines represent the inlet experimental temperatures, while dashed ones represent outlet experimental temperatures. 93

Figure 47 - Example of differences between inlet (continuous lines) and outlet (dashed lines) temperatures for TPD tests. Comparison between experimental temperature traces (left) and between simulated temperature traces (right). All the traces showed refers to TPDs with only medium NO concentrations in lean environment as inlet feeding species (see Table 13)... 94

Figure 48 - CO and NMHC traces for Tests 1 - 3 - 6, performed at low Space Velocity. Boundary conditions are depicted in Table 11. The red lines refer to the simulated CO (left) and NMHC (right) outlet emissions, the blue lines to the experimental outlet ones, the green

dashed to the inlet emissions and the light orange dashed lines to the inlet temperature profiles..... 95

Figure 49 - CO and NMHC traces for Tests 2 - 5, performed at high Space Velocity. Boundary conditions are depicted in Table 11. The red lines refer to the simulated CO (left) and NMHC (right) outlet emissions, the blue lines to the experimental outlet ones, the green dashed to the inlet emissions and the light orange dashed lines to the inlet temperature profiles..... 95

Figure 50 - Test 9 - 12 - 14, NO in the feeding gas, low SV. CO/NMHC simulated traces from tests with same conditions but without NO in the feeding gas have been reported for comparison (pink dashed lines). Boundary conditions are depicted in Table 11. The red lines refer to the simulated outlet emissions, the blue lines to the experimental outlet ones, the green dashed to the inlet emissions and the orange dashed lines to the inlet temperature profiles..... 96

Figure 51 - OSC tests: 5 - 11 - 13 with C₃H₆ as reductant. The blue lines represent the average OSC estimated according the procedure from paragraph 2.1.2, while the red lines represents the simulated OSC. 97

Figure 52 - OSC tests: 4 - 10 - 12 with CO as reductant. The blue lines represent the average OSC estimated according the procedure from paragraph 2.1.2, while the red lines represent the simulated OSC. 98

Figure 53 - Zoom between 500s and 750s of OSC tests 1, 4, 10, 12, with CO as reductant. The red line represents the simulation output, the blue line the experimental output, the green dashed line the inlet experimental NO and the orange dashed line the LNT inlet temperature profile. 99

Figure 54 - Zoom between 500s and 750s of OSC tests 2, 5, 11 and between 1500s and 3000s of OSC test 13, with C₃H₆ as reductant. The red line represents the simulation output, the blue line the experimental output, the green dashed line the inlet experimental NO and the orange dashed line the LNT inlet temperature profile. 100

Figure 55 - TPD Test 1: T=100°C and Test 5: T=150°C, medium NO concentrations, low SV (see Table 13). NO (left) and NO₂ (right) traces. The red line represents the simulation output, the blue dashed line the experimental output, the green dashed line the inlet NO and the orange dashed line the LNT inlet temperature profile. 101

Figure 56 - Test 7: T=200°C and Test 13: T=250°C, medium NO concentrations, low SV (see Table 13). NO (left) and NO₂ (right) traces. The red line represents the simulation output, the blue dashed line the experimental output, the green dashed line the inlet NO and the orange dashed line the LNT inlet temperature profile. 102

Figure 57 - Test 24: T=300°C and Test 31: T=350°C, medium NO concentrations, low SV (see Table 13) . NO (left) and NO₂ (right) traces. The red line represents the simulation output, the blue dashed line the experimental output, the green dashed line the inlet NO and the orange dashed line the LNT inlet temperature profile. 103

Figure 58 - Test 32: T=400°C and Test 33: T=450°C, medium NO concentrations, low SV (see Table 13). NO (left) and NO₂ (right) traces. The red line represents the simulation output, the blue dashed line the experimental output, the green dashed line the inlet NO and the orange dashed line the LNT inlet temperature profile. 104

Figure 59 - Test 12: T=250°C and Test 23: T=275°C, medium NO concentrations, high SV (see Table 13). NO (left) and NO₂ (right) traces. The red line represents the simulation output, the blue dashed line the experimental output, the green dashed line the inlet NO and the orange dashed line the LNT inlet temperature profile. 105

Figure 60 - Test 18: T=250°C and Test 26: T=300°C, high NO concentrations, low SV (see Table 13). NO (left) and NO₂ (right) traces. The red line represents the simulation output, the blue dashed line the experimental output, the green dashed line the inlet NO and the orange dashed line the LNT inlet temperature profile..... 106

Figure 61 - Test 19: T=250°C and Test 25: T=300°C, low NO concentrations, low SV (see Table 13). NO (left) and NO₂ (right) traces. The red line represents the simulation output, the blue dashed line the experimental output, the green dashed line the inlet NO and the orange dashed line the LNT inlet temperature profile..... 106

Figure 62 - Test 3: T=125°C, Test 9: T=200°C and Test 20: T=250°C, low concentrations of NO and NO₂, low SV (see Table 13). NO (left) and NO₂ (right) traces. The red line represents the simulation output, the blue dashed line the experimental output, the green dashed line the inlet NO and the orange dashed line the LNT inlet temperature profile..... 107

Figure 63 - Test 4: T=125°C, Test 10: T=200°C and Test 21: T=250°C, medium NO concentrations, low concentrations of CO and HCs, low SV (see Table 13). NO (left) and NO₂ (right) traces. The red line represents the simulation output, the blue dashed line the experimental output, the green dashed line the inlet NO and the orange dashed line the LNT inlet temperature profile. 108

Figure 64 - Comparison between the NO loading phase sampled during TPD tests (Top) and NSR experiments (Bottom), with same atmosphere and temperature conditions. Red line is representative of simulated outlet NO, blue dashed line is the experimental outlet NO, green dashed line represents the inlet NO and orange dashed line is the inlet temperature profile. 110

Figure 65 - Comparison between the NO₂ loading phase sampled during TPD tests (Top) and NSR experiments (Bottom), with same atmosphere and temperature conditions. The red line represents the simulated outlet NO₂ emissions, the blue dashed line is referred to the experimental outlet NO₂ and the orange dashed line is the inlet temperature profile. 112

Figure 66 - CO (Left), NO (Center) and NO₂ (Right) out traces for NSR test 2 from Table 14, performed at T=200°C. Zoom in the 0-2000s time range. The red lines represent the simulated outlet emissions, the blue dashed ones the experimental outlet emissions and the dashed green lines the inlet concentrations. 113

Figure 67 - CO (Left), NO (Center) and NO₂ (Right) out traces for NSR test 2 from Table 14, performed at T=200°C. Zoom in the 0-800s time range. The red lines represent the simulated outlet emissions, the blue dashed ones the experimental outlet emissions and the dashed green lines the inlet concentrations. 114

Figure 68 - CO (Left), NO (Center) and NO₂ (Right) out traces for NSR test 5 from Table 14, performed at T=250°C. Zoom in the 0-3500s time range. The red lines represent the simulated outlet emissions, the blue dashed ones the experimental outlet emissions and the dashed green lines the inlet concentrations. 114

Figure 69 - CO (Left), NO (Center) and NO₂ (Right) out traces for NSR test 5 from Table 14, performed at T=250°C. Zoom in the 0-1400s time range. The red lines represent the simulated outlet emissions, the blue dashed ones the experimental outlet emissions and the dashed green lines the inlet concentrations. 115

Figure 70 - CO (Left), NO (Center) and NO₂ (Right) out traces for NSR test 8 from Table 14, performed at T=350°C. Zoom in the 0-2000s time range. The red lines represent the simulated outlet emissions, the blue dashed ones the experimental outlet emissions and the dashed green lines the inlet concentrations. 115

Figure 71 - CO (Left), NO (Center) and NO₂ (Right) out traces for NSR test 8 from Table 14, performed at T=350°C. Zoom in the 0-800s time range. The red lines represent the simulated outlet emissions, the blue dashed ones the experimental outlet emissions and the dashed green lines the inlet concentrations. 116

Figure 72 - NH₃ out traces from NSR tests of Table 14. From left to the right: Test 2 at T=200°C, Test 5 at T=250°C, Test8 at T=350°C. The red lines represent the simulated NH₃ outlet emissions, the blue dashed ones the experimental NH₃ outlet emissions and the dashed green lines the NO inlet concentrations. 116

Figure 73 - N₂O out traces from NSR tests of Table 14 at different inlet temperature. From left to the right: Test 2 at T=200°C, Test 5 at T=250°C, Test 8 at T=350°C. The red lines

represent the simulated N₂O outlet emissions, the blue dashed ones the experimental N₂O outlet emissions and the dashed green lines the inlet NO concentration. 117

Figure 74 - C₃H₆ (Left), NO (Center) and NO₂ (Right) out traces for NSR test 3 from Table 14, performed at T=200°C. Zoom in the 0-3000s time range. The red lines represent the simulated outlet emissions, the blue dashed ones the experimental outlet emissions and the dashed green lines the inlet concentrations. 117

Figure 75 - C₃H₆ (Left), NO (Center) and NO₂ (Right) out traces for NSR test 3 from Table 14, performed at T=200°C. Zoom in the 0-1000s time range. The red lines represent the simulated outlet emissions, the blue dashed ones the experimental outlet emissions and the dashed green lines the inlet concentrations. 118

Figure 76 - C₃H₆ (Left), NO (Center) and NO₂ (Right) out traces for NSR test 6 from Table 14, performed at T=250°C. Zoom in the 0-3500s time range. The red lines represent the simulated outlet emissions, the blue dashed ones the experimental outlet emissions and the dashed green lines the inlet concentrations. 118

Figure 77 - C₃H₆ (Left), NO (Center) and NO₂ (Right) out traces for NSR test 6 from Table 14, performed at T=250°C. Zoom in the 0-1200s time range. The red lines represent the simulated outlet emissions, the blue dashed ones the experimental outlet emissions and the dashed green lines the inlet concentrations. 119

Figure 78 - C₃H₆ (Left), NO (Center) and NO₂ (Right) out traces for NSR test 9 from Table 14, performed at T=350°C. Zoom in the 0-2000s time range. The red lines represent the simulated outlet emissions, the blue dashed ones the experimental outlet emissions and the dashed green lines the inlet concentrations. 119

Figure 79 - C₃H₆ (Left), NO (Center) and NO₂ (Right) out traces for NSR test 9 from Table 14 performed at T=350°C. Zoom in the 0-800s time range. The red lines represent the simulated outlet emissions, the blue dashed ones the experimental outlet emissions and the dashed green lines the inlet concentrations. 120

Figure 80 - NH₃ out traces for NSR test from Table 14: Test 3 at T=200°C (left), Test 6 at T=250°C (Center), Test 9 at T=350°C (Right). The red lines represent the simulated NH₃ outlet emissions, the blue dashed ones the experimental NH₃ outlet emissions and the dashed green lines the NO inlet concentrations. 120

Figure 81 - N₂O out traces from NSR tests of Table 14: Test 3 at T=200°C (Left), Test 6 at T=250°C (Center), Test 9 at T=350°C (Right). The red lines represent the simulated N₂O outlet emissions, the blue dashed ones the experimental N₂O outlet emissions and the dashed green lines the inlet NO concentrations. 121

Figure 82 - NO out traces for NSR test from Table 14: Test 1 at T=200°C (Left), Test 4 at T=250°C (Center), Test 7 at T=350°C (Right). The red lines represent the simulated outlet emissions, the blue dashed ones the experimental outlet emissions and the dashed green lines the inlet concentrations. 121

Figure 83 - NO₂ out traces for NSR test of Table 14: Test 1 at T=200°C (Right), Test 4 at T=250°C (Center), Test 7 at T=350°C (Left). The red lines represent the simulated outlet emissions, the blue dashed ones the experimental outlet emissions and the dashed green lines the inlet concentrations. 122

Figure 84 - NH₃ out traces from NSR tests of Table 14: Test 1 at T=200°C (Left), Test 4 at T=250°C (Center), Test7 at T=350°C (Right). The red lines represent the simulated NH₃ outlet emissions, the blue dashed ones the experimental NH₃ outlet emissions and the dashed green lines the NO inlet concentration..... 123

Figure 85 - N₂O out traces from NSR tests of Table 13: Test 1 at T=200°C (Left), Test 4 at T=250°C (Center), Test7 at T=350°C (Right). The red lines represent the simulated N₂O outlet emissions, the blue dashed ones the experimental N₂O outlet emissions and the dashed green lines the inlet NO concentrations. 123

Figure 86 - Comparison between simulated and experimental outlet temperatures referred to Cold WLTC 18. The red line is referred to the simulated trace, the blue dashed line to the experimental one and the green dashed line to the catalyst inlet temperature. 125

Figure 87 - Simulation results from WLTC 18: a) NMHC cumulated emissions, b) NMHC conversion efficiency, c) CO cumulated emissions, d) CO conversion efficiency. The red line represents the simulated value and the dashed blue is referred to the experimental result. 125

Figure 88 - Simulation results from WLTC 18: a) NO cumulated emissions, b) NO₂ cumulated emissions, c) NO_x cumulated emissions, d) NO_x conversion efficiency. The red line represents the simulated value, the dashed blue is referred to the experimental result and the dashed green to the inlet emissions. 126

Figure 89 - Comparison between simulated and experimental outlet temperatures referred to Hot WLTC 17. The red line is referred to the simulated trace, the blue dashed line to the experimental one and the green dashed line to the catalyst inlet temperature. 127

Figure 90 - Simulation results from WLTC 17: a) NMHC cumulated emissions, b) NMHC conversion efficiency, c) CO cumulated emissions, d) CO conversion efficiency. The red line represents the simulated value and the dashed blue one is referred to the experimental result. 127

Figure 91 - Simulation results from WLTC 17: a) NO cumulated emissions, b) NO₂ cumulated emissions, c) NO_x cumulated emissions, d) NO_x conversion efficiency. The red line represents the simulated value, the dashed blue is referred to the experimental result and the dashed green to the inlet emissions. 128

Figure 92 - Simulated and experimental outlet temperature referred to RDE 2. The red line is referred to the simulated trace, the blue dashed line to the experimental one and the green dashed line to the catalyst inlet temperature..... 129

Figure 93 - Simulation results from RDE 2: a) NMHC cumulated emissions, b) NMHC conversion efficiency, c) CO cumulated emissions, d) CO conversion efficiency. The red line represents the simulated value from updated calibration, the orange dashed one is referred to the original calibration and the dashed blue line is referred to the experimental result. ... 130

Figure 94 - Simulation results from RDE 2: a) NO cumulated emissions, b) NO₂ cumulated emissions, c) NO_x cumulated emissions, d) NO_x conversion efficiency. The red line represents the simulated value from updated calibration, the orange dashed one is referred to the original calibration, the blue dashed line is referred to the experimental result and the green dashed one to the inlet emissions. 130

Figure 95 - Simulated and experimental outlet temperature referred to RDE 3. The red line is referred to the simulated trace, the blue dashed line to the experimental one and the green dashed line to the catalyst inlet temperature..... 131

Figure 96 - Simulation results from RDE 3: a) NMHC cumulated emissions, b) NMHC conversion efficiency, c) CO cumulated emissions, d) CO conversion efficiency. The red line represents the simulated value and the blue dashed one is referred to the experimental result. 132

Figure 97 - Simulation results from RDE 3: a) NO cumulated emissions, b) NO₂ cumulated emissions, c) NO_x cumulated emissions, d) NO_x conversion efficiency. The red line represents the simulated value, the blue dashed one is referred to the experimental result and the green dashed line to the inlet emissions. 132

List of Tables

Table 1 - Representative CO ₂ and fuel economy requirements computed based on average footprints with a vehicle fleet comprising 67% passenger cars and 33% light duty trucks [1].	28
Table 2 - Tier 3 pollutant emission limits for gasoline and diesel light duty vehicles on FTP cycle [1].	29
Table 3 - Tier 3 pollutant emission limits for gasoline and diesel light duty vehicles on composite SFTP cycle [1].	30
Table 4 - US EPA & California Emission Standards for Heavy-Duty CI Engines, g/bhp*h [3].	31
Table 5 - Euro 5-6 pollutant limits for diesel light duty passenger cars expressed in mg/km on WLTC cycle [1].	32
Table 6 - Light Duty passenger vehicles categories definition on PMR basis [1].	33
Table 7 - CF for RDE type approval tests [1].	34
Table 8 - Euro VI limits on the WHSC and WHTC cycles for Compression Ignition HD engines [3].	35
Table 9 - Euro VI stages and OCE/ISC limits requirements [3].	36
Table 10 - LNT technology.	50
Table 11 - Temperature and inlet species concentration of LO experimental tests.	52
Table 12 - Temperature and inlet species concentration of OSC experimental tests (Lean/Rich Phases).	54
Table 13 - Temperature and inlet species concentration of TPD experimental tests.	57
Table 14 - Temperature and inlet species concentration of NSR experimental tests (Lean/Rich Phases).	59
Table 15 - Main characteristics of vehicle used for transient LNT full scale testing.	60
Table 16 - WLTC full scale experimental dataset.	61

Table 17 - RDE full scale experimental dataset.	61
Table 18 - Light-Off reactions over PGM sites.	67
Table 19 - OSC associated reactions.	74
Table 20 - NO _x storage reactions.	77
Table 21 - NO _x reduction reactions.	85

List of Equations

1	$SFTP = 0.35 * FTP + 0.28 * US06 + 0.37 * SC03$	29
2	$NTE_{pollutant} = CF_{pollutant} * EURO6_{limits}$	34
3	$BaO + 3NO_2 \rightarrow Ba(NO_3)_2 + NO$	43
4	$NO_2 + BaO \rightarrow BaO - NO_2$	43
5	$BaO - NO_2 \rightarrow BaO_2 + NO$	43
6	$2NO_2 + BaO_2 \rightarrow Ba(NO_3)_2$	43
7	$BaO + 2NO + 0.5O_2 \rightarrow Ba(NO_2)_2$	43
8	$Ba(NO_2)_2 + O_2 \rightarrow Ba(NO_3)_2$	44
9	$BaO + 2NO + 1.5O_2 \rightarrow Ba(NO_3)_2$	44
10	$BaO + 2NO_2 + 0.5O_2 \rightarrow Ba(NO_3)_2$	44
11	$2CeO_2 + CO \rightarrow Ce_2O_3 + CO_2$	54
12	$2CeO_2 + 0.111111C_3H_6 \rightarrow Ce_2O_3 + 0.333333CO_2 + 0.333333H_2O$	54
13	$H_2O + CO \rightarrow CO_2 + H_2$	55
14	$C_3H_6 + 3H_2O \rightarrow 3CO + 6H_2$	55
15	$f(t) = A * (1 - e^{-\frac{t}{\tau}})$	59
16	$f(t) = A * e^{-\frac{t}{\tau}}$	59
17	$K = A * e^{-\frac{E_a}{RT}}$	65
18	$R = K * C * G_i * \theta_i$	65
19	$G1 = f_1(\{CO\}) * f_2(\{HC\}) * f_3(\{CO\}, \{HC\})$	69
20	$G23 = 1 + e^{-30} * e^{\frac{14000}{t}}$	71

21	$G27 = 1 + e^{\frac{2300}{t}} * \{O_2\}$	75
22	$G24 = 1 + e^{\frac{5000}{t}} * \{C_3H_6\} + e^{\frac{6800}{t}} * \{CO\} + e^{\frac{6000}{t}} * \{H_2\}$	82
23	$G25 = 1 + e^{\frac{4000}{t}} * \{C_3H_6\} + e^{\frac{6800}{t}} * \{CO\} + e^{\frac{7000}{t}} * \{H_2\}$	82
24	$G17 = 1 + e^{-23.382} * e^{\frac{13970}{t}} * \{O_2\}$	91

List of acronyms

Ammonia Slip Catalyst	ASC
Belt Alternator Starter	BAS
California Air Resources Board	CARB
CO2 Module for Passenger and commercial vehicles Simulation	CO2MPAS
Compression Ignition	CI
Conformity Factor	CF
Corporate Average Fuel Economy	CAFE
Diesel Exhaust Fluid	DEF
Diesel Oxidation Catalyst	DOC
Diesel Particulate Filter	DPF
Environmental Protection Agency	EPA
Exhaust Gas Recirculation	EGR
Federal Test Procedures	FTP
Gasoline Direct Injection	GDI
Green House Gases	GHG
Heavy Duty	HD
Heavy Duty Federal Test Procedure	HD-FTP
Highway Fuel Economy Test	HWFET
In-Service Conformity	ISC
Lean NO _x Trap	LNT
Light-Off SCR	LO-SCR
New European Driving Cycle	NEDC
Non Methane Organic Gas	NMHC
Not To Exceed	NTE
NO _x Storage and Reduction	NSR
Off Cycle Emission	OCE
Oxygen Storage Capacity	OSC

Particulate Matter	PM
Particulate Number	PN
Passive NO _x Adsorber	PNA
Portable Emissions Monitoring Systems	PEMS
Positive Ignition	PI
Power to Mass Ratio	PMR
Precious Gold Metals	PGM
Real Driving Emissions	RDE
SCR on Filter	SCR-F
Selective Catalytic Reduction	SCR
Space Velocity	SV
Supplemental Emission Test	SET
Supplemental Federal Test Procedures	SFTP
Synthetic Gas Bench	SGB
Temperature Programmed Desorption	TPD
Temperature Programmed Reduction	TPR
Three Way Catalyst	TWC
Type Approval	TA
Ultra Low NO _x	ULN
Ultra Low Sulfur Diesel	ULSD
Worldwide harmonized Light vehicles Test Cycle	WLTC
Worldwide Harmonized Steady state Cycle	WHSC
Worldwide Harmonized Transient Cycle	WHTC

1 INTRODUCTION

In the last decades the evolution of legislative framework for pollutant emission of motorized vehicles led to even more tightening limits. The introduction of Euro 6d in Europe and the phasing in of Tier 3 in North America pushed the development of new advanced aftertreatment technologies, able to reduce tail pipe emission below the requested values. This chapter presents the main regulations in terms of CO₂ and pollutant emissions for the European and North American markets, introducing the available aftertreatment technologies for pollutants abatement. Particular emphasis will be posed on the analysis of catalysts able to reduce the NO_x emissions under highly oxidizing conditions, like in the exhaust gases of diesel engines, focusing on the role of Lean NO_x Trap (LNT) in the current and future aftertreatment systems.

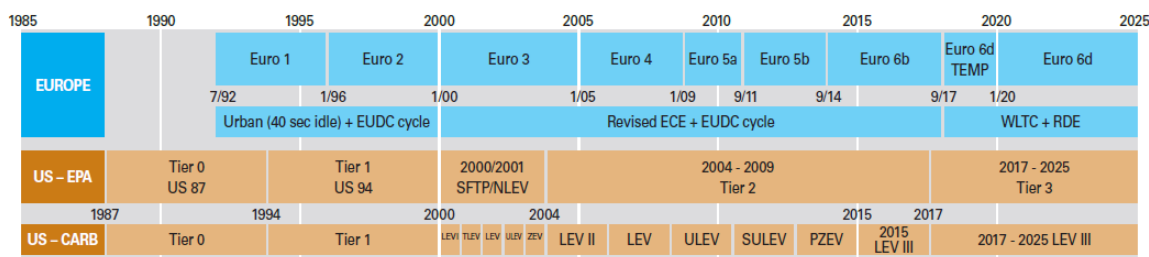


Figure 1 - Overview of pollutant regulations in Europe and North America for light duty passenger cars [1].

1.1 Legislative framework for fuel economy and pollutant emission

1.1.1 North America

1.1.1.1 Light-duty vehicles

US has two sets of parallel standards for CO₂ regulations:

- The Corporate Average Fuel Economy (CAFE);
- The Greenhouse Gas (GHG) emission standards by the Environmental Protection Agency (EPA).

The first standard defines the average fuel economy to respect by the sales-weighted fuel economy for the entire fleet sold in USA. The targets were assigned according to vehicle’s footprint (product of average track width and wheelbase). The second standard defines the CO₂ emission limits to be respected by the sales weighted GHG emission level for the entire fleet sold in USA. These two standards have been merged in the harmonized CAFE and GHG emission rules.

California has also its own regulations in term of greenhouse gases from motor vehicles: the California Air Resources Board (CARB), become effective from January 2006.

In 2012 EPA, CAFE and CARB decided to finalize common target for 2017-2025. So, starting from 2017 and phasing in 2025, in accord with their vehicle footprints, these vehicles must respect an average fuel economy in accord with values showed in Table 1.

Projected 2017-25 fleet-wide CO ₂ and fuel economy compliance levels										
Vehicle Category & Standard		Model Year								
		2017	2018	2019	2020	2021	2022	2023	2024	2025
Passenger Cars	CO ₂ g/mi	212	202	191	182	172	164	157	150	143
	Fuel eco. (mpg) ¹	41.9	44.0	46.5	48.8	51.7	54.2	56.6	59.3	62.2
Light Duty Trucks	CO ₂ g/mi	295	285	277	269	249	237	225	214	203
	CO ₂ equiv. mpg	30.1	31.2	32.1	33.0	35.7	37.5	39.5	41.5	43.8
Combined Cars & Trucks	CO ₂ g/mi	243	232	222	213	199	190	180	171	163
	CO ₂ equiv. mpg	36.6	38.3	40.0	41.7	44.7	46.8	49.4	52.0	54.5

Table 1 - Representative CO₂ and fuel economy requirements computed based on average footprints with a vehicle fleet comprising 67% passenger cars and 33% light duty trucks [1].

Vehicles are tested for fuel economy over the 5-cycle test, or else over the FTP-75 and HWFET, cold FTP, US06 and SC03 cycles.

For pollutant emission US EPA introduced Tier 3 standards starting from 2017 and phased-in 2025. Manufacturers must certify vehicles to one of seven available “certification bins”, meeting a fleet-average emission standard for the entire vehicle fleet in a given model year. The name of the bin derives from the correspondent NMOG + NO_x (Non-Methane Organic Gases) emission level, and the fleet average NMOG+NO_x emission must reach 30 mg/mi (18.64 mg/km) by 2025. The vehicle is tested over the FTP cycle for pollutant emissions and need to respect the emission limits of its correspondent certifications bin.

Tier 3 Certification Bin Standards (FTP, 150,000 mi)				
Bin	NMOG+NO _x (mg/mi)	PM ^{2.5} (mg/mi)	CO (g/mi)	HCHO (mg/mi)
Bin 160	160	3	4.2	4
Bin 125	125	3	2.1	4
Bin 70	70	3	1.7	4
Bin 50	50	3	1.7	4
Bin 30	30	3	1.0	4
Bin 20	20	3	1.0	4
Bin 0	0	0	0	0

Table 2 - Tier 3 pollutant emission limits for gasoline and diesel light duty vehicles on FTP cycle [1].

All light duty vehicles are also tested over two additional driving cycle that consider different driving behaviors: the US06 and the SC03. The first one considers the effect of higher speeds and loads requirements, while the second takes into account higher temperatures conditions (35°C) and the Air Conditioning unit (A/C) load.

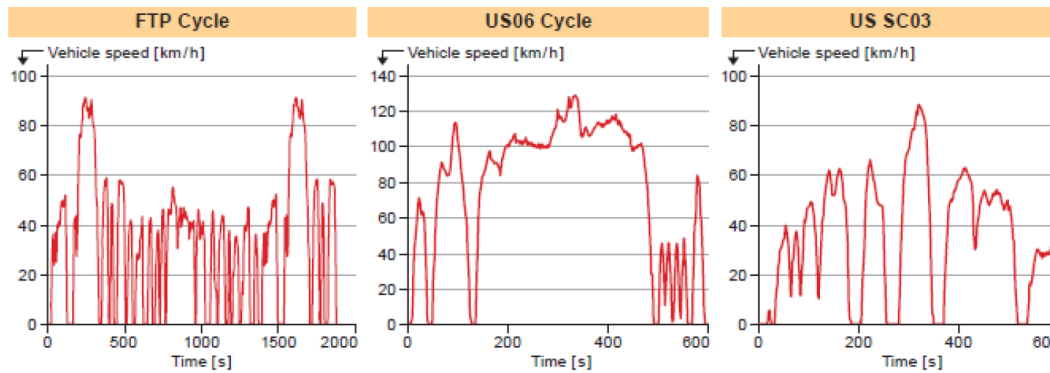


Figure 2 - FTP75, US06 and SC03 driving cycles for type approval tests [2].

The emission results of all the three cycles are differently weighted forming an equivalent SFTP driving cycle:

$$1 \quad SFTP = 0.35 * FTP + 0.28 * US06 + 0.37 * SC03$$

To be certified, the pollutant emissions must comply also with SFTP limits.

Tier 3 Fleet Average NMOG+NO _x SFTP Standards									
Emission	2017 ²⁾	2018	2019	2020	2021	2022	2023	2024	2025
NMOG+NO _x (mg/mi)	103 ³⁾	97	90	83	77	70	63	57	50
CO (g/mi)	4.2								

Table 3 - Tier 3 pollutant emission limits for gasoline and diesel light duty vehicles on composite SFTP cycle [1].

1.1.1.2 Heavy-duty vehicles and buses

US EPA signed emission standards for model year 2007 and later heavy-duty highway engines on December 2000, subsequently adopted by California ARB in October 2001. No CO₂ regulation is expected by the normative, but two stringent limits for PM and NO_x emission were defined [22]:

- 0.01 g/bhp*h for PM;
- 0.20 g/bhp*h for NO_x.

While the PM limits took full effect in 2007, the NO_x limit was phased in between 2007 and 2010.

The USA regulation for Heavy Duty (HD) and Buses expects the engine to pass several tests. HD Diesel engine are tested on the Heavy-Duty transient FTP (HD-FTP) engine dynamometer cycle. Furthermore, the engine must pass other Supplemental Emission Tests (SET), composed by two cycles: a discrete mode cycle and a ramped mode cycle. Finally, to avoid cycle beating, in the Not To Exceed (NTE) test some operating points are randomly selected. The limits for SET are equal to the HD transient FTP dynamometer test, while the NTE limits are 1.5 times the HD-FTP standards.

Diesel fuel is also regulated beginning from June 2006. All refiners must produce Ultra Low Sulfur Diesel (ULSD) with maximum sulfur content of 15 ppm, a good improvement if compared to the previous value of 500 ppm. These limits were imposed to preserve catalysts performances from sulfur poisoning, enabling to maintain exhaust aftertreatment efficiencies for longer mileage.

Year	CO	HC ^a	HC ^a +NO _x	NO _x	PM	
					General	Urban Bus
2004 ^j	15.5	-	2.4 ⁱ	-	0.10	0.05 ^h
2007	15.5	0.14 ^k	-	0.20 ^k	0.01	
2015	15.5	0.14	-	0.02 ^l	0.01	

h. In-use PM standard 0.07 g/bhp·hr
i. Alternative standard: NMHC+NO_x = 2.5 g/bhp·hr and NMHC = 0.5 g/bhp·hr
j. Under the 1998 Consent Decrees, several manufacturers supplied 2004 compliant engines from October 2002.
k. NO_x and NMHC standards were phased-in on a percent-of-sales basis: 50% in 2007-2009 and 100% in 2010. Most manufacturers certified their 2007-2009 engines to a NO_x limit of about 1.2 g/bhp·hr, based on a fleet average calculation.
l. Optional. Manufacturers may choose to certify engines to the California Optional Low NO_x Standards of 0.10, 0.05 or 0.02 g/bhp·hr

Table 4 - US EPA & California Emission Standards for Heavy-Duty CI Engines, g/bhp*h [3].

California, leader in the pollutants control and air quality preservation in North America, will drop NO_x emission to 20 mg/bhp*h by about 2024 [4]. Thus, starting from 2015, manufacturers may choose to certify their engine to three optional NO_x emission standards: 0,10 – 0,05 – 0,02 g/bhp*h [22]. Furthermore, California regulation is trying to develop a low load certification cycle, introducing even more challenging operating conditions for the exhaust aftertreatment system.

1.1.2 Europe

1.1.2.1 Light-duty vehicles

European Commission, European Parliament and European Council agreed for European Union regulation CO₂ emission targets on vehicle fleet of 95 g/km (passenger cars) and 147 g/km (light-commercial vehicles) over the New European Driving Cycle (NEDC).

From September 2017 pollutants and CO₂ emissions are measured over the Worldwide Harmonized Light-Duty Test Cycle (WLTC), which replaced the NEDC procedure in case of the laboratory test. Therefore, the CO₂ emissions are converted to the NEDC equivalent value based on CO2MPAS software, while in case of pollutants emissions no changes are expected.

Starting from EURO 6d-Temp regulation, the measurements from the lab tests are completed with the Real Driving Emissions (RDE) procedure, which requests to test vehicles on streets.

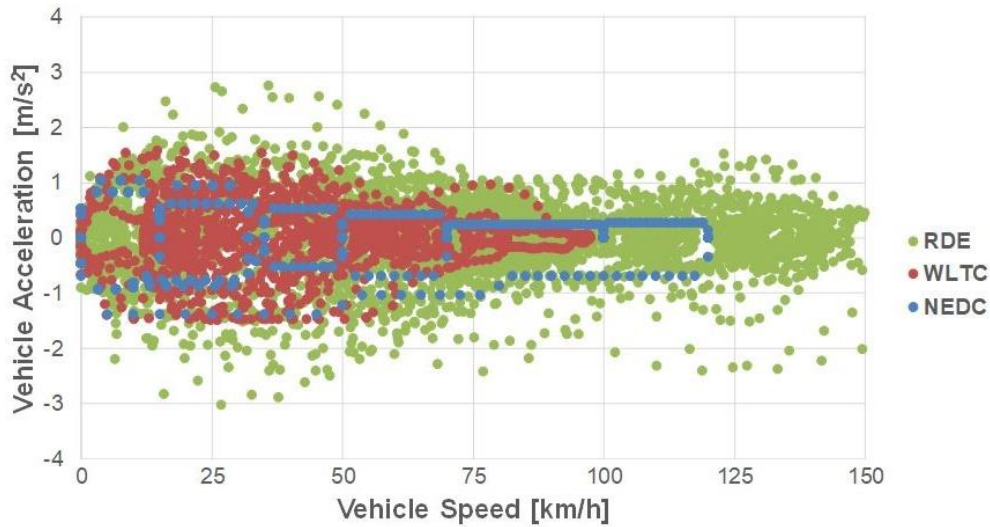


Figure 3 - Comparison between NEDC, WLTC and RDE cycles vehicle acceleration VS vehicle speed points [5].

The legal NO_x limit from Diesel fueled passenger cars is fixed at 80 mg/km on the WLTC lab test. While in case of RDE test a conformity factor is applied.

Emissions	Unit	PC M ¹³ , LCV N1 CL 1			LCV N1 CL 2			LCV N1 CL 3, N2		
		Euro 5a	Euro 5b/b+	Euro 6b, 6c, 6d-Temp, 6d	Euro 5a	Euro 5b/b+	Euro 6b, 6c, 6d-Temp, 6d	Euro 5a	Euro 5b/b+	Euro 6b, 6c, 6d-Temp, 6d
EURO 5-6 Compression ignition emissions limits ((EC) 715/2007 as amended (EC) 692/2008)										
NO _x	mg/km	180	180	80	235	235	105	280	280	125
HC+NO _x		230	230	170	295	295	195	350	350	215
CO		500	500	500	630	630	630	740	740	740
PM ¹⁰		5.0	4.5	4.5	5.0	5.0	4.5	5.0	5.0	4.5
PN ¹⁰	Nb/km	-	6x10 ¹¹	6x10 ¹¹	-	6x10 ¹¹	6x10 ¹¹	-	6x10 ¹¹	6x10 ¹¹

Table 5 - Euro 5-6 pollutant limits for diesel light duty passenger cars expressed in mg/km on WLTC cycle [1].

1.1.2.1.1 WLTC – Worldwide harmonized Light-duty Test Cycle

WLTC is the regulatory cycle adopted by European regulation since September 2017. The WLTC cycle is closer to real driving conditions than NEDC, because it is characterized by higher dynamics, it requests more realistic road loads and the enabling of auxiliary components [6].

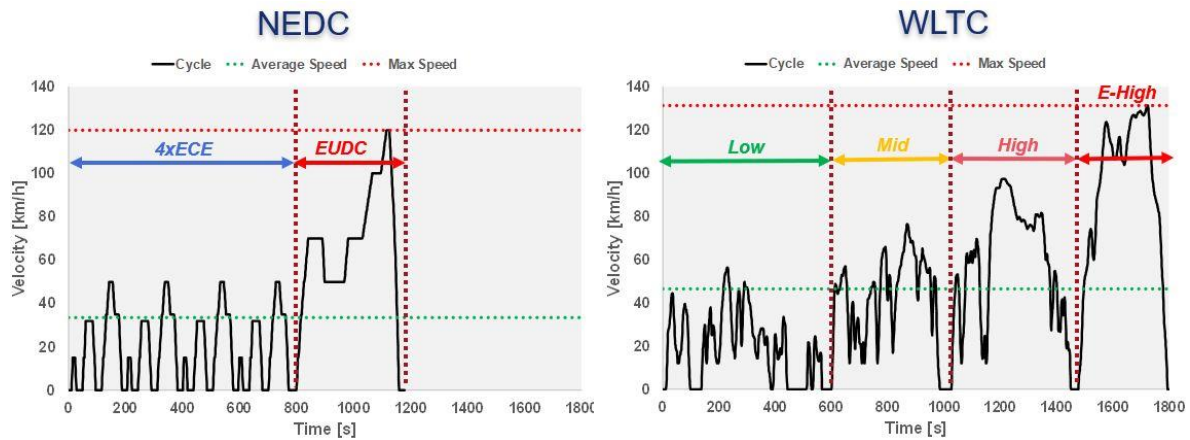


Figure 4 - Comparison between NEDC (left) and WLTC (right) vehicle speed profiles [5].

Depending on the Power to Mass Ratio (PMR) of the tested vehicle, different combinations of low, medium, high and extra high WLTC phases are used for type approval procedures.

Category		PMR (W/kg)	Speed Phases
Class 3	3a ($v_{max} < 120$ km/h)	PMR > 34	Low ₃ +Medium ₃₋₁ +High ₃₋₁ +Extra High ₃₋₁
	3b ($v_{max} \geq 120$ km/h)		Low ₃ +Medium ₃₋₂ +High ₃₋₂ +Extra High ₃₋₁
Class 2		22 < PMR ≤ 34	Low ₂ +Medium ₂ +High ₂ +Extra High ₂₋₂
Class 1		PMR ≤ 22	Low ₁ +Medium ₁ +Low ₁

Table 6 - Light Duty passenger vehicles categories definition on PMR basis [1].

1.1.2.1.2 RDE – Real Driving Emission cycle

The RDE test is carried out on public roads with real traffic and the pollutant emissions are measured with the Portable Emissions Measurements Systems (PEMS). The trip consists of three different portions: urban, extra urban and highway conditions. RDE test includes the cold start phase and strictly regulates its conditions, placing bounds on average and top speeds, the idle time and the total stop time during this phase of the test. An example of RDE test is reported in Figure 5. Air conditioning and other auxiliary devices must normally operate during the trip. Furthermore, at the end of the driving procedure, a trip verification is carried out. In fact, the cycle must respect all the ambient boundary conditions and trip

requirements, such as ambient temperature range, altitude range, distance, speed and stop time. The driving dynamic is also checked a posteriori.

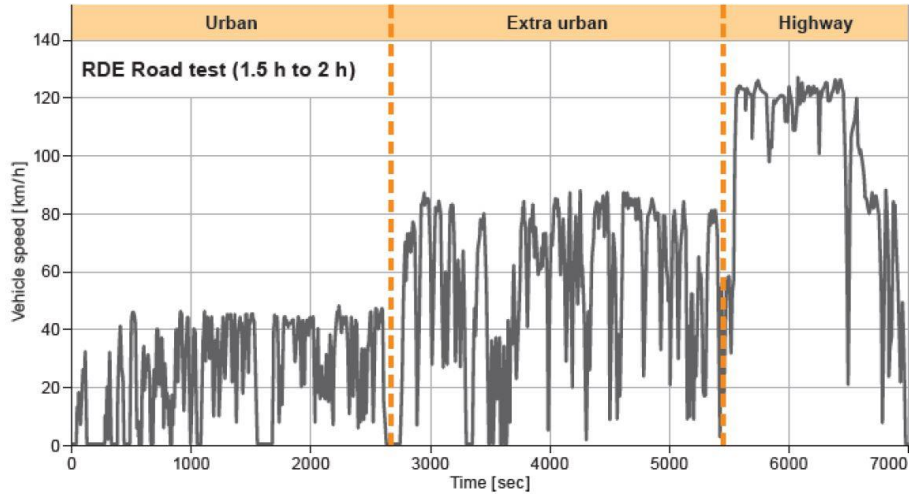


Figure 5 - Example of an RDE test cycle recorded during road testing [2].

The RDE test should be compliant with the NTE limits. The calculation of NTE is reported in equation 2 where CF is the conformity factor and Euro6_{limit} is the Euro 6 limit of a specific pollutant. For example, the NTE limit for NO_x corresponds to the Euro 6 limit multiplied by a CF factor equal to 2.1 for euro 6d-Temp regulation and 1.43 for Euro 6d.

$$2 \quad NTE_{pollutant} = CF_{pollutant} * EURO6_{limit}$$

Conformity Factors for Euro 6d RDE			
CF _{pollutant}	NO _x	PN	CO ₂
Temporary (Euro 6d-Temp)	2.1	1 + margin PN with margin PN = 0.5	–
Final (Euro 6d)	1 + margin NO _x with margin NO _x = 0.43	1 + margin PN with margin PN = 0.5	–

Table 7 - CF for RDE type approval tests [1].

1.1.2.2 Heavy duty engines

The latest EURO VI regulation for diesel HD engine pollutant emission expects several cycle tests to be passed. The engine only is tested on a dynamometer (without the vehicle) on two different type approval cycle:

- Worldwide Harmonized Steady state Cycle (WHSC): a ramped steady-state cycle with a sequence of steady state engine test modes with defined torque and speed;
- Worldwide Harmonized Transient Cycle (WHTC): a transient dynamometer schedule with several monitoring segments and both cold and hot start requirements.

Stage	Date	Test	CO	HC	NOx	PM	PN	Smoke
			g/kWh					1/kWh
Euro VI	2013.01	WHSC	1.5	0.13	0.40	0.01	8.0×10 ¹¹	
Stage	Date	Test	CO	NMHC	CH ₄ ^a	NOx	PM ^b	PN
			g/kWh					1/kWh
Euro VI	2013.01	WHTC	4.0	0.16 ^d	0.5	0.46	0.01	6.0×10 ^{11e}

^d THC for diesel (CI) engines
^e PN limit for PI engines applies for Euro VI-B and later [EC 2014]

Table 8 - Euro VI limits on the WHSC and WHTC cycles for Compression Ignition HD engines [3].

To avoid cycle beating, the engine must pass two other Off Cycle Emission (OCE) testing:

- NTE Testing, where some operating points are randomly selected to test the engine;
- Type-Approval (TA) PEMS testing;

In the first case the engine is tested in laboratory on dynamometer bench. A control area is defined on the engine map and divided into grids. Three cells are randomly selected and emission measurement will occur on 5 load points per cell. In the second case the entire vehicle is tested with a payload between 50-60%. The procedure is carried out over a defined mix of urban, rural and motorway conditions on public streets. Pollutant emission levels must comply with the WHTC limits multiplied by a conformity factor.

Stage	Implementation Date		OCE/ISC Requirements				
	Type approval (new types/all vehicles)	Last date of registration	PEMS power threshold	Cold start included in PEMS	OCE NTE g/kWh	PEMS CO, HC, NMHC, CH ₄ CF	PEMS PN CF
A	2013.01/2014.01	2015.08	20%	No	NOx 0.60 THC 0.22 CO 2.0 PM 0.016	1.50	-
B (CI)	2013.01/2014.01	2016.12					
B (PI)	2014.09/2015.09	2016.12					
C	2016.01/2017.01	2017.08					
D	2018.09/2019.09	2021.12					
E	2020.09/2021.09	-	10%	Yes			1.63 ^a

^a For PI engines and type 1A and 1B dual fuel engines in dual fuel mode, PN CF applies 2023.01/2024.01

Table 9 - Euro VI stages and OCE/ISC limits requirements [3].

The HD engines must respect an In-Service Conformity (ISC) during their useful life, thus maintaining the pollutant emission level under a certain range for a defined distance depending on vehicle category. This requirement is checked by a ISC testing similar to PEMS testing described above.

An additional regulation imposes not to exceed 10 ppm concentration value for the ammonia slip in tail pipe emissions on both the WHSC and WHTC cycles for Compression Ignition (CI) engine.

Differently from Light-Duty vehicles legislation, HD Engine emissions are expressed in g/kWh, to free the emission level from the variable payload of these vehicles.

1.2 Technological path to reduce NO_x emissions

The introduction of new emissions standards and procedure like the RDE cycle in Europe, is making complex the compliance with new NO_x limits, using well known technologies like the Diesel Oxidation Catalyst (DOC), the common rail and the Exhaust Gas Recirculation (EGR). For example, the RDE procedure stresses both the problem of “Cold Start” emissions and of the limitation of Exhaust Gas Recirculation (EGR) in the high engine loads.

The compliance with tight emission limits in a wide range of operating conditions requests the integration of different aftertreatment technologies, which in case of Diesel engines are:

- **Diesel Oxidation Catalyst (DOC):** a catalyst coated with Platinum Group Metals (PGM), which has the role to oxidize CO and HC emissions, while promoting the NO conversion to NO₂, helping the downstream components efficiencies like the Diesel Particulate Filter (DPF) and the Selective Catalytic Reduction (SCR) systems.

Additional feature can be implemented adding trapping materials, such as Zeolite, to store HCs in the cold start phase, releasing them when the catalyst light-off is reached;

- **Diesel Particulate Filter (DPF):** It is a mechanical filter used to trap the Particulate Matter (PM), which should be periodically regenerated to recover the trapping capacity and to avoid the pressure difference between inlet and outlet to be too high;
- **Selective Catalytic Reduction (SCR):** this technology promotes the NO_x reduction thanks to the presence of ammonia in the exhaust stream as reductant agent. The ammonia can be obtained from the decomposition of Urea injected upstream of the SCR or it can be a product of catalysis reaction from the Lean NO_x Trap (LNT);
- **Lean NO_x Trap (LNT):** The LNT is a PGM based catalyst, which promotes during lean events the adsorption of NO_x thanks to the presence of barium sites and the oxidation of pollutants like CO and HCs. The reduction of NO_x into N₂ is promoted during rich events, which should be enabled when the chemical trap is saturated;
- **SCR on Filter (SCR-F):** The SCR-F integrates the capabilities of the SCR on a DPF. This double purpose catalyst allows to reduce the packaging volumes and costs, achieving lower thermal capacity and faster warm-ups in automotive applications [7].

In case of passenger cars the compliance with Euro 6 emission requests the combination of different catalysts such as DOC/LNT, DPF/SCR-F, SCR and ASC.

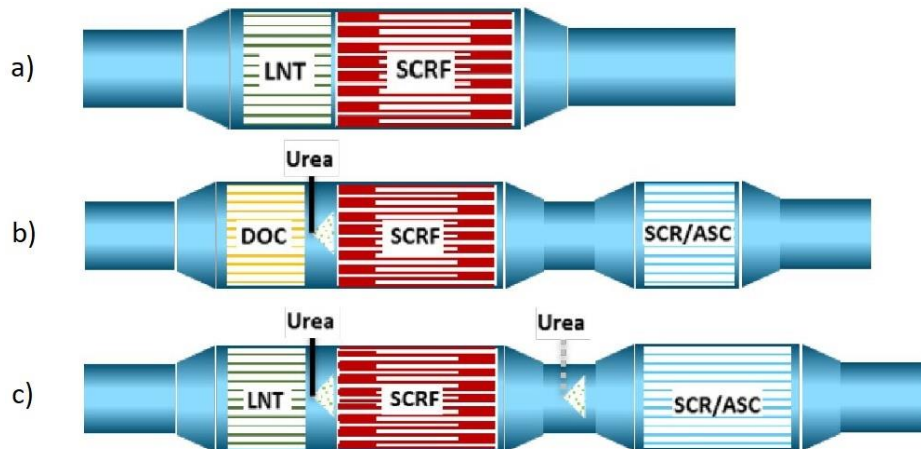


Figure 6 - Possible applicable configurations to comply with light duty passenger cars Euro 6b (figures a, b) and Euro 6d (figure c) pollutant limits [8].

In case of HD vehicles for US market, the path to achieve the Ultra-Low NO_x (ULN) levels requests the definition of new technologies. The ULN requests NO_x emissions below 0.02 g/bhp*h (0.026 g/kWh) [9].

To reach this level of NO_x emissions not only aftertreatment components must be upgraded, but the engine and aftertreatment system control strategies must be improved too. These advanced systems for ULN emission require evolved warm-up strategies in the cold start phase and low load driving conditions. In fact, pollutant emitted during the early cold phases represent the main part of the emissions during the driving cycle, because the NO_x conversion system has not reached the light-off temperature.

Some technological path to achieve ULN emission are listed below and can be divided into two main parts:

- Advanced warm-up strategies;
- Upgrade of aftertreatment components.

Focusing the attention on aftertreatment, the fulfillment of ULN levels requests the introduction of new catalysts characterized by high performance during the “Cold Start” events such as:

- **Passive NO_x Adsorber (PNA):** similar to LNT, PNA is a NO_x adsorbed catalyst coated with PGM. PNA traps NO_x during the cold start phases and thermally releases them when the downstream catalysts have reached the light-off temperature. Due to the PGM loading, this component acts also like a DOC, oxidizing HCs and CO and promoting the NO to NO₂ conversion. It doesn't need regeneration events or lean/rich cycling because, as the temperature increase, all the NO_x stored is released. Thus, CO₂ emissions and fuel consumption are not affected. Different formulations appear in the literature [10,11,12], such as Pt-Pd/Al₂O₃, Pt-Pd/CeO_x and Pt-Pd/La-Al₂O₃. However, the most effective ones usually contain also Zeolites that can store some quantity of unburned HCs in the cold start phases and show more resistance to sulfur poisoning. Recent studies (2019) investigated a WO₃-ZrO₂ formulation showing good performance.
- **Dual-layer SCR-LNT catalyst:** is a NO_x trap based on a multiple catalytically active layers coated on the channel walls of the monolithic substrate. A possible configuration expects a first SCR layer with an underneath LNT layer, leading to the double possibility to reduce NO_x to N₂ by SCR reactions and store and reduce NO_x by NSR reactions. The LNT formulation can be chosen to give the maximum selectivity of NO_x reduction to the formation of NH₃, useful for the SCR layer. This dual layer configuration can have some diffusion limitation for the underneath layer that can be solved by coating the SCR only on a downstream washcoat portion [13].

Figure 7, Figure 8 and Figure 9 show new generation aftertreatment architectures capable to fulfill the ULN requirements.

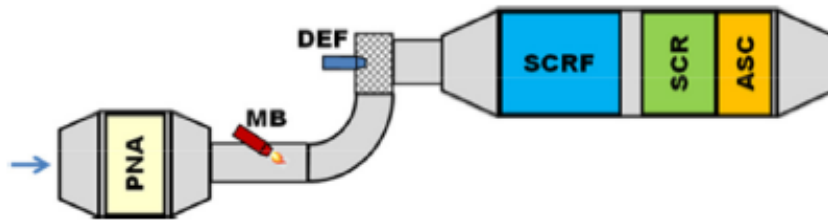


Figure 7 - Possible aftertreatment configuration to achieve ULN emissions [14].

In case of Figure 7, the PNA acts as a NO_x buffer, since it adsorbs the NO_x during the cold phase and it releases them once the SCR system has reached the light-off temperature. The SCR system is divided into three part, one coated on the DPF, one stand-alone SCR and an Ammonia Slip Catalyst (ASC). The SCR-F takes care of NO_x emitted on low load conditions while the downstream SCR take care of NO_x emitted during high load and high space velocity conditions, when the SCR-F is not enough to convert all NO_x produced. The ASC catalyst has the role to convert the ammonia slipped from the upstream SCR system avoiding the NH₃ diffusion into the atmosphere [14]. This architecture requests the introduction of two additional components: one mini-burner allows the injection of additional HCs to activate the DPF regeneration, while the Diesel Exhaust Fluid (DEF) takes care of Urea injection for the downstream SCR.

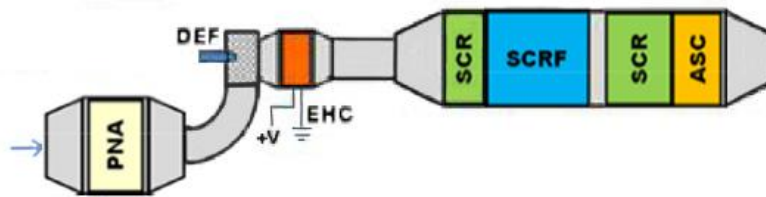


Figure 8 - Possible aftertreatment configuration to achieve ULN emissions [15].

The Figure 8 shows another possible configuration of the aftertreatment system. In this case the extra heat is given by an electric heating system and a small SCR is positioned just downstream of it with the aim to reduce the warm-up time of the SCR.

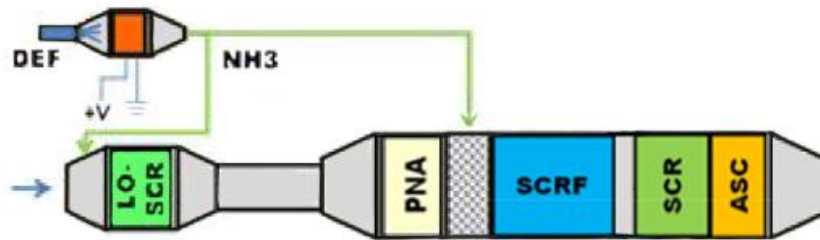


Figure 9 - Possible aftertreatment configuration to achieve ULN emissions [15].

A more complex system is shown in Figure 9, where a Light-Off SCR (LO-SCR) is positioned in close coupled position to improve the catalyst heating time in the cold start phases. This configuration requires the introduction of a Dual DEF system to guarantee the optimal conversion efficiency of all SCR components [15].

1.3 LNT technology

1.3.1 Overview

The LNT or NO_x Storage and Reduction (NSR) catalyst is a PGM and alkaline metals coated catalyst, which is used to adsorb and reduce NO_x.

The concept of LNT was introduced in the middle 90s by Toyota for Gasoline Direct Injection (GDI) lean-burn engine applications. However, the technology is suitable for all engines operating in lean conditions, such as the Diesel engines [16]. This was possible because of the better quality of fuels available in the Japanese market. In fact, the LNT catalyst suffer of sulfur poisoning that reduces the catalyst efficiency, and in the 90's, in Europe, the fuels quality was not high enough to commercialize such technology.

Usually, an high dispersion area washcoat is deposited on a monolithic structure of cordierite. The washcoat is formed by porous and high surface area materials. The gamma-Allumina (γ -Al₂O₃) is the most used, but also other kind of materials can be considered, like ZrO₂ and MgO. Generally, Ceria is added to give some Oxygen Storage Capacity (OSC) and stabilize the washcoat chemical composition at higher temperatures. Furthermore, other materials can be added in minor quantities to increase washcoat stability.

The noble metals loading is normally based on Platinum (Pt) coating, that is the best promoter for NO oxidation to NO₂. However, also Palladium (Pd) and Rhodium (Rh) can be used. The latter is particularly active in the NO_x reduction phase. Moreover, the PGM loading enables the oxidation of CO and unburned HCs.

Most of the commercially available LNT catalysts use NO_x storage materials based on barium, but also other alkaline and earth-alkaline metals can be exploited, such as Na, K, Sr, Ca, Li and Mg. The NO_x storage capacity of these materials is directly correlated to their basicity [16].

The LNT operates under two different conditions:

1. the lean phase promotes the NO_x sorption on the storage materials in nitrite/nitrate form;
2. the rich phase destabilizes the adsorbed species allowing the release of NO_x and their reduction to N₂.

Figure 10 schematically illustrates the storage and reduction behavior over the LNT washcoat.

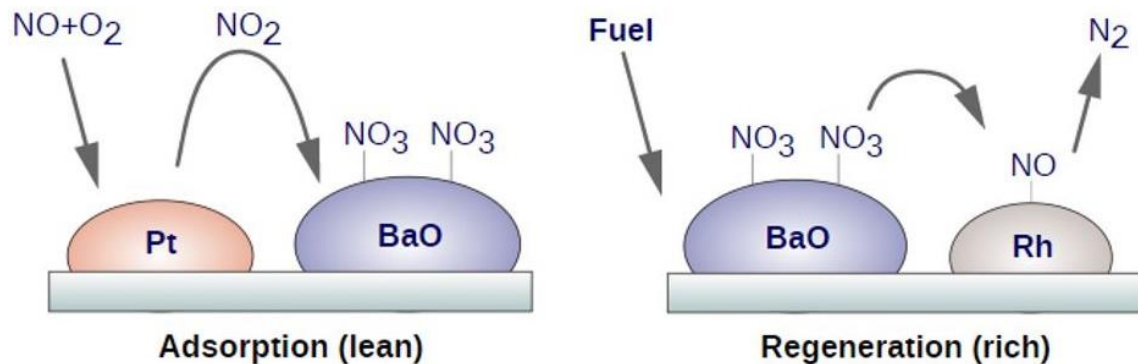


Figure 10 - NO_x adsorption and desorption/reduction behaviors on a Pt-Ba/Al₂O₃ based LNT catalyst [17].

The rich phases are necessary for LNT catalyst because, without it, the storage capacity is rapidly saturated, leading to high NO_x tailpipe emissions.

The NO_x Storage and Reduction mechanism can be summarized into five steps [16,18]:

1. NO to NO₂ oxidation;
2. NO_x adsorption as nitrites or nitrates on storage sites during the lean phase;
3. Reducing agent introduction through late post injection (mainly CO, HCs and H₂ derived from the combustion process) or an additional fuel injector upstream of the catalyst;

4. NO_x release into the gas stream during the rich phase;
5. NO_x reduction to N_2 through reactions with reducing agents during the rich phase.

1.3.1.1 NO_x storage

Under appropriate conditions the LNT catalyst is capable to completely remove NO_x species from the exhaust flow of a lean-burn diesel engine. However, sensible variation of these conditions can affect NO_x removal performances.

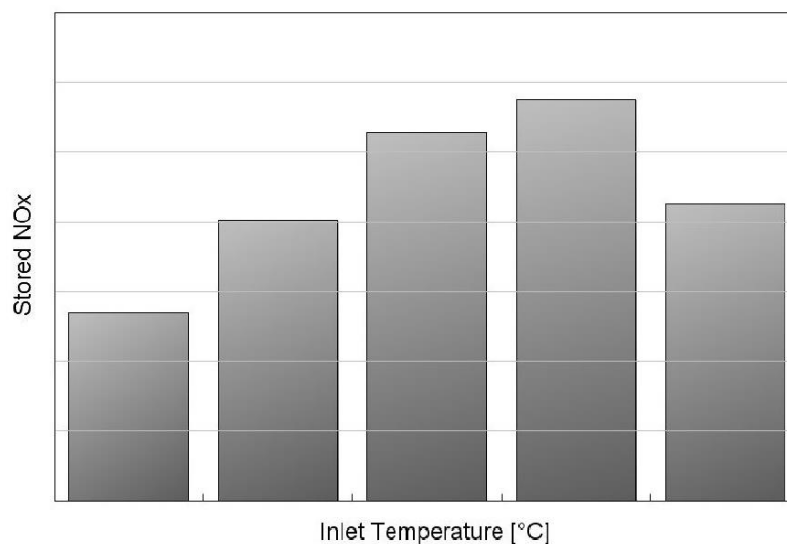
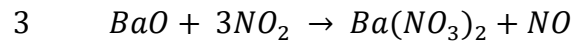


Figure 11 - Bell shaped storage capacity dependency from temperature over a Pt/Ba based LNT catalyst [19].

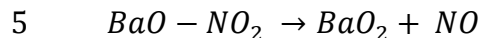
As showed in Figure 11, the NO_x storage capacity is primary function of temperature and it follows a bell shaped behavior. This trend is the result of two competing effects: the first is the adsorption rate that increases with temperature, the second is the nitrate and nitrite thermodynamic stability, that decreases with temperature. However, it also depends on catalyst formulation and environment composition. In fact, for a fixed temperature, some studies [18,20,21] found that moving from 1 to 3% the oxygen concentration in the feeding gas improves the trapping capacity, thanks to the increased thermodynamic stability of adsorbed species and the higher availability of O_2 , shifting thermodynamic equilibrium to better surface nitrates formation. Despite this, for further increase in oxygen concentrations, albeit the sorption rate still increases, the stored NO_x does not. Around 350/400°C, depending on catalyst formulation and atmosphere composition, the instability of adsorbed species dominates on adsorption rate, leading to NO_x desorption.

The storage of NO_x species occurs on catalyst surface, thanks to alkaline or alkaline-earth metals present in the washcoat formulation. In this study, a Pt-Ba/Al₂O₃ catalyst is considered. Despite storage on barium sites is the main phenomena, several studies [18,22, 23,24] found that sorption process can occur not only on BaO, but also Hydroxide (Ba(OH)₂) and Carbonate (BaCO₃) can compete as trapping sites. Therefore, the presence of H₂O and CO₂ in the feeding gas can affect the LNT storage capacity. In fact, barium oxides can adsorb water and carbon dioxide forming the more stable carbonates and hydroxides. Since the stability of these species is higher, nitrates and nitrites formation will result slowed down and accompanied by CO₂ and H₂O evolution. Furthermore, in certain operating conditions and in Pt-coated formulations also Al₂O₃ sites have found to participate in minor quantities to weakly bonded nitrates and nitrites formations [18]. Thus, also the substrate can compete with sorbate components in NO_x adsorption.

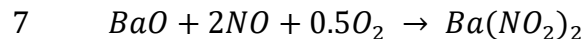
Similar Pt-Ba/Al₂O₃ catalysts [7,16, 22,23, 25] highlighted that the NO_x sorption process can follow different ways. Both NO and NO₂ species can be adsorbed in presence of O₂ in the feeding gas. However, in absence of it, almost no NO is stored, while appreciable quantities of NO₂ are still adsorbed by the storage materials. In this case the sorption process of NO₂ follow the so called Nitrates route, where 3 moles of NO₂ react with the barium site to form one mole of nitrate (Ba(NO₃)₂) and release one mole of NO in the gas flow:



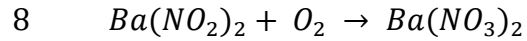
Reaction 3 represents the overall stoichiometry of a three steps mechanism [16,18,25]:



In presence of oxygen and on Pt-coated catalysts, the storage process can follow another way. In fact, Pt sites cause the formation of big source of monoatomic oxygen through spillover reactions that involve O₂ and NO₂ as precursors [18,21]. Thus, at lower temperatures, at the beginning of the adsorption process, mainly nitrite (Ba(NO₂)₂) species are stored through the reaction 7:

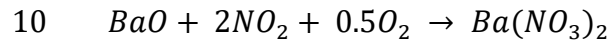
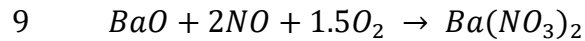


Continuing the adsorption, almost all the nitrites are converted to nitrates by oxidation [24,26]:



At the end of the process only few nitrites species survive, while nitrates are the main species stored. This second pathway is called Nitrite route. Therefore, if the storage time is sufficiently long, at the end of both adsorption routes nitrates are the final stored species. Nitrites route occur on Ba sites close to Pt sites, that can subsequently catalyze the oxidation to nitrates [18,25] through monatomic oxygen derived from O₂ or NO₂. Conversely, nitrates route occurs in sites not so close to Pt, through the direct adsorption of NO₂. Furthermore, with increasing temperatures, the formation of more stable nitrates is favored.

However, these two routes are not the only ones can be followed during sorption process. In fact, thanks to availability of oxygen source given by Pt catalyzed spillover reactions, other mechanisms can occur. In those barium sites close to Pt ones, adsorption of NO and NO₂ can proceed through reactions 9 and 10 [3,18,26]:



In all reactions showed the BaO was chosen as representative precursor of nitrites and nitrates species, but in atmosphere with CO₂ and H₂O, also Hydroxides and Carbonates species can exist, substituting the barium oxides.

Pt catalytic activity on NO conversion and spillover reactions has an important role in adsorption process. It influences the NO₂/NO ratio and provides oxygen sources for the adsorption reactions that otherwise would not occur. In fact, a study on Ba/Al₂O₃ formulation [21] found that with gas feeding compositions of NO and O₂, only negligible amounts of NO are adsorbed. On the other hand, in presence of Pt, the adsorption of NO is possible. Therefore, the presence of Pt coating allows other mechanism to occur, enabling the adsorption in wider range of exhaust gas compositions.

1.3.1.2 NO_x reduction

The LNT catalyst is capable to store only a limited quantity of NO_x species on its surface, thus it needs a periodical regeneration to fulfill its role in the nitrogen oxides reduction. The cleaning of catalyst surface can be spontaneous if exhaust gases reach temperatures high enough (above 400°C) to destabilize the adsorbed species. However, regeneration of the trap should not occur through thermal desorption because NO_x species must be reduced prior to reach the atmosphere. Thus, the regeneration of storage capacity is carried out by means of controlled fuel post injections. The use of post-injections leads to CO, HCs and H₂ engine out slip to the downstream components up to the LNT, promoting the reduction. H₂ is the most active reductant at low temperatures, maintaining good performances also at high temperatures. However, it is present in lower quantities in a Diesel engine exhaust than CO and HCs [27,28]. CO and C₃H₆ show less reducing power at low temperatures if compared with H₂. Despite this, at high temperatures, Water Gas Shift (WGS) and Steam Reforming (SR) reactions convert considerable quantities of these two species into H₂, leading to improved performances in NO_x reduction. In fact, in OSC doped and Pt loaded catalysts these two reactions can cause beneficial effects if H₂O is present. In addition to CO, HCs and H₂, also the NH₃ can be used as reductant, which is produced from nitrates/nitrites reduction with other reductants at low temperatures, or directly formed at high temperatures from the Pt catalyzed ammonia production reaction.

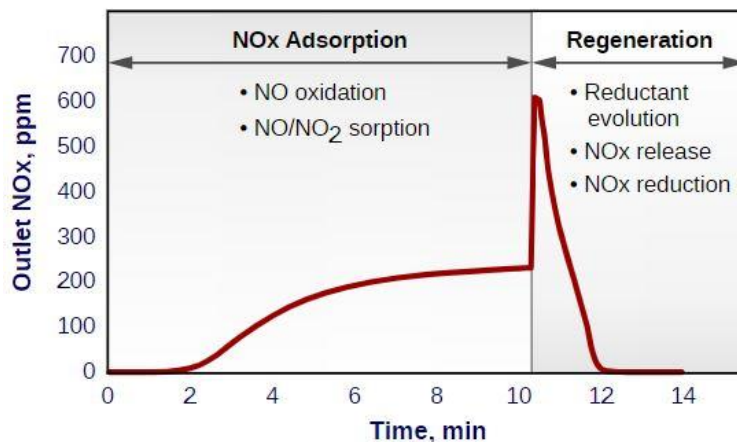


Figure 12 - NO_x release profile in a generic NSR catalyst [17].

As shown in Figure 12, at the start of a regeneration events the release of NO_x from the surface of the catalyst is observed, not always followed by its reduction into N₂. At the lean/rich interfaces NO_x slip occurs, with different intensities and durations depending on temperature and reductant used. The temperature defines the rate of NO_x desorption in correspondence of lean/rich transitions. However, the activation temperatures of reductants

establish the magnitude of NO_x slip. In other words, higher is the reducing power of the available reductant, lower will be the desorption peak value, because the released species will be reduced more rapidly. On the other hand, in presence of poor reducing power elements, the NO_x slips will be enhanced. However, at high temperatures, the instability of adsorbed species usually dominates on reduction reaction rates, leading to high thermal desorption independently from reducing species chosen.

NO_x desorption is promoted by two main coexisting conditions at the start of a rich pulse [18,26]:

- Since the adsorption reaction are influenced by equilibrium, the rapid change of atmosphere composition from lean to rich leads to almost zero partial pressure relative to oxygen and NO_x. Thus, stability of chemical bonds in such rich conditions decreases while the desorption rate rises;
- Exothermic reactions between adsorbed species like oxygen, nitrates/nitrites and reducing agents lead to thermal release and a rapid increase in catalyst surface temperature, which promotes the instability of chemical bonds and thus the release of NO_x.

H₂ can reduce large quantities of NO_x stored species already at low temperatures, but in the range of temperature between 100°C and 150°C almost complete selectivity to ammonia is observed. At temperatures above 200°C the H₂ selectivity to ammonia production decrease in favor of N₂ production [29]. Several studies [28,29,30,31] agree describing reduction process through H₂ with a dual step pathway, with a first step involving the fast reaction between adsorbed species and H₂, leading to formation of ammonia. Then, the second step consists of a slower reaction of the so formed NH₃ with stored NO_x species to form N₂ with almost complete selectivity [29]. The regeneration process by H₂ works as a front traveling through the catalyst. If nitrates/nitrites species are available to be reduced, the two steps reaction involved leads to the double formation of N₂ and NH₃. The ammonia reacts with barium stored species, producing N₂. However, when the front reaches the end of the catalyst, no more stored species are available and the NH₃ slip occurs. The NH₃ slip can be promoted in presence of downstream SCR [29,31], otherwise it should be limited by acting on the duration of rich events. Another undesired phenomenon is the formation of N₂O in low temperature conditions [7].

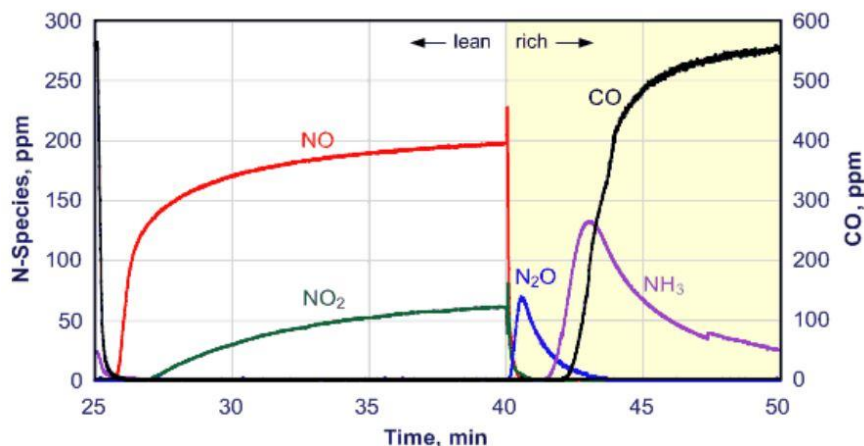


Figure 13 - NSR test, performed at $T = 200^{\circ}\text{C}$, $SV = 30,000 \text{ l/h}$, 15 min lean (300 ppm NO, 10% O_2 , 5% H_2O , 5% CO_2 , balance N_2), 10 min rich (625 ppm CO, 375 ppm H_2 , 5% H_2O , 5% CO_2 , balance N_2) [17].

The hydrogen is the main responsible for NH_3 formation at low temperature, while in case of C_3H_6 as reductant a small amount of NH_3 is produced in the same temperature region. The presence of CO as reductant promotes the production of NH_3 at temperatures around 200°C [28]. At temperatures above 350°C the NH_3 selectivity is almost the same for all reductants species because WGS and SR reactions produce hydrogen from CO and C_3H_6 [30,18]. Also, N_2O is a relevant by-product of nitrites/nitrates reduction process, mainly produced during catalyst regeneration through CO, but also present if H_2 and C_3H_6 are used.

The NO_x reduction by means of C_3H_6 is active starting from 225°C . At lower temperatures reduction reactions with high selectivity to NO occurs, leading to partial nitrites/nitrates reduction and NO evolution. The NO formation is also associated to PtO_x species formed during the lean phase, where Pt sites oxidation is possible. During the subsequent rich phase, propylene reduces the oxidized Pt sites and only once all PtO_x sites have been reduced the reduction process can proceed with higher selectivity to N_2 formation. For temperature higher than $220/230^{\circ}\text{C}$ the reduction of PtO_x sites occurs at higher rate, thus selectivity to N_2 increases [23].

CO is an effective reductant for temperature above 200°C . Experiments with both CO and H_2 as reductants found that CO inhibits the reduction process through H_2 , reducing its performances at low temperatures, because it poisons the Pt sites, which catalyze the release and the reduction process. On the contrary, at high temperatures the poisoning phenomena is reduced [18,32].

1.3.1.3 OSC - Oxygen Storage Capacity

The presence of ceria is helpful both to stabilize the barium dispersion over the washcoat at high temperature and to enable OSC over the catalyst bed during lean phases, promoting the adsorption process and the oxidation reactions. The OSC capacity increases by increasing the exhaust temperature and it saturates between 450°C and 500°C, due to the bulk diffusion limitations [33,34]. During rich events, the O₂ stored in ceria sites oxidizes H₂, CO and HCs and it promotes the WGS and SR, which produce H₂ helping the catalyst regeneration [7]. However, during the regeneration the presence of O₂ on the catalyst surface can reduce the overall LNT efficiency, increasing the overall amount of reductant necessary to complete the reduction of NO_x species [26,35,36]. In fact, prior to reduce the stored elements such as nitrites and nitrates, reductants must consume all the oxygen.

The presence of ceria in the washcoat formulation can also give other beneficial effects. Temperature Programmed Desorption (TPD) tests performed in [37] highlighted that during lean phases Pt/Ceria sites can also compete with barium ones in NO_x adsorption, promoting the storage performance of the catalyst mostly in the temperature range of 200°C- 400°C. Furthermore, ceria doped catalysts show improved barium dispersion. Temperature Programmed Reduction (TPR) experiments show that also NO_x reduction performance is enhanced by the presence of ceria sites. In fact, NO_x captured from Pt/CeO₂ sites results in less stable NO_x adsorbed species, facilitating the regeneration of the catalyst at lower temperatures. Ceria can also prevent barium site from sulfur poisoning, adsorbing these species in place of barium. Furthermore, the sulfur adsorbed by ceria results in less stable species, thus requiring lower temperatures and durations for desulphation events, preventing the catalyst from thermal aging and helping to maintain high conversion efficiencies during catalyst life [36].

1.3.1.4 Performance targets and NO_x absorbers advantages and disadvantages

The LNT technology presents many positive features but some disadvantages too. Advanced washcoat formulations and control strategies enable to reach 70-90% of conversion efficiencies in low load conditions, reaching good performance at low temperatures respect to other NO_x converters like SCR systems [38].

This catalyst does not need extra urea injection for the NO_x conversion, thus the infrastructure is easier respect to SCR systems. The regeneration events last some seconds and usually occur every few minutes. The extra fuel can be injected directly by engine injector with late fuel post injection or adding an extra fuel injector directly upstream of the catalyst, avoiding the oil dilution problem.

The LNT catalyst suffers from sulfur poisoning and requests the use of low sulfur fuel to achieve durable performances. Despite this, occasional desulphation events are necessary, and the high temperatures reached can lead to early washcoat deterioration. The susceptibility of LNT to sulfur poisoning is the most important factor that determines the catalyst lifetime. The required conditions to eliminate sulfur from the catalyst can activate several mechanisms that may affect the performance: precious metals sintering, loss of washcoat surface area and chemical reactions between washcoat elements [36].

The lean/rich cycling and the occasional desulphation events cause an extra fuel consumption, which is around +7% respect to a vehicle equipped with an SCR system [39], corresponding to an increase of CO₂ emissions.

The performances of an LNT system are strictly related to its control strategies, thus the definition and refinement of this control is needful to reduce the fuel consumption and reach the maximum possible efficiency in NO_x conversion. Unfortunately, finding the best control strategy is not so easy because several chemical mechanisms are involved. Furthermore, each LNT washcoat requires a specific regeneration strategy depending on formulation, engine application and aftertreatment layout.

As seen in the previous paragraph, one of the most promising solutions to fulfill the ULN targets for HD engines is the PNA. The PNA does not require the definition of an active regeneration strategy to manage the DeNO_x events, eliminating fuel/CO₂ penalties. Furthermore, it requires less PGM loading and usually adsorbing material are different from Barium/Rare-Earth metals to allow free thermal desorption at lower temperatures. This potentially can lead to the reduction of costs, in particular for HD applications, where high catalyst volumes are required. However, the different materials used for PNA show lower NO_x storage capacity respect the ones used in LNT technology.

LNTs have been used as stand-alone in several light-duty diesel aftertreatment applications to comply with NO_x emission regulations and they can be integrated with NO_x converts like SCR or SCR-F. Conversely, PNA catalysts are a just-born technology. They show high potential in NO_x reduction during cold starts, but further investigations must be carried out to evaluate their performance in all conditions.

2 Experimental activity

This chapter presents the experimental test campaigns on the Low Temperature (LT) LNT which were used for the model calibration and validation.

The LT-LNT is a technology capable to guarantee high NO_x conversion efficiencies in the low temperature region thanks to the high PGM loading, which allows increased NO to NO₂ conversion and consequently high adsorption of NO. Moreover, the high PGM loading reduces the light-off temperature of CO/HCs. The characteristics of the LT-LNT this work focused on are summarized in Table 10.

	Full scale	Reactor scale
Type	<i>Low Temperature LNT</i>	<i>Low Temperature LNT</i>
PGM loading [g/ft³]	120	120
PGM ratio (Pt : Pd : Rh)	103 : 12 : 5	103 : 12 : 5
Substrate material	<i>Cordierite</i>	<i>Cordierite</i>
Cell density [cpsi]	400	400
Wall thickness [mil]	4.5	4.5
Aging	<i>Sulfur-free oven-aged (20h/800degC, 10% H₂O+air)</i>	<i>Sulfur-free oven-aged (20h/800degC, 10% H₂O+air)</i>

Table 10 - LNT technology.

The component was tested at reactor scale level on a Synthetic Gas Bench (SGB) in steady state conditions by General Motors Research and Development (GM R&D) in North America (for the description of SGB see the work of R. Mahsa [7]). The samples used for the SGB testing activity are depicted in Figure 14.

The Full-Scale component experimental activity consisted of 23 WLTC and 4 RDE cycles, performed at General Motors Torino over a chassis dynamometer (for the description of dyno bench see the work of C. Cubito [6]).

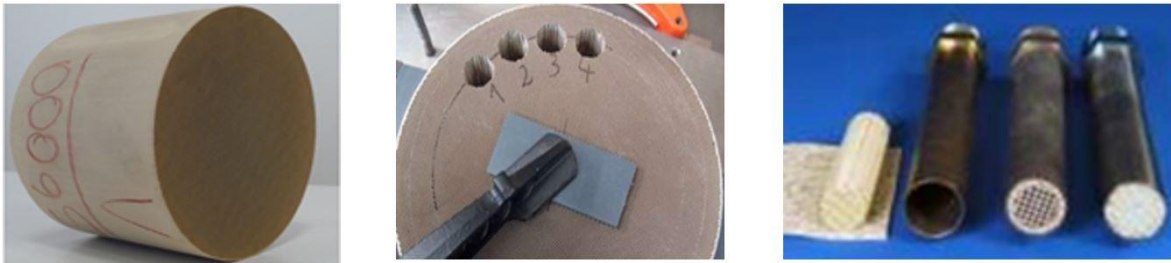


Figure 14 - Samples extraction from full scale LNT catalyst.

Both the reactor scale and the full-scale component are referred to the same aging status.

2.1 Steady state tests

The SGB experimental activity has the purpose to identify the driving chemical reactions of the catalyst. The tests on the sample were carried out with controlled species concentrations, temperatures and flow rates. Inlet species concentrations have been carefully selected in order to decouple the main chemical phenomena of the LNT. However, in some cases it was difficult to isolate all the chemical effects.

Four type of tests were executed during experimental activity:

- *Light-Off (LO)* tests;
- *Temperature Programmed Desorption (TPD)* tests;
- *Oxygen Storage Capacity (OSC)* tests;
- *NO_x Storage and Reduction (NSR)* tests.

All the tests were performed on a sulphur free core sample.

2.1.1 LO tests

The goal of the LO test is the characterization of oxidation rates of LNT reductants as function of catalyst temperature. The tests consists into different combination of reductants (CO, HCs and H₂) in lean conditions (High O₂ concentrations) at the inlet of LNT, increasing the inlet temperature from 100°C to 500°C with a gradient of 5°C/min, as illustrated in Figure 15.

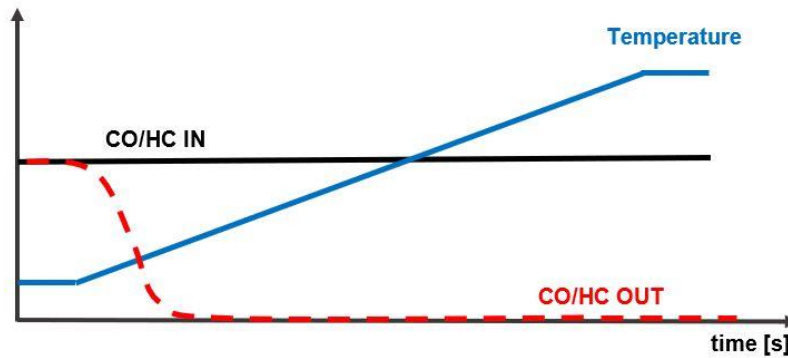


Figure 15 - CO and NMHC tailpipe traces during a generic light-off test.

The use of different concentrations of reactants, from Low to High, should be helpful to describe the competition and the inhibitions effects between the species during the light-off. The full test matrix is reported in Table 11.

The characterization required the combination of different concentrations (%Vol) of reductants and different Space Velocities (SV) to explore the full operating domain of the LNT during the light off. A background gas constituted by O₂, CO₂, and H₂O was used during the tests, with concentrations values representative of the average operating conditions of a Diesel engine.

Test n°	Space Velocity	NO	NO ₂	O ₂	CO ₂	H ₂ O	H ₂	CO	HC
1	Low	0	0	High	Medium	Medium	-	Low	Low
2	High	0	0	High	Medium	Medium	-	Low	Low
3	Low	0	0	High	Medium	Medium	-	Medium	Medium
4	Low	0	0	High	Medium	Medium	-	High	High
5	High	0	0	High	Medium	Medium	-	High	High
6	Low	0	0	High	Medium	Medium	Low	High	High
7	High	0	0	High	Medium	Medium	Low	High	High
8	Low	0	0	High	Medium	Medium	Medium	High	High
9	Low	Medium	0	High	Medium	Medium	-	Low	Low
10	Low	Medium	0	High	Medium	Medium	-	-	-
11	Low	Low	Low	High	Medium	Medium	-	Low	Low
12	Low	Low	0	High	Medium	Medium	-	Medium	Medium
13	Low	Low	0	High	Medium	Medium	-	High	Medium
14	Low	Low	0	High	Medium	Medium	Low	High	High
15	Low	Low	0	Low	High	High	-	Extra-High	Extra-High
16	Low	Low	0	Low	High	High	Extra-High	Extra-High	Extra-High

Table 11 - Temperature and inlet species concentration of LO experimental tests.

2.1.2 OSC tests

The aim of OSC experimental protocol is to evaluate the quantity of O_2 stored on the catalyst bed. These tests consist of alternated lean/rich periods performed at constant temperature, ranging from 150°C up to 400°C , as depicted in Figure 16.

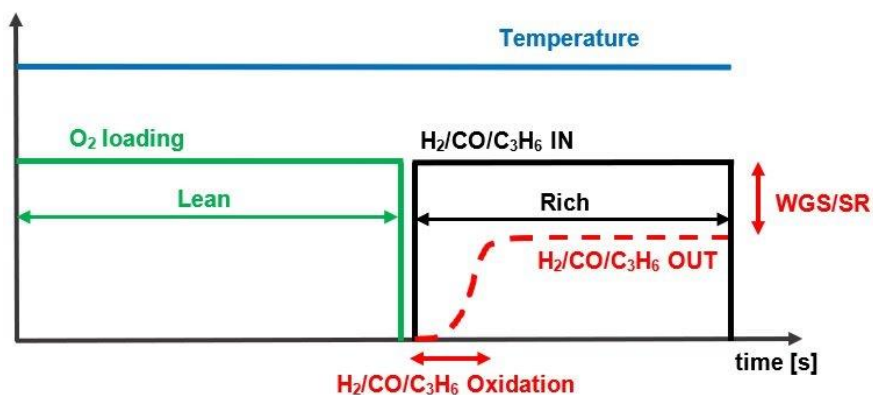


Figure 16 - Chemical behavior during a generic OSC test.

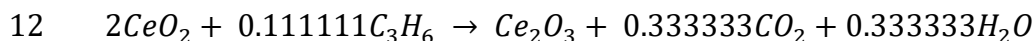
During lean phases the ceria sites store oxygen, while in the following rich pulses the stored O_2 is consumed through the oxidation of reductants. During rich phases the O_2 feeding is stopped and different concentrations of H_2 , CO and C_3H_6 are used to characterize the OSC. Due to some limitations of the experimental layout, the H_2 concentration was not measured during the tests. Furthermore, for the tests with lean/rich cycling, such as OSC and NSR tests, only propylene was used as hydrocarbon. The list of tests used for the OSC characterization is reported in Table 12.

<i>Lean phase</i>										
<i>Test n°</i>	<i>Temperature [degC]</i>	<i>Space Velocity</i>	<i>NO</i>	<i>NO₂</i>	<i>O₂</i>	<i>CO₂</i>	<i>H₂O</i>	<i>H₂</i>	<i>CO</i>	<i>C₃H₆</i>
1	150	Low	-	-	High	Low	Low	-	-	-
2	150	Low	-	-	High	Low	Low	-	-	-
3	200	Low	-	-	High	Low	Low	-	-	-
4	200	Low	-	-	High	Low	Low	-	-	-
5	200	Low	-	-	High	Low	Low	-	-	-
6	250	Low	-	-	High	Low	Low	-	-	-
7	250	Low	-	-	High	Low	Low	-	-	-
8	250	Low	-	-	High	Low	Low	-	-	-
9	250	Low	-	-	High	Low	Low	-	-	-
10	300	Low	-	-	High	Low	Low	-	-	-
11	300	Low	-	-	High	Low	Low	-	-	-
12	400	Low	-	-	High	Low	Low	-	-	-
13	400	Low	-	-	High	Low	Low	-	-	-
<i>Rich phase</i>										
1	150	Low	-	-	-	Low	Low	-	Medium	-
2	150	Low	-	-	-	Low	Low	-	-	Medium
3	200	Low	-	-	-	Low	Low	Medium	-	-
4	200	Low	-	-	-	Low	Low	-	Medium	-
5	200	Low	-	-	-	Low	Low	-	-	Medium
6	250	Low	-	-	-	Low	Low	Medium	-	-
7	250	Low	-	-	-	Low	Low	-	Medium	-
8	250	Low	-	-	Low	Low	Low	-	Extra-high	-
9	250	Low	-	-	-	Low	Low	-	-	Medium
10	300	Low	-	-	-	Low	Low	-	Medium	-
11	300	Low	-	-	-	Low	Low	-	-	Medium
12	400	Low	-	-	-	Low	Low	-	Medium	-
13	400	Low	-	-	-	Low	Low	-	-	Medium

Table 12 - Temperature and inlet species concentration of OSC experimental tests (Lean/Rich Phases).

In OSC dataset also blank tests were recorded. The blank tests were carried out without the catalyst sample, with the aim to characterize the valve dynamic and reproduce it during the reactor test. This is very important for the correct characterization of the OSC test, because the O₂ consumption during the rich phase is fast and the incorrect identification of the transition phase could affect the quality of results.

The estimation of OSC is an indirect procedure, because the storage capacity is assessed from the oxidation of reactants during the rich phase. Furthermore, the procedure was applicable only to test performed with CO and C₃H₆ as reactants, because H₂ measurements were not available. Analyzing the stoichiometry of oxygen consumption reactions allows to extrapolate the quantity of oxygen stored. The consumption of O₂ stored in ceria sites is described by reaction 11 and reaction 12:



In case of experiments with CO as reductant, there are two paths to estimate the average OSC on a single rich phase:

1. Calculate the difference between the inlet and outlet CO₂ emissions;
2. Calculate the CO consumption based on the difference between the inlet and outlet concentrations.

In case of tests with C₃H₆ as reductant, there are three possible ways to estimate the OSC. Following the stoichiometry of the reaction 12, the O₂ storage can be calculated as:

1. Production of H₂O moles;
2. Production of CO₂ moles;
3. Calculation on C₃H₆ consumption, expressed as the difference between the inlet and outlet concentrations.

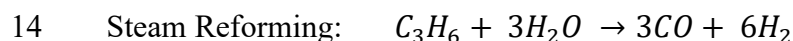
Once the consumption of CO/C₃H₆ and the production of CO₂/H₂O are estimated, it is possible to assess the OSC:

1. In case of CO as reductant, the correspondence between O₂/CO consumed and CO₂ produced is defined according to the stoichiometry: 1 mole of CO₂ produced corresponds to 0.5 moles of O₂ consumed;
2. 1 mole of CO oxidized corresponds to 0.5 moles of O₂ consumed.

In case of C₃H₆ as reductant the OSC can be estimated as:

1. 1 mole of CO₂ produced corresponds 0.66 moles of O₂ consumed;
2. 1 mole of H₂O produced corresponds 0.66 moles of O₂ consumed;
3. 1 mole of C₃H₆ consumed corresponds 4.5 moles of O₂ consumed;

Unfortunately, in the mid/high temperature region WGS and SR reactions can contribute to the consumption respectively of CO and C₃H₆. The stoichiometry of these two reactions is illustrated in equations 13 and 14:



In case of CO the WGS is enabled at temperatures above 200°C. The only way to discern between oxidation and WGS is the measure of H₂ at the outlet of LNT, which is not available in this case. In the case of C₃H₆, for temperatures higher than 300°C, the effect of SR is not

negligible. Thus, the consumed C_3H_6 by means of SR can be estimated through the analysis of CO outlet emissions. However, at temperatures above $300^\circ C$ the WGS is active and it contributes to the consumption of CO produced by SR.

The following hypothesis was applied to avoid the uncertainty on the OSC estimation: if the temperature is sufficiently high the OSC is independent from the type of reductant. Therefore, if the inlet temperature is above $200^\circ C$ the OSC estimated from C_3H_6 was assumed equal to equivalent tests with the CO as reductant, avoiding the problem of WGS. On the contrary, if the temperature is below $200^\circ C$ the OSC has been estimated according to the available experimental data.

2.1.3 TPD tests

TPD test protocol allows the characterization of the adsorption and desorption of NO_x relative to barium sites, as depicted in Figure 17.

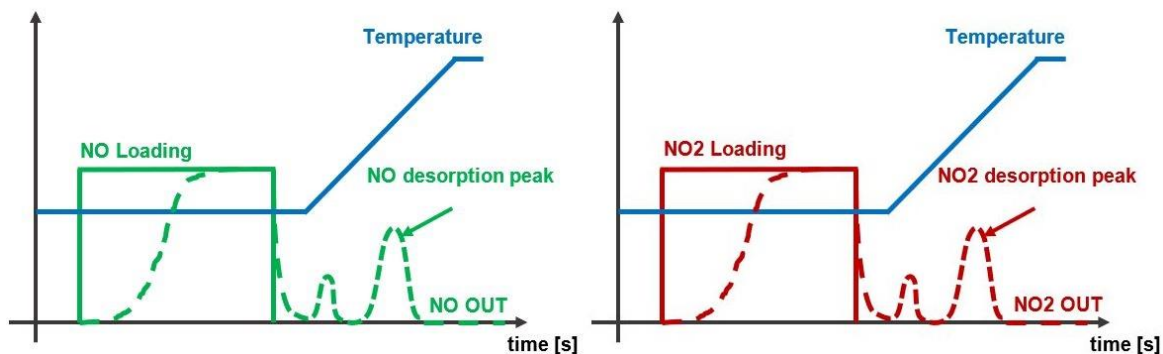


Figure 17 - Simplified example of NO and NO_2 in/out traces during a TPD experiment.

NO_x storage tests are mainly divided into two phases:

1. the first phase is driven by NO/NO_2 feeding until the reaching of storage saturation;
2. the second phase shows no NO_x at the inlet in order to monitor the desorption.

The adsorption phase is performed at constant temperature, ranging from $100^\circ C$ to $400^\circ C$ as illustrated in Table 13. During the desorption phase, the temperature is increased from the starting value up to $500^\circ C$ with a constant gradient of $5^\circ C/min$. At the end of the temperature ramp, a short rich purge is done to clean the sample core from any residual NO_x .

The complete characterization of the absorption/desorption requested a large operating domain, characterized by different NO_2/NO_x ratios and SVs, as depicted in Table 13. As for

the LO tests, CO₂, H₂O and O₂ were added to the feeding gas to be representative of the average Diesel exhaust composition.

Test n°	Constant Temperature phase [degC]	Space Velocity	NO	NO ₂	O ₂	CO ₂	H ₂ O	HC	CO
1	100	Low	Medium	-	Medium	Medium	Medium	-	-
2	125	Low	Medium	-	Medium	Medium	Medium	-	-
3	125	Low	Low	Low	Medium	Medium	Medium	-	-
4	125	Low	Medium	-	Medium	Medium	Medium	High	High
5	150	Low	Medium	-	Medium	Medium	Medium	-	-
6	150	Low	-	-	Medium	Medium	Medium	-	-
7	200	Low	Medium	-	Medium	Medium	Medium	-	-
8	200	High	Medium	-	Medium	Medium	Medium	-	-
9	200	Low	Low	Low	Medium	Medium	Medium	-	-
10	200	Low	Medium	-	Medium	Medium	Medium	High	High
11	225	Low	Medium	-	Medium	Medium	Medium	-	-
12	250	Low	Medium	-	Medium	Medium	Medium	-	-
13	250	High	Medium	-	Medium	Medium	Medium	-	-
14	250	Low	Medium	-	Low	Medium	Medium	-	-
15	250	Low	Medium	-	High	Medium	Medium	-	-
16	250	Low	Medium	-	Low	High	High	-	-
17	250	Low	Medium	-	High	Medium	Medium	-	-
18	250	Low	High	-	Medium	Medium	Medium	-	-
19	250	Low	Low	-	Medium	Medium	Medium	-	-
20	250	Low	Low	Low	Medium	Medium	Medium	-	-
21	250	Low	Medium	-	Medium	Medium	Medium	High	High
22	275	Low	Medium	-	Medium	Medium	Medium	-	-
23	275	Low	Medium	-	Medium	Medium	Medium	-	-
24	300	High	Medium	-	Medium	Medium	Medium	-	-
25	300	Low	Low	-	Medium	Medium	Medium	-	-
26	300	Low	High	-	Medium	Medium	Medium	-	-
27	300	Low	Medium	-	Low	Medium	Medium	-	-
28	300	Low	Medium	-	High	Medium	Medium	-	-
29	300	Low	Medium	-	Low	High	High	-	-
30	300	Low	Medium	-	High	Low	Low	-	-
31	350	Low	Medium	-	Medium	Medium	Medium	-	-
32	400	Low	Medium	-	Medium	Medium	Medium	-	-
33	450	Low	Medium	-	Medium	Medium	Medium	-	-

Table 13 - Temperature and inlet species concentration of TPD experimental tests.

Some of the tests described in Table 13 were carried out also with CO and HCs at the inlet of LNT sample to characterize the interaction between adsorption/desorption and reduction.

2.1.4 NSR Tests

NSR test protocol summarizes the behavior of a LNT catalyst, since it gives the possibility to monitor the NO_x storage in lean conditions, the NO_x desorption and the reduction in rich atmosphere, as shown in Figure 18.

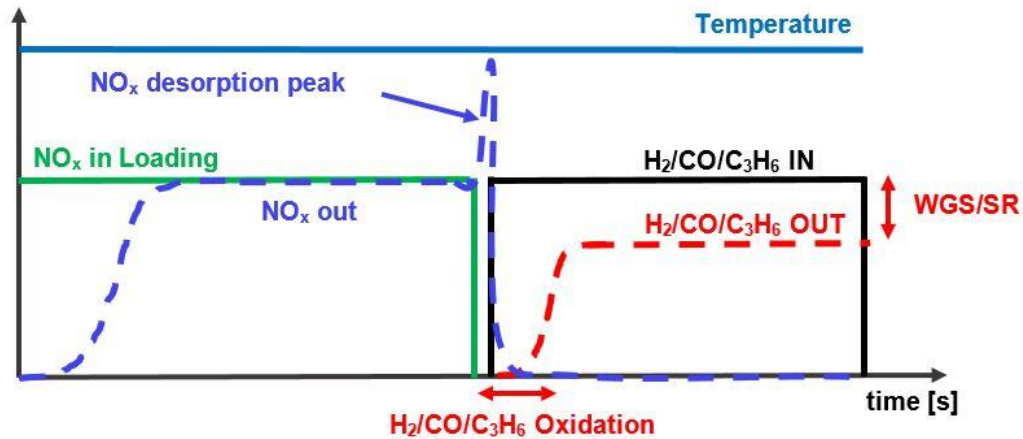


Figure 18 - Generic NSR test behavior.

As previously seen in OSC and TPD tests, during lean phase O_2 and NO_x are adsorbed respectively by ceria and barium sites until catalyst saturation. While in the following rich phase, the reductants in the feeding gas consume the stored NO_x and O_2 . As previously mentioned in paragraph 2.1.2, due to SGB limitations, only propylene was used as hydrocarbon for the reducing phases.

All NSR tests were carried out at constant inlet temperature, ranging from 200 °C to 350 °C. The boundary conditions of NSR tests are collected in Table 14.

<i>Lean phase</i>										
<i>Test n°</i>	<i>Temperature [degC]</i>	<i>Space Velocity</i>	<i>NO</i>	<i>NO₂</i>	<i>O₂</i>	<i>CO₂</i>	<i>H₂O</i>	<i>H₂</i>	<i>CO</i>	<i>C₃H₆</i>
1	200	Low	Medium	-	High	Medium	Medium	-	-	-
2	200	Low	Medium	-	High	Medium	Medium	-	-	-
3	200	Low	Medium	-	High	Medium	Medium	-	-	-
4	250	Low	Medium	-	High	Medium	Medium	-	-	-
5	250	Low	Medium	-	High	Medium	Medium	-	-	-
6	250	Low	Medium	-	High	Medium	Medium	-	-	-
7	350	Low	Medium	-	High	Medium	Medium	-	-	-
8	350	Low	Medium	-	High	Medium	Medium	-	-	-
9	350	Low	Medium	-	High	Medium	Medium	-	-	-
<i>Rich phase</i>										
1	200	Low	-	-	-	Medium	Medium	High	-	-
2	200	Low	-	-	-	Medium	Medium	-	High	-
3	200	Low	-	-	-	Medium	Medium	-	-	High
4	250	Low	-	-	-	Medium	Medium	High	-	-
5	250	Low	-	-	-	Medium	Medium	-	High	-
6	250	Low	-	-	-	Medium	Medium	-	-	High
7	350	Low	-	-	-	Medium	Medium	High	-	-
8	350	Low	-	-	-	Medium	Medium	-	High	-
9	350	Low	-	-	-	Medium	Medium	-	-	High

Table 14 - Temperature and inlet species concentration of NSR experimental tests (Lean/Rich Phases).

During the lean phase the concentrations of CO, H₂O and O₂ are representative of standard operating conditions of a Diesel engine. During the rich events the NO and O₂ feedings are stopped to monitor the consumption of nitrates/nitrites stored into barium sites and consumption of oxygen stored in ceria sites. Unfortunately, no blank tests were available to characterize the dynamics of the feeding valve. To overcome this problem, the valve dynamics was modelled as follows:

- Valve Opening: 15 $f(t) = A * (1 - e^{-\frac{t}{\tau}})$;
- Valve Closing: 16 $f(t) = A * e^{-\frac{t}{\tau}}$.

where:

- **A**: is the steady state amplitude (or the nominal value for inlet species concentration);
- **τ**: is the system time constant.

An example of the resulting traces is reported in Figure 19.

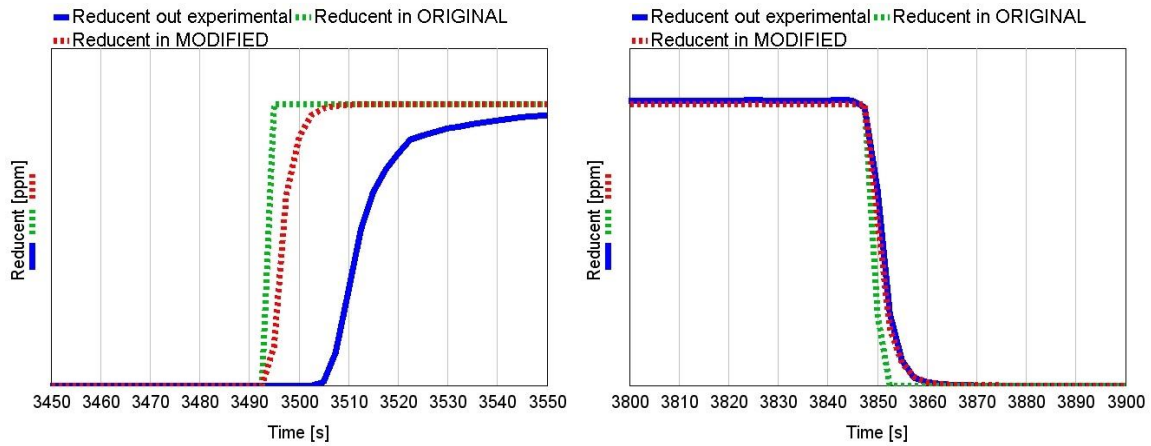


Figure 19 - Original inlet reductant trace (green dashed line) compared with experimental out reductant trace (blue continuous line). The red dashed line represents the inlet reductant profile after the valve dynamic correction.

2.2 Transient tests

Transient tests were carried out on a chassis dyno over WLTC and RDE cycles with the full scale LNT coupled with a medium size Diesel engine. The characteristics of the vehicle are reported in Table 15.

<i>Vehicle application</i>	<i>Mid-size passenger car</i>
<i>Engine</i>	<i>1.6 l Diesel engine Turbo charged, 4 cylinders in line</i>
<i>Transmission</i>	<i>Manual – 6 gears</i>

Table 15 - Main characteristics of vehicle used for transient LNT full scale testing.

The list of WLTC and RDE cycles considered for the LNT model calibration and validation are listed in Table 16 and Table 17.

Cycle Name	Start Coolant Temperature	Preconditioning Procedure	DeNOx Events
WLTC 1	23°C	Regeneration + DeNOx events	NO
WLTC 2	23°C	Just cool down	NO
WLTC 3	23°C	Regeneration + DeNOx events	NO
WLTC 4	23°C	Just cool down	NO
WLTC 5	23°C	Regeneration + DeNOx events	NO
WLTC 6	23°C	Just cool down	NO
WLTC 7	23°C	Just cool down	NO
WLTC 8	23°C	Regeneration + DeNOx events	NO
WLTC 9	23°C	Just cool down	NO
WLTC 10	23°C	Just cool down	NO
WLTC 11	23°C	Regeneration + DeNOx events	NO
WLTC 12	90°C	Without cool down	NO
WLTC 13	23°C	Regeneration + DeNOx events	NO
WLTC 14	90°C	Without cool down	NO
WLTC 15	23°C	Regeneration + DeNOx events	YES
WLTC 16	23°C	Just cool down	YES
WLTC 17	90°C	Without cool down	YES
WLTC 18	23°C	Regeneration + DeNOx events	YES
WLTC 19	23°C	Just cool down	YES
WLTC 20	90°C	Without cool down	YES
WLTC 21	23°C	Regeneration + DeNOx events	YES
WLTC 22	23°C	Just cool down	YES
WLTC 23	90°C	Without cool down	YES

Table 16 - WLTC full scale experimental dataset.

Cycle Name	Start Coolant Temperature	Preconditioning Procedure	DeNOx Events
RDE 1	23°C	Regeneration + DeNOx events	NO
RDE 2	23°C	Regeneration + DeNOx events	NO
RDE 3	23°C	Regeneration + DeNOx events	YES
RDE 4	23°C	Regeneration + DeNOx events	YES

Table 17 - RDE full scale experimental dataset.

3 LT-LNT modeling and calibration

This chapter introduces the methodology adopted to model the LT-LNT catalyst, using a global kinetic approach in GT-Suite environment, and the calibration procedure based on experimental data from SGB at reactor scale level, described at paragraph 2.1.

3.1 Modeling approach for automotive catalysts

The use of mathematical models is widely exploited to reduce design time and costs [7]. In case of aftertreatment systems modelling, it is possible to find different approaches, which can be grouped into three categories:

1. Maps/Lookups:
 - Efficiency maps based on temperature and exhaust mass flow rate;
 - Simple implementation;
 - Large experimental effort for map characterization.
2. Global kinetic models:
 - Overall reaction rates are developed to capture the experimental evidence;
 - Inhibition functions are used to model the interaction/competition between the species at the catalyst surface;
 - Few numbers of reactions with selected species solved;
 - Leads to the development of effective models which generally represent a good compromise between achieved accuracy, experimental data needed for the development and computational effort.
3. Micro-kinetic models:
 - All the reaction steps (formation of intermediates) are considered;
 - High number of reactions with a lot of species to be solved;
 - More rigorous from a physical prospective, but difficult to calibrate.

3.2 Aftertreatment 1-D modeling

The modelling approach used for the LNT catalyst is based on a Global Kinetic 1D modelling in GT-Suite environment [40].

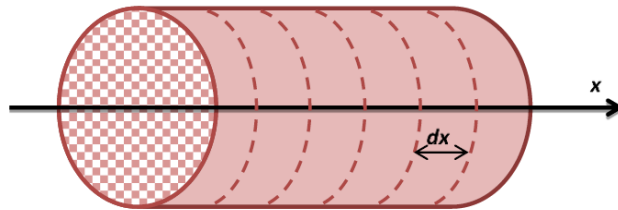


Figure 20 - Volume discretization along component length [13].

The GT-Suite 1D aftertreatment model is based on the following assumptions [40]:

1. Consider only variations along the catalyst length and flow direction (x);
2. Neglect non-homogeneity and non-uniformity of flow and thermal field in the cross-section;
3. Quasi-steady approximation is applied, since the resident time of the gas in the catalyst volume is much shorter than the time scale of interest (which is of the order of seconds);
4. Governing equations considered: continuity, momentum, solid and gas energy balances;
5. Global kinetic mechanism for the reactions is considered;
6. Diffusion between gas and washcoat is considered (external diffusion);
7. Ideal gas equation assumption for the gas phase;
8. Reaction rate in Arrhenius form;
9. Fully developed laminar flow is assumed through catalyst channel.

3.2.1 Thermal modeling

GT-Suite allows to model the thermal features of the catalyst, considering the heat exchange between the gas and the walls and the thermal loss to the external environment. Three levels of details are available to account for external heat loss: a simplified way, an intermediated

approach and a detailed one. As recommended by GT manual the intermediated approach was chosen for this 1-D reactor model. In this case some quantity needs to be specified, like the external ambient temperature, the external convection coefficient and the thermal properties of the various layers composing the catalyst brick, as depicted from Figure 21. In this work the thermal properties of the cordierite substrate, the alumina based washcoat, the polymer catalyst insulation and the metallic support are available from software library. Defined these data, the solver can predict with enough precision the catalyst thermal behavior. As shown in Figure 21, the LNT this study was focused on required only one washcoat layer to be accounted for, but the software allows to model up to two washcoat layers, so advanced aftertreatment components like SCR-F and dual-layer LNT-SCR can be modeled as well.

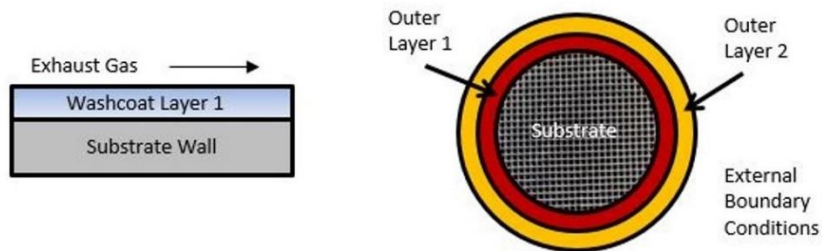


Figure 21 - Simplified representation of thermal intermediate approach modeling [40].

3.2.2 Chemical modeling

The design of an LNT model requires the description of several chemical phenomena and consequently a large number of chemical reactions should be defined and calibrated. In this case the LT-LNT is modelled based on 41 chemical reactions and 22 inhibitions functions, which are used to represent the competition between species or to shape specific phenomena based on concentration of reactants and temperature.

3.3 Calibration procedure

The baseline model was inherited from the previous studies of R. Mahsa [7] and F. Millo et al. [19]. The chemical kinetic structure was modified in order to comply with experimental evidence. In particular, several changes were made in terms of NO_x storage mechanism. The calibration of the LNT chemical model was initially done based on a trial and error approach. The refinement of baseline calibration was then performed based on Genetic Algorithm tool available in GT-Suite [40].

The modelling approach in GT-Suite requests the definition of reactions rates based on the Arrhenius form as illustrated in equations 17 and 18:

$$17 \quad K = Ae^{\frac{-E_a}{RT}}$$

$$18 \quad R = K * \{C\} * G(i) * \theta_i$$

where:

- A: Pre-exponent Multiplier;
- E_a: Activation Energy in J/mol;
- T: the temperature in K;
- R: the ideal gas constant J/mol*K;
- K: Kinetic constant;
- R: Reaction Rate;
- {C}: Concentration;
- G(i): inhibition function;
- θ_i: Coverage expression.

The calibration process consists into the definition of the parameters A, E_a and of the inhibition functions capable to minimize the error between the experimental measure and the simulation results. The Arrhenius plot, which has on the X-axis the inverse of the catalyst inlet temperature [K] multiplied by 1000 and on Y-axis the natural logarithm of the reaction rate, can be used to find the best fittings at all temperatures as described in Figure 22. This method is helpful when experimental dataset consists of isothermal tests performed at several temperatures.

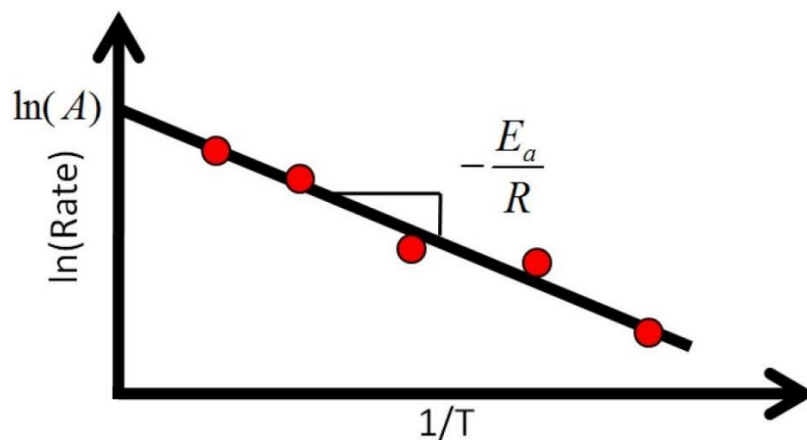


Figure 22 - Arrhenius plot: red dots represent reaction rate in correspondence of different temperatures, the black line represents the interpolating line used by calibrator to match rates at all temperatures [40].

3.3.1 Reactions over PGM sites

The reactions representative of the LO, WGS and SR over PGM sites are reported in Table 18.

	Reaction	Rate Expression
1	$CO + 0.5O_2 \rightarrow CO_2$	$r_1 = k_1 \frac{C_{CO}C_{O_2}}{G_1G_2G_{26}}$
2	$C_3H_6 + 4.5O_2 \rightarrow 3CO_2 + 3H_2O$	$r_2 = k_2 \frac{C_{C_3H_6}C_{O_2}}{G_1G_2}$
3	$C_8H_{10} + 10.5O_2 \rightarrow 8CO_2 + 5H_2O$	$r_3 = k_3 \frac{C_{C_8H_{10}}C_{O_2}}{G_1G_2}$
4	$C_{12}H_{26} + 18.5O_2 \rightarrow 12CO_2 + 13H_2O$	$r_4 = k_4 \frac{C_{C_{12}H_{26}}C_{O_2}}{G_1G_2}$
5	$H_2 + 0.5O_2 \rightarrow H_2O$	$r_5 = k_5 \frac{C_{H_2}C_{O_2}}{G_1G_2}$
6	$H_2O + CO \rightarrow CO_2 + H_2$	$r_6 = k_6 \frac{(C_{CO}C_{H_2O} - \frac{C_{H_2}C_{CO_2}}{G_4})}{G_1G_2G_{23}}$

7	$C_3H_6 + 3H_2O \rightarrow 3CO + 6H_2$	$r_7 = k_7 \frac{C_{C_3H_6} C_{H_2O}}{G_1 G_2}$
8	$NO + 0.5O_2 \rightarrow NO_2$	$r_8 = k_8 \frac{(C_{NO} C_{O_2} - C_{NO_2} G_3)}{G_1 G_{22} G_{28}}$
9	$NO + 2.5H_2 \rightarrow NH_3 + H_2O$	$r_9 = k_9 \frac{C_{NO} C_{H_2}}{G_1 G_2 G_{17}}$

Table 18 - Light-Off reactions over PGM sites.

Reactions from 1 to 5, and 8 in Table 18, are representative of oxidation of products from incomplete diesel combustion process such as: CO, H₂, and HCs. The speciation of HCs on a C1 basis is expressed as: 20% of light weight HC and 80% of heavy weight hydrocarbons. The light-weight fraction is represented with C₃H₆ (Propylene), the heavy portion is split into 1/3 of C₈H₁₀ (Xylene) and 2/3 of C₁₂H₂₆ (Dodecane).

Reactions 6 and 7 in Table 18 correspond to WGS and SR reactions. Reaction 9 account for ammonia (NH₃) production, occurring at high temperatures and in presence of both nitric oxide and H₂.

3.3.1.1 CO and HCs oxidation in lean conditions

CO oxidation cannot be associated to only one reaction. Several reactions lead to CO consumption. In this work, the decision was to initially calibrate direct CO oxidation by oxygen in the gas flow, neglecting both the CO oxidation by oxygen stored on ceria sites and the effect of WGS. This assumption should be reasonable, since in lean conditions the contribute of OSC to CO oxidation is negligible. Furthermore, Light-Off tests start from temperatures below 100°C, as depicted in Figure 23, and all the CO fluxed into the catalyst is oxidized by oxygen in the flow prior than WGS reaction has reached its activating temperature.

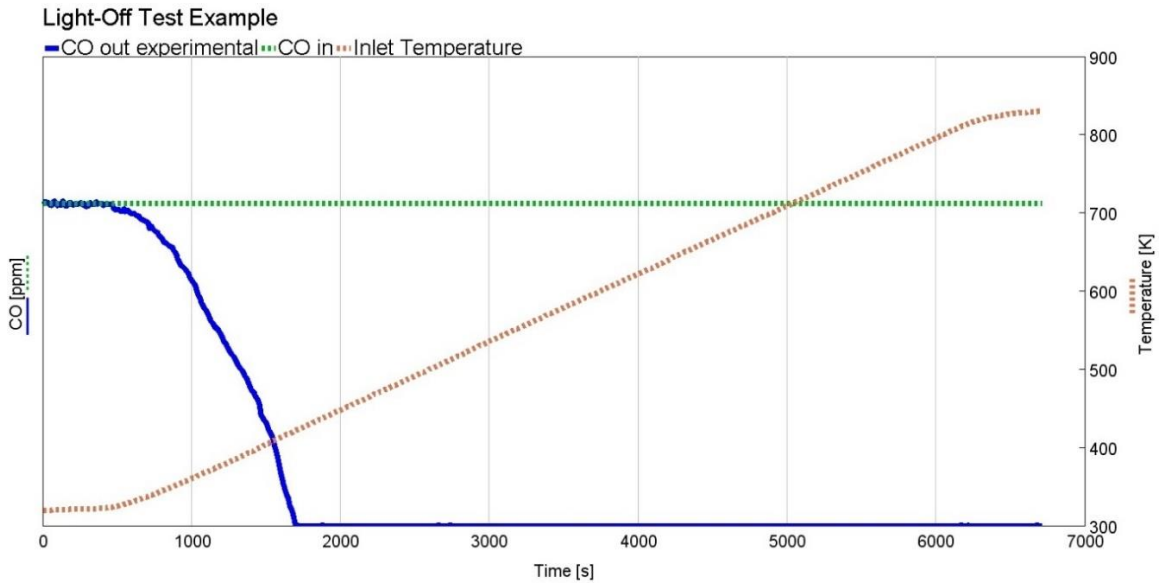


Figure 23 - Example of a LO test with CO as inlet species. The green dashed line represents the inlet concentration, while the blue line the outlet one. The orange dotted line represents the temperature profile.

The same approach was applied to the HCs oxidation. SR and C₃H₆ oxidation due to OSC were neglected.

The calibration activity was done manually based on Arrhenius plot for all reactions considered. The resulting Arrhenius plot is reported in Figure 24: it is possible to observe that the CO has a lower LO temperature and a smoother increase of reaction rate than HCs. Since hydrogen was not available in the SGB dataset, calibration of H₂ oxidation was left as it was in the baseline GT-SUITE model and is not showed.

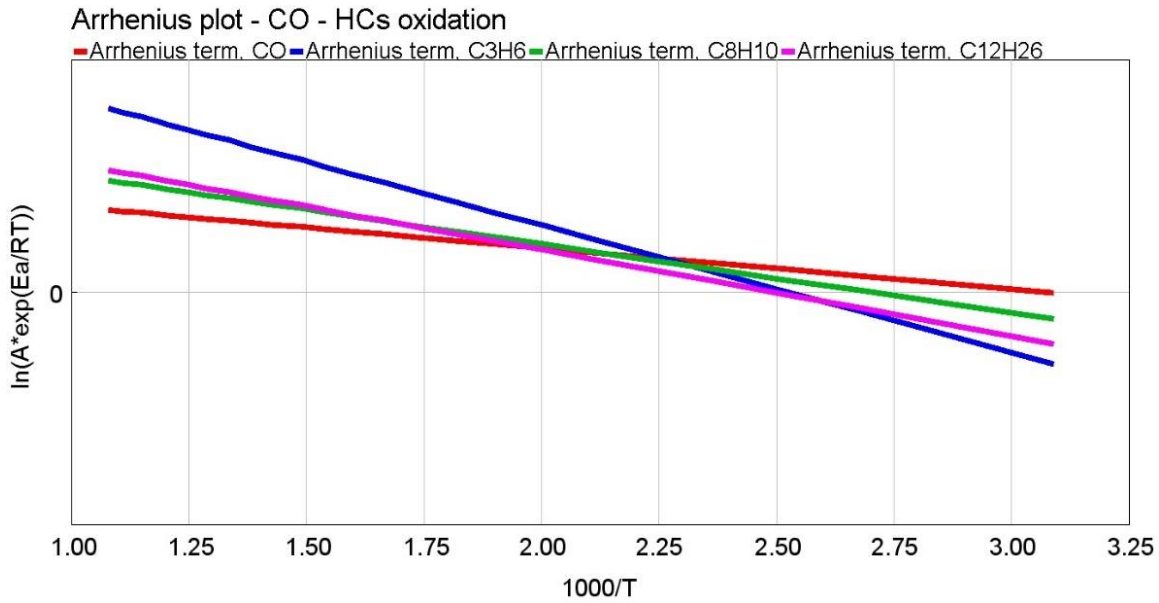


Figure 24 - Arrhenius terms associated to CO and HCs oxidation reactions. The red line represents the reaction rate for CO oxidation, the blue line depicts the C₃H₆ one, the green line refers to C₈H₁₀ oxidation rate and the pink line illustrates the oxidation rate for C₁₂H₂₆.

CO and HCs oxidations are self-inhibited reactions. In other words, the two species compete on PGM site for the catalytic activity and this effect is more stressed when the concentrations of these two species increase, because the number of sites available reduces. Using a global kinetic approach, this phenomenon is modelled with inhibitions functions named G1 and G2, (Table 18). In particular, G1, which is reported in equation 19, is a “Voltz-type” inhibition function [7] and it is representative of a series of phenomena, described by 3 different sub-functions.

$$19 \quad G_1 = f_1(C_{CO}) * f_2(C_{HC}) * f_3(C_{CO}, C_{HC})$$

- f_1 : accounts for CO self-inhibition effect;
- f_2 : consider the C₃H₆ self-inhibition effect;
- f_3 : take into account the competitive effect of the two species.

G2 takes care of NO inhibition effect on all oxidation reactions occurring on PGM sites, while the inhibition function G26, reported in reaction 1 of Table 18, inhibits the oxidation of CO at low temperatures.

3.3.1.2 NO oxidation

The NO oxidation (reaction 8 of Table 18) was calibrated based on TPD tests. In particular, experiments carried out at temperature below 300°C were used to improve the calibration of oxidation reaction, because at high temperatures the NO oxidation is limited by thermodynamic equilibrium, represented by means of the inhibition function G3. The correct modelling of NO oxidation requests the definition of an inhibition function, called G22, which limits the NO oxidation at temperatures below 200°C. The resulting Arrhenius plot is reported in Figure 25. The inhibition function G28 reported in Table 18 has the same form and rationale of G2, but is used only for NO oxidation, since this reaction needs a different weight for NO inhibition effect respect to other ones.

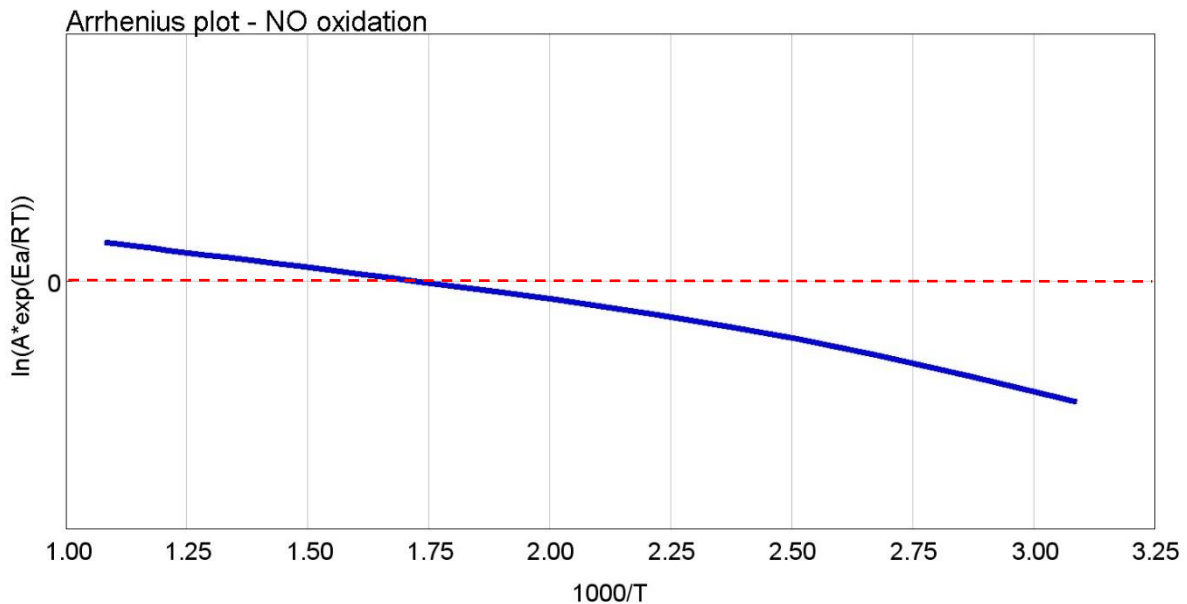


Figure 25 - Arrhenius plot for NO oxidation reaction, medium concentrations of NO in the inlet feeding gas.

3.3.1.3 WGS reaction

As mentioned in paragraph 2.1.2, the WGS, reaction number 6 of Table 18, occurs at temperature above 200 °C in presence of CO and H₂O, producing H₂ and CO₂. The correct modelling of WGS requests the definition of a set of inhibition functions, as illustrated in Table 18:

1. G1 and G2 are associated to the competition between CO and HCs on PGM sites;
2. G4 is representative of the equilibrium of the reaction;
3. G23 has the purpose to shape the WGS rate depending on the catalyst temperature.

The formula of G23 inhibition function is reported in equation 20, where “T” is the catalyst wall temperature.

$$20 \quad G23 = 1 + e^{-30} * e^{\frac{14000}{T}}$$

The equation 20 is composed by two terms:

1. The first unitary term ensures that the function does not reach the zero value;
2. The second term is a decreasing function of temperature.

The use of an inhibition function like G23 has the purpose to model the non-linear behavior of the WGS as function of temperature: from SGB tests it was observed a sudden increase of reaction rate at temperatures between 200°C and 225°C and the inhibition of WGS when LNT temperature is below 200°C. The resulting reaction rate on the Arrhenius plot is reported in Figure 26.

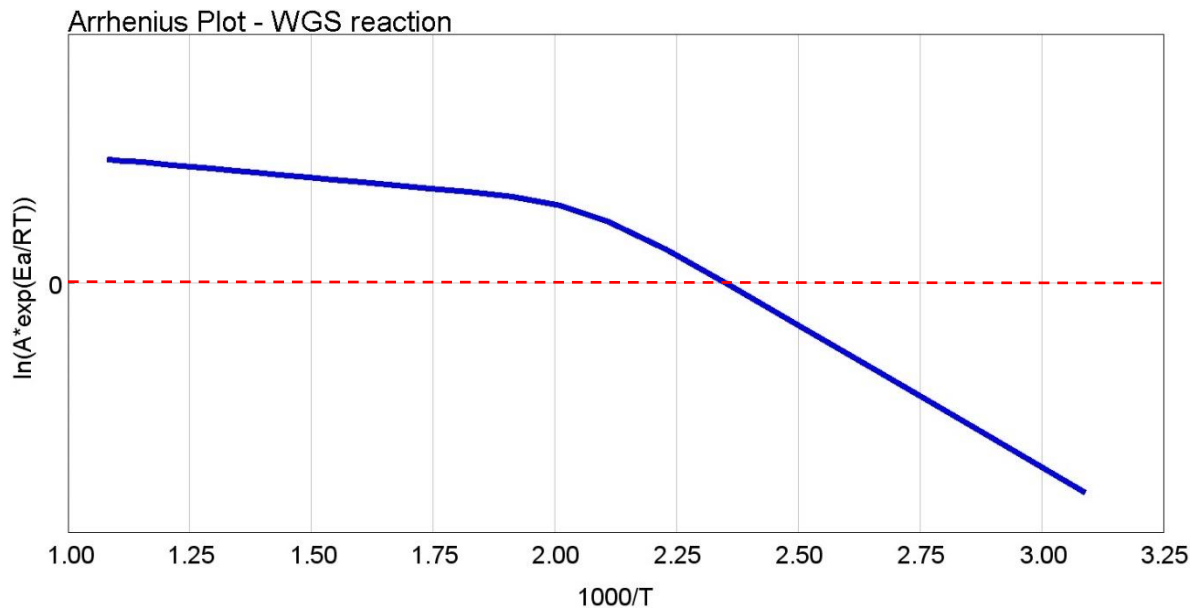


Figure 26 - Arrhenius plot for WGS reaction.

3.3.1.4 SR reaction

The SR, reaction number 7 in Table 18, occurs at high temperatures and in presence of H_2O . It consumes water and propylene, producing H_2 and CO . The consumption of CO by means of SR becomes significant above $300^\circ C$. SR is affected by the competition between CO and HCs on PGM sites. Therefore, the same inhibition functions defined for the LO, G1 and G2, are used to implement this effect.

Calibration of SR reaction was done based on outputs from OSC and NSR tests with C_3H_6 as reductant. The resulting Arrhenius from calibration is reported in Figure 27.

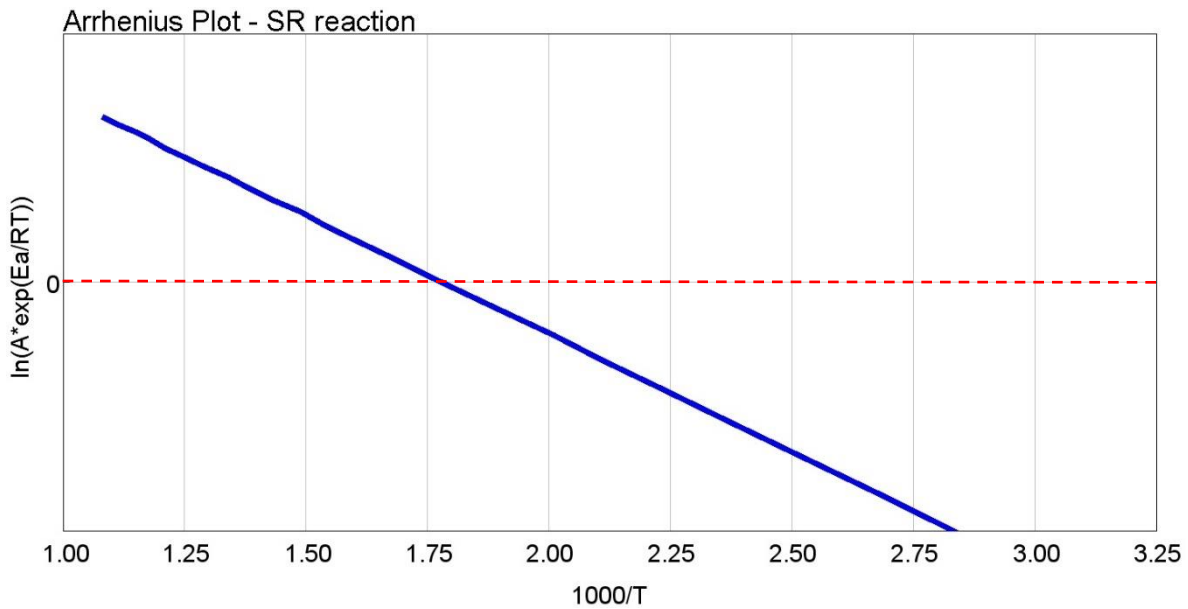


Figure 27 - Arrhenius plot for SR reaction.

The Activation Energy and the pre-exponent multiplier were calibrated in order to have a rate different from 0 when the LNT inlet temperature is above 300 °C.

3.3.2 Storage and oxidation reactions over Cerium sites

The OSC and the consumption of stored O₂ were modeled according to reactions from 10 to 13 reported in Table 19. Reaction 10, which represents the O₂ storage on cerium sites, was calibrated based on SGB results in lean conditions from OSC tests. Reactions from 11 to 13, which describe the oxidation of the reductants by means of stored O₂, were calibrated based on the outputs from OSC test during the rich event (see paragraph 2.1.2). Due to the unavailability of H₂ measurements, reaction 12 was not calibrated, and the default calibration presented in [7] was used.

	Reaction	Rate Expression
10	$Ce_2O_3 + 0.5O_2 \rightarrow 2CeO_2$	$r_{10} = k_{10} \frac{C_{O_2} \theta_{Ce_2O_3} G_7}{G_8}$
11	$2CeO_2 + CO \rightarrow Ce_2O_3 + CO_2$	$r_{11} = k_{11} \frac{C_{CO} \theta_{CeO_2} G_{15}}{G_{27}}$
12	$2CeO_2 + H_2 \rightarrow Ce_2O_3 + H_2O$	$r_{12} = k_{12} C_{H_2} \theta_{CeO_2} G_{16}$
13	$2CeO_2 + 0.111111C_3H_6 \rightarrow Ce_2O_3 + 0.333333CO_2 + 0.333333H_2O$	$r_{13} = k_{13} \frac{C_{C_3H_6} \theta_{CeO_2} G_{15}}{G_{27}}$

Table 19 - OSC associated reactions.

The calibration of oxidation reactions on cerium sites should consider the coexistence with other two phenomena typical of rich events: WGS and SR. Based on the reactor-scale experimental evidence, the WGS is active when temperature is above 200°C, while the SR is enabled above 300°C, as depicted in Figure 28. Moreover, from OSC tests the oxidation of CO and C₃H₆ by means of stored O₂ is already observed at temperatures below 200°C. Therefore, it is possible to decouple the calibration of reductants oxidation from WGS and SR.

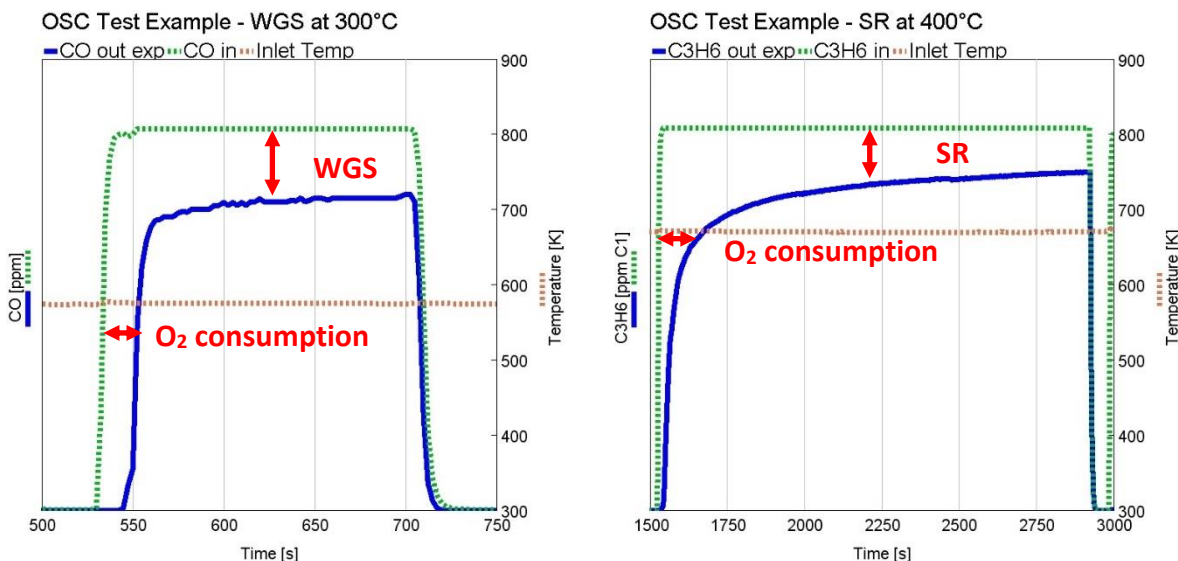


Figure 28 - Example of two OSC tests: with CO as reductant, performed at 300°C (573°K) (left) and with C₃H₆, performed at 400°C (right). The green line represents the CO inlet concentration, while the blue line the outlet one. The orange dotted line represents the temperature profile.

The calibration of CO and C₃H₆ oxidations involves also the definition of two additional inhibition functions: G15 and G27 (see Table 19). G15 modifies the rates of reaction 11 and 13 depending on ceria coverage value, smoothing the breakthrough curves [41].

The formula of inhibition function G27 is reported in equation 21:

$$21 \quad G27 = 1 + e^{\frac{2300}{T}} * \{O_2\}$$

The equation 21 is composed by two terms:

1. The first unitary term ensures that the function does not reach the zero value;
2. The second term is dependent on temperature and oxygen concentration. It assumes higher values with increasing O₂ concentrations, while it decreases with increasing temperature.

G27 (reactions 11 and 13) was implemented to limit the oxidation rate of CO and C₃H₆ due to OSC in case of lean atmosphere, because the direct reaction with the oxygen in the feeding gas is expected to prevail in these conditions. The effect of G27 on CO and C₃H₆ oxidation is depicted in Figure 29. The continuous lines (blue for C₃H₆, red for CO) are the oxidation rates in case of rich atmosphere (no O₂ in the feed gas), while the dashed line is referred to the rates in lean conditions (high concentrations of O₂).

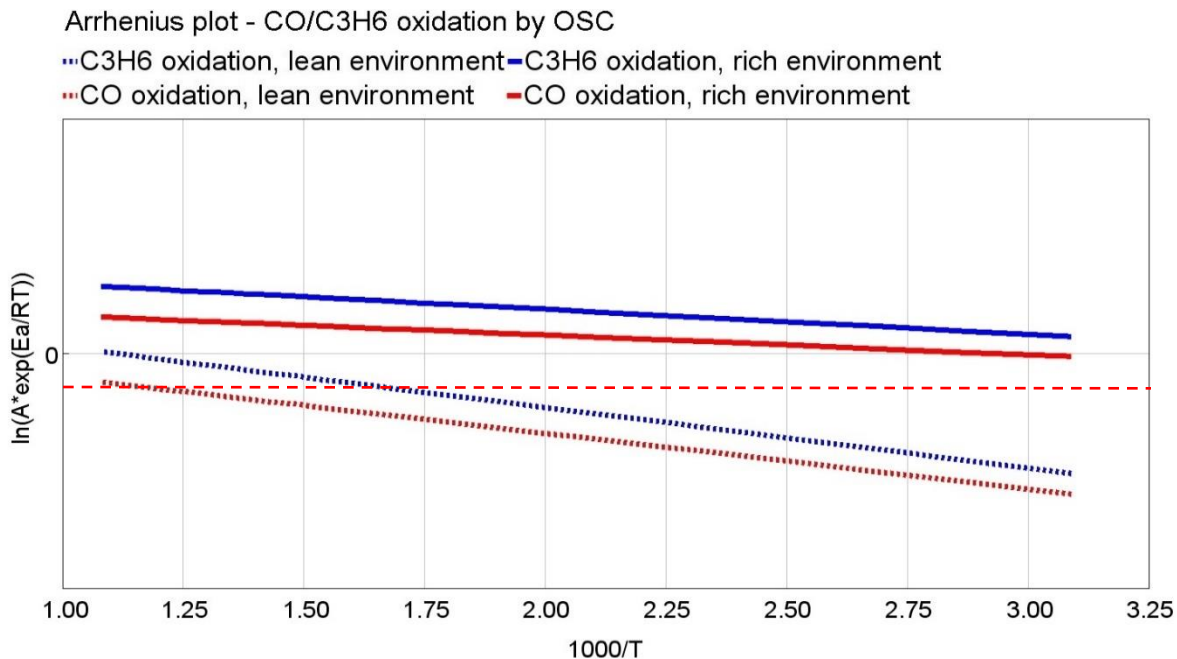


Figure 29 - Arrhenius plot for C₃H₆ (blue) and CO (red) oxidation through O₂ stored on the catalyst. The dotted lines represent the Arrhenius term in lean conditions (high percentages of O₂ in the atmosphere), while continuous lines represent the Arrhenius term in rich conditions (no O₂ in the atmosphere composition).

The calibration of the oxygen storage (reaction 10 of Table 19) was done acting on the density of ceria sites (mol/m³), to match the consumption of CO and C₃H₆. The related inhibition function G7 represents the chemical equilibrium as function of temperature.

3.3.3 NO_x storage on LT-LNT

The NO_x storage mechanism is reported in Table 20 and it was calibrated based on TPD tests.

	Reaction	Rate Expression
14	$Ba_1O + 2NO + 1.5O_2 \rightarrow Ba_1(NO_3)_2$	$r_{14} = k_{14} \frac{C_{NO} C_{O_2} \theta_{Ba_1O} G_{19}}{G_{20}}$
15	$Ba_1O + 3NO_2 \rightarrow Ba_1(NO_3)_2 + NO$	$r_{15} = k_{15} C_{NO_2} \theta_{Ba_1O}$

16	$Ba_{II}O + 2NO + 0.5O_2 \rightarrow Ba_{II}(NO_2)_2$	$r_{16} = k_{16} \frac{C_{NO} C_{O_2} \theta_{Ba_{II}O}}{G_{12}}$
17	$Ba_{III}O + 2NO_2 + 0.5O_2 \rightarrow Ba_{III}(NO_3)_2$	$r_{17} = k_{17} \frac{C_{NO_2} C_{O_2} \theta_{Ba_{III}O}}{G_6 G_{21}}$
18	$Ba_I(NO_3)_2 \rightarrow Ba_I O + 2NO + 1.5O_2$	$r_{18} = k_{18} \theta_{Ba_I O} G_{24}$
19	$Ba_{II}(NO_2)_2 \rightarrow Ba_{II}O + 2NO + 0.5O_2$	$r_{19} = k_{19} \frac{\theta_{Ba_{II}O}}{G_{12}}$
20	$Ba_{III}(NO_3)_2 \rightarrow Ba_{III}O + 2NO_2 + 0.5O_2$	$r_{20} = k_{20} \theta_{Ba_{III}O} G_{25}$

Table 20 - NO_x storage reactions.

The analysis of TPD tests (examples are reported in Figure 30 and Figure 31) highlighted that NO and NO₂ have different adsorption and desorption mechanisms, depending on temperature and NO/NO₂ ratio. In order to capture the experimental behavior, three barium active sites were considered, having the following main characteristics:

1. **NO adsorption mechanism** (reactions 14 and 16 from Table 20):
 - Barium-I: storage of NO as nitrates through oxygen spilled over from adjacent Pt sites;
 - Barium-II: NO storage through formation of nitrites at low temperature.
2. **NO desorption mechanism** (reactions 18 and 19 from Table 20):
 - The experimental tests highlighted the presence of two NO desorption peaks: the first located at temperatures below 200°C, the second in all the temperature regions. This peculiar condition requests the definition of two sites, which are characterized by different desorption temperature (Barium-I – all temperatures, Barium-II – low temperatures).
3. **NO₂ adsorption mechanism** (reactions 15 and 17 from Table 20):
 - Barium-I: storage of NO₂ through nitrates route, which happens when NO₂/NO ratio in the feeding gas is different from zero;
 - Barium-III: storage of NO₂ as nitrates through oxygen spilled over from adjacent Pt sites.
4. **NO₂ desorption mechanism** (reaction 20 from Table 20):
 - All the considered TPD tests show the presence of only one desorption peak. Therefore, only one site is needed, which is Barium-III.

The first calibration step of adsorption phase consisted into the definition of the Active Site Density (mol/m^3) of barium sites. This step was done applying the stoichiometry of adsorption reactions from the calculation of the moles of NO and NO₂ desorbed by the LNT during the temperature ramp at the end of TPD.

The second step involved the calibration of adsorption and desorption reactions. The analysis of TPD tests, illustrated in Figure 30 and Figure 31, highlights that:

1. At 100°C the LT LNT is capable to store a low amount of NO, while the NO₂ stored is negligible because the NO oxidation is still not active;
2. Within the temperature range between 100°C and 200°C, two NO desorption peaks are visible, while only one for NO₂;
3. At high temperatures (above 200°C), the first NO site is no longer available for adsorption, and only two sites, one for NO and one for NO₂, are capable to store NO_x. The storage capacity drops down for both sites for temperature higher than 400°C, leading to almost no adsorption/desorption at 450°C.

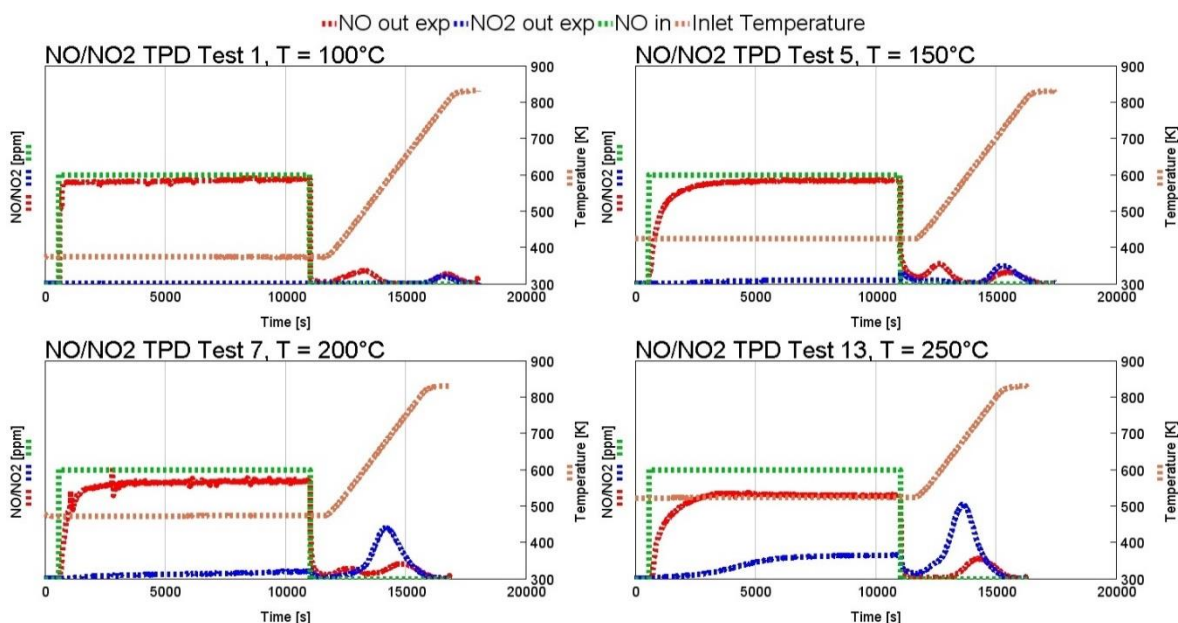


Figure 30 - NO and NO₂ experimental traces, Test 1: T=100°C, Test 5: T=150°C, Test 7: T=200°C, Test 13: T=250°C. Low SV conditions, NO medium concentration, NO₂/NO = 0. The green line represents the inlet NO concentration, while the red and blue ones represent respectively the NO and NO₂ outlet experimental traces. The orange line depicts the inlet temperature profile.

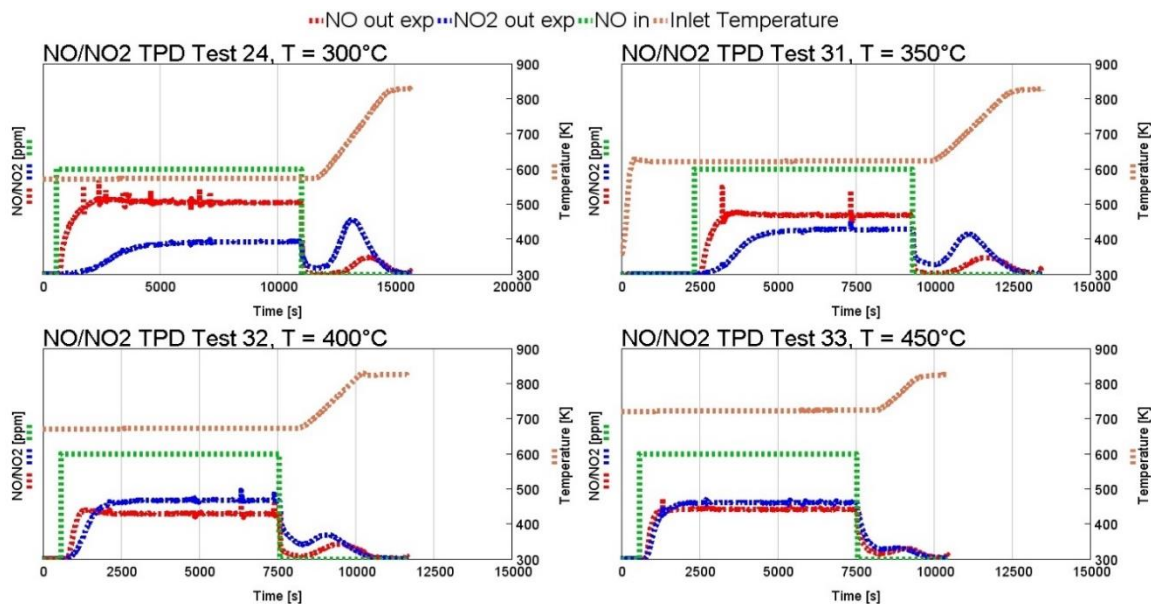


Figure 31 - NO and NO₂ experimental traces, Test 24: T=300°C, Test 31: T=350°C, Test 32: T=400°C, Test 33: T=450°C. Low SV conditions, NO medium concentration, NO₂/NO = 0. The green line represents the inlet NO concentration, while the red and blue ones represent respectively the NO and NO₂ outlet experimental traces. The orange line depicts the inlet temperature profile.

The results from the calibration process are depicted in Figure 32 and Figure 33. In Figure 32 the adsorption (blue line) and the desorption curve (red line) on Barium-II site, reactions 16 and 19 of Table 20, are illustrated on the Arrhenius plot. The shape of the adsorption curve (blue line in Figure 32) in the Arrhenius plot is caused by the inhibition function G12 [41], which disables the NO adsorption at temperatures below 125°C, in agreement with TPD tests. On the contrary, the desorption starts at 200°C and above this threshold the desorption rate is higher than the adsorption one.

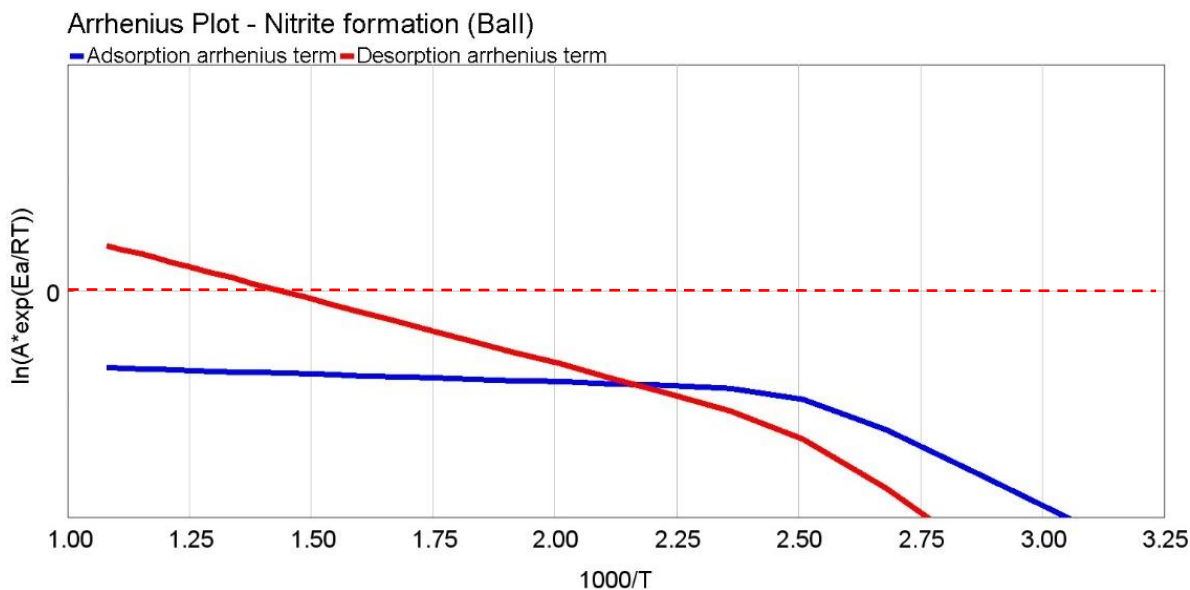


Figure 32 - Arrhenius terms of adsorption and desorption reactions associated to nitrite formation (Barium-II). The blue line represents the adsorption rate, while the red one the desorption rate.

Figure 33 shows the adsorption and desorption curves on the Arrhenius plot in case of the Barium-I site (reactions 14 and 18 of Table 20). The blue continuous line represents the adsorption curve when barium sites are empty (zero coverage), the blue dashed line is referred to the adsorption curve when barium sites are full (coverage equal to one), and finally the red line is referred to the desorption curve. The Barium-I is characterized by a larger temperature area than Barium-II, because the adsorption is still active above 300°C. At 400°C the desorption rate becomes higher than the adsorption one, leading to NO release.

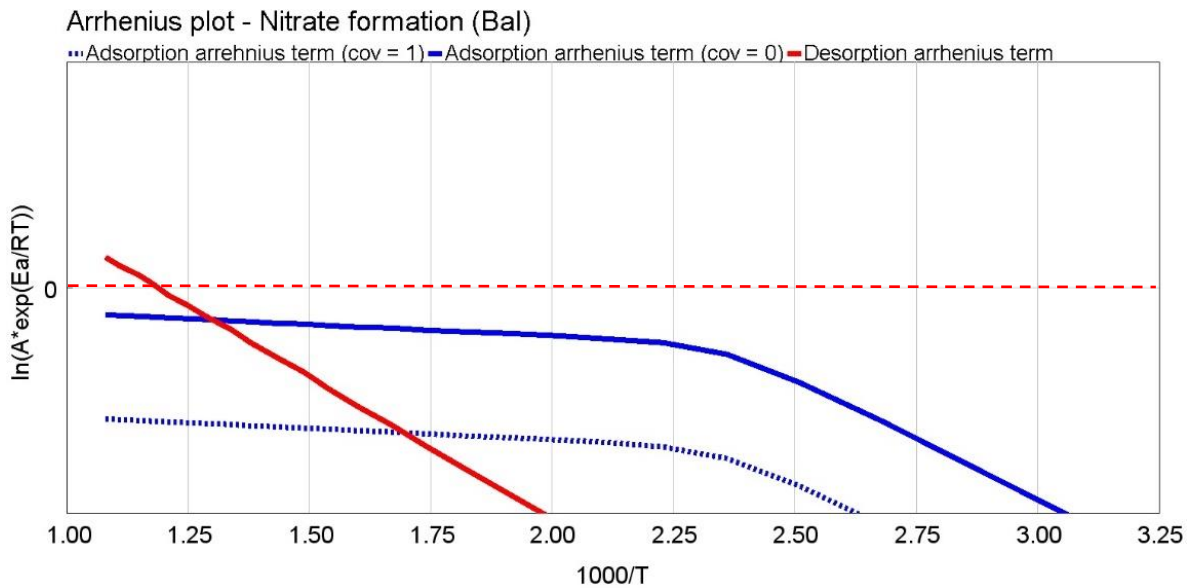


Figure 33 - Arrhenius terms of adsorption and desorption reactions associated to nitrate formation (Barium-I), the continuous blue line corresponds to adsorption rate with associated coverage equal to zero, while the dashed one corresponds to full site. The red line represents the desorption rate.

Thanks to G19 [41], a dependence from surface site coverage is added. The adsorption rate decrease with increasing coverage values for Barium-I site, thus the desorption occurs at lower temperatures than the calibrated 500°C for the empty site, in agreement with the experimental data.

The calibration process of adsorption and desorption on Barium-III site, which is related to NO_2 (reactions 17 and 20 of Table 20), is similar to Barium-I site, because from TPD test it shows good adsorption performance in a wide range of temperatures. However, in this case the use of a relationship with the surface site coverage was not requested. The Arrhenius plot obtained from the calibration is reported in Figure 34.

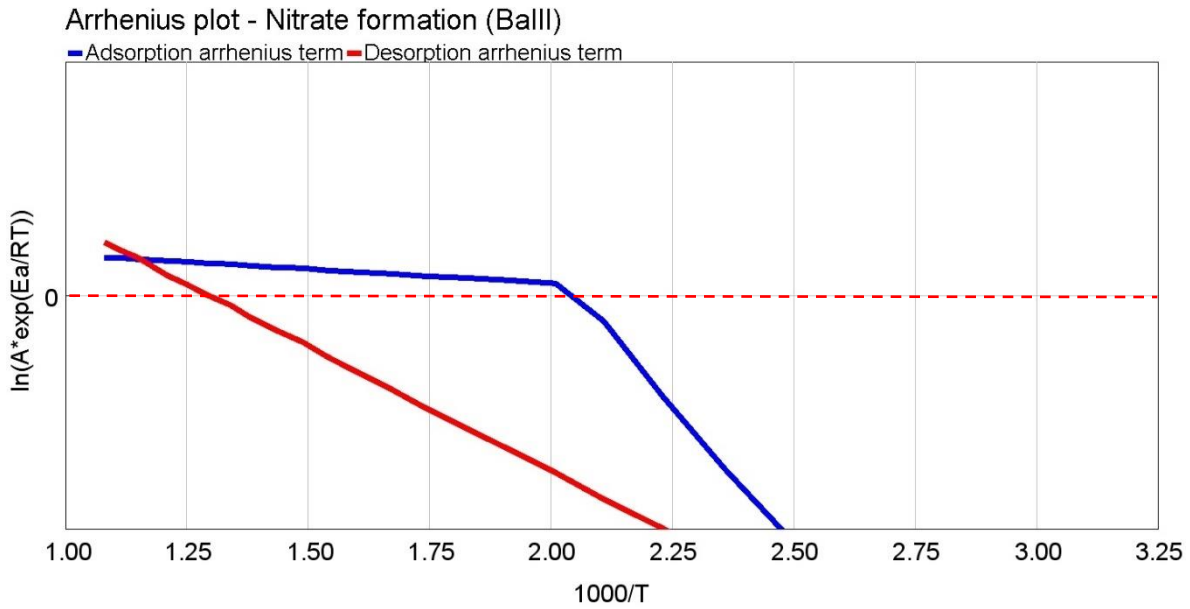


Figure 34 - Arrhenius terms of adsorption and desorption reactions associated to nitrate formation (Barium-III). The blue line represents the adsorption rate, while the red one the desorption rate.

Based on NSR data, it was observed an increase of desorption rates in presence of reducing atmosphere. Two inhibition functions, called G24 and G25, were added respectively to reaction 18 and 20 of Table 20. The formulas of these inhibition functions are visible in equations 22 and 23:

$$22 \quad G24 = 1 + e^{\frac{5000}{T}} * \{C_3H_6\} + e^{\frac{6800}{T}} * \{CO\} + e^{\frac{6000}{T}} * \{H_2\}$$

$$23 \quad G25 = 1 + e^{\frac{4000}{T}} * \{C_3H_6\} + e^{\frac{6800}{T}} * \{CO\} + e^{\frac{7000}{T}} * \{H_2\}$$

The equations 22 and 23 are composed by two terms:

1. The first unitary term ensure that the function does not reach the zero value;
2. The second term is dependent on temperature and reductant concentrations. It assumes higher values with increasing $C_3H_6/CO/H_2$ concentrations, while it decreases with increasing temperature.

The goal of these two inhibition functions is the boosting of desorption in presence of rich atmosphere. The decision to apply these inhibition functions only to Barium-I and Barium-III sites is based on the low stability of nitrites (Barium-II site) in the low temperature region. The NO desorption from Barium-I and Barium-III sites in is depicted in Figure 35, where the

continuous lines are representative of desorption in lean atmosphere, while the dashed ones illustrate the desorption in case of rich atmosphere with C₃H₆ as reductant.

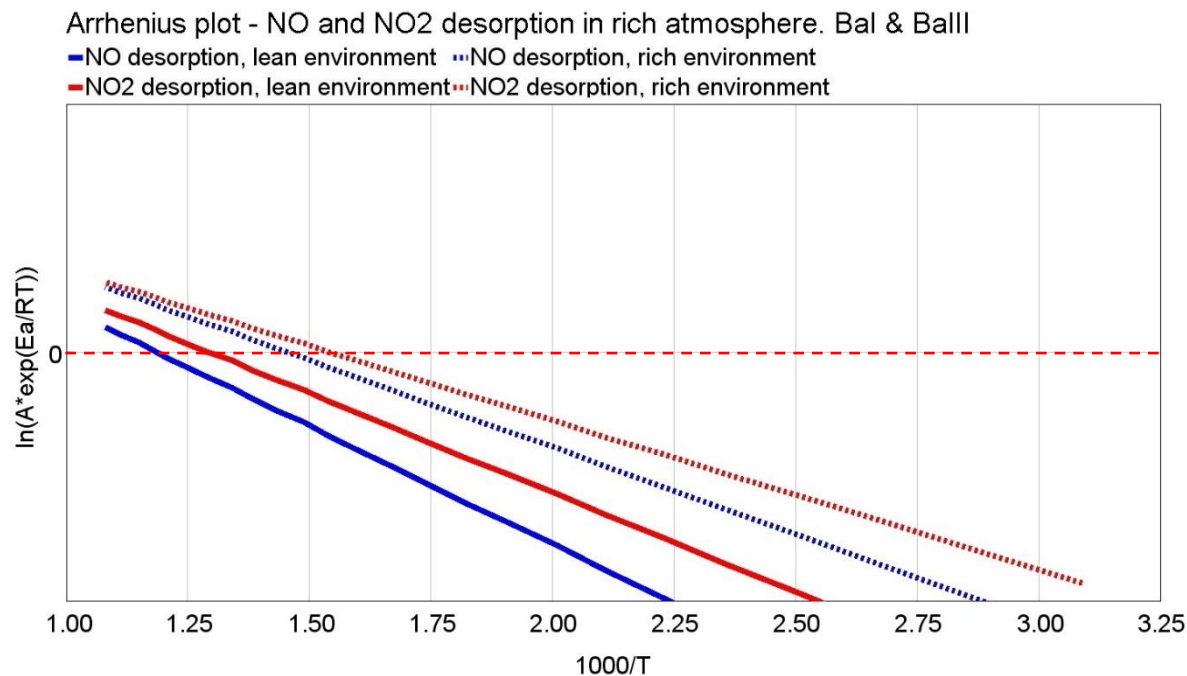


Figure 35 - Arrhenius terms for NO (blue) and NO₂ (red) desorption related to Barium-I and Barium-III sites in lean conditions (continuous lines) and in rich conditions, with high concentrations of C₃H₆ (dashed lines), where inhibition function G₂₄ increase the rate.

3.3.4 NO_x reduction

The chemical reactions representative of NO_x reduction on LT-LNT are reported in Table 21.

	Reaction	Rate Expression
21	$Ba_I(NO_3)_2 + 8H_2 \rightarrow Ba_I O + 2NH_3 + 5H_2O$	$r_{21} = k_{21} \frac{C_{H_2} \theta_{Ba_I(NO_3)_2}}{G_{17}}$
22	$Ba_{II}(NO_2)_2 + 6H_2 \rightarrow Ba_{II} O + 2NH_3 + 3H_2O$	$r_{22} = k_{22} \frac{C_{H_2} \theta_{Ba_{II}(NO_2)_2}}{G_{17}}$

23	$Ba_{III}(NO_3)_2 + 3H_2 \rightarrow Ba_{III}O + 2NO + 3H_2O$	$r_{23} = k_{23} \frac{C_{H_2} \theta_{Ba_{III}(NO_3)_2}}{G_{17}}$
24	$Ba_{III}(NO_3)_2 + 8H_2 \rightarrow Ba_{III}O + 2NH_3 + 5H_2O$	$r_{24} = k_{24} \frac{C_{H_2} \theta_{Ba_{III}(NO_3)_2}}{G_{17}}$
25	$Ba_I(NO_3)_2 + 3.333333NH_3 \rightarrow Ba_I O + 2.666667N_2 + 5H_2O$	$r_{25} = k_{25} \frac{C_{NH_3} \theta_{Ba_I(NO_3)_2}}{G_{17}}$
26	$Ba_{II}(NO_2)_2 + 2NH_3 \rightarrow Ba_{II}O + 2N_2 + 3H_2O$	$r_{26} = k_{26} \frac{C_{NH_3} \theta_{Ba_{II}(NO_2)_2}}{G_{17}}$
27	$Ba_{II}(NO_2)_2 + 0.4NH_3 \rightarrow Ba_{II}O + 2.4NO + 0.6H_2O$	$r_{27} = k_{27} \frac{C_{NH_3} \theta_{Ba_{II}(NO_2)_2}}{G_{17}}$
28	$Ba_{III}(NO_3)_2 + 3.333333NH_3 \rightarrow Ba_{III}O + 2.666667N_2 + 5H_2O$	$r_{28} = k_{28} \frac{C_{NH_3} \theta_{Ba_{III}(NO_3)_2}}{G_{17}}$
29	$Ba_I(NO_3)_2 + 2NH_3 \rightarrow Ba_I O + 2N_2O + 3H_2O$	$r_{29} = k_{29} \frac{C_{NH_3} \theta_{Ba_I(NO_3)_2}}{G_{17}}$
30	$Ba_I(NO_3)_2 + 5CO \rightarrow Ba_I O + 5CO_2 + N_2$	$r_{30} = k_{30} \frac{C_{CO} \theta_{Ba_I(NO_3)_2}}{G_{17}}$
31	$Ba_{II}(NO_2)_2 + CO \rightarrow Ba_{II}O + 2NO + CO_2$	$r_{31} = k_{31} \frac{C_{CO} \theta_{Ba_{II}(NO_2)_2}}{G_{17}}$
32	$Ba_{II}(NO_2)_2 + 3CO \rightarrow Ba_{II}O + N_2 + 3CO_2$	$r_{32} = k_{32} \frac{C_{CO} \theta_{Ba_{II}(NO_2)_2}}{G_{17}}$
33	$Ba_{III}(NO_3)_2 + 5CO \rightarrow Ba_{III}O + 5CO_2 + N_2$	$r_{33} = k_{33} \frac{C_{CO} \theta_{Ba_{III}(NO_3)_2}}{G_{17}}$
34	$Ba_I(NO_3)_2 + 4CO \rightarrow Ba_I O + 4CO_2 + N_2O$	$r_{34} = k_{34} \frac{C_{CO} \theta_{Ba_I(NO_3)_2}}{G_{17}}$
35	$Ba_I(NO_3)_2 + 0.555556C_3H_6$ $\rightarrow Ba_I O + 1.666667H_2O + 1.666667CO_2 + N_2$	$r_{35} = k_{35} \frac{C_{C_3H_6} \theta_{Ba_I(NO_3)_2}}{G_{17}}$
36	$Ba_I(NO_3)_2 + 0.333333C_3H_6 \rightarrow Ba_I O + H_2O + CO_2 + 2NO$	$r_{36} = k_{36} \frac{C_{C_3H_6} \theta_{Ba_I(NO_3)_2}}{G_{17}}$
37	$Ba_{II}(NO_2)_2 + 0.111111C_3H_6$ $\rightarrow Ba_{II}O + 0.333333H_2O + 0.333333CO_2 + 2NO$	$r_{37} = k_{37} \frac{C_{C_3H_6} \theta_{Ba_{II}(NO_2)_2}}{G_{17}}$
38	$Ba_{III}(NO_3)_2 + 0.555556C_3H_6$ $\rightarrow Ba_{III}O + 1.666667H_2O + 1.666667CO_2 + N_2$	$r_{38} = k_{38} \frac{C_{C_3H_6} \theta_{Ba_{III}(NO_3)_2}}{G_{17}}$

39	$Ba_{III}(NO_3)_2 + 0.333333C_3H_6 \rightarrow Ba_{III}O + H_2O + CO_2 + 2NO$	$r_{39} = k_{39} \frac{C_{C_3H_6} \theta_{Ba_{III}(NO_3)_2}}{G_{17}}$
40	$C_3H_6 + 9NO \rightarrow 3H_2O + 3CO_2 + 4.5N_2$	$r_{40} = k_{40} \frac{C_{C_3H_6} C_{NO}}{G_1 G_2 G_{17}}$
41	$C_3H_6 + 18NO \rightarrow 3H_2O + 3CO_2 + 9N_2O$	$r_{41} = k_{41} \frac{C_{C_3H_6} C_{NO}}{G_1 G_2 G_{17}}$

Table 21 - NO_x reduction reactions.

Reactions from 21 to 28 in Table 21 describe the two steps DeNO_x behavior with H₂ as reductant [28,29,30,31]. This mechanism describes the reduction of NO_x with H₂ and the resulting formation of NH₃, which is used as NO_x reductant (SCR mechanism).

Reaction 29 models the N₂O production caused by NO_x reduction with ammonia.

Reactions from 30 to 33 represent the reduction of barium sites by means of CO, leading to N₂ production or the NO release. Reaction 34 takes into account N₂O production due to reduction through CO. Reactions from 35 to 39 are representative of DeNO_x on barium sites by means of C₃H₆ as reductant. Finally, reactions 40 and 41 are representative of NO_x reduction in the gaseous atmosphere, which lead to the production of N₂ and N₂O.

The calibration of DeNO_x is complex, because in rich conditions different phenomena occur, like the WGS and SR, which produce H₂. For example, when CO is used as reductant and the temperature is above 200°C, the WGS is enabled and H₂ production starts. Therefore, also due to the unavailability of H₂ measurements, it is difficult in calibration to discern between the two reduction mechanisms. The same issue is evident also in case of C₃H₆, because when the temperature is above 350°C the SR is active and H₂ production starts. This problem is particularly stressed in case of Barium-I and Barium-III sites that are active in storage in the same temperature region of WGS and SR. The calibration of reduction reactions is less stressed in case of Barium-II site, because the NO_x storage capacity is limited in the range of temperatures where WGS and SR are not active. However, in this latter case, the site is already quite inactive at temperatures above 200°C. Thus, considering that NSR tests start from 200°C, the reduction calibration of Barium-II site is not possible.

Another important aspect for the correct modelling of the LT-LNT is the characterization of the selectivity during the NSR test. From these tests, for both CO and C₃H₆, it was observed that at low temperatures the system is oriented to the NO production trough partial reduction, as depicted in Figure 36 (a) for C₃H₆ and Figure 37 (a) for CO, while at high temperatures it is observed high selectivity to the production of N₂. No Nitrogen measurement is available in this study, thus the higher selectivity to N₂ production was evaluated through the lower

NO emissions, that should mean complete reduction, as depicted in Figure 36 (b) for C_3H_6 and Figure 37 (b) for CO.

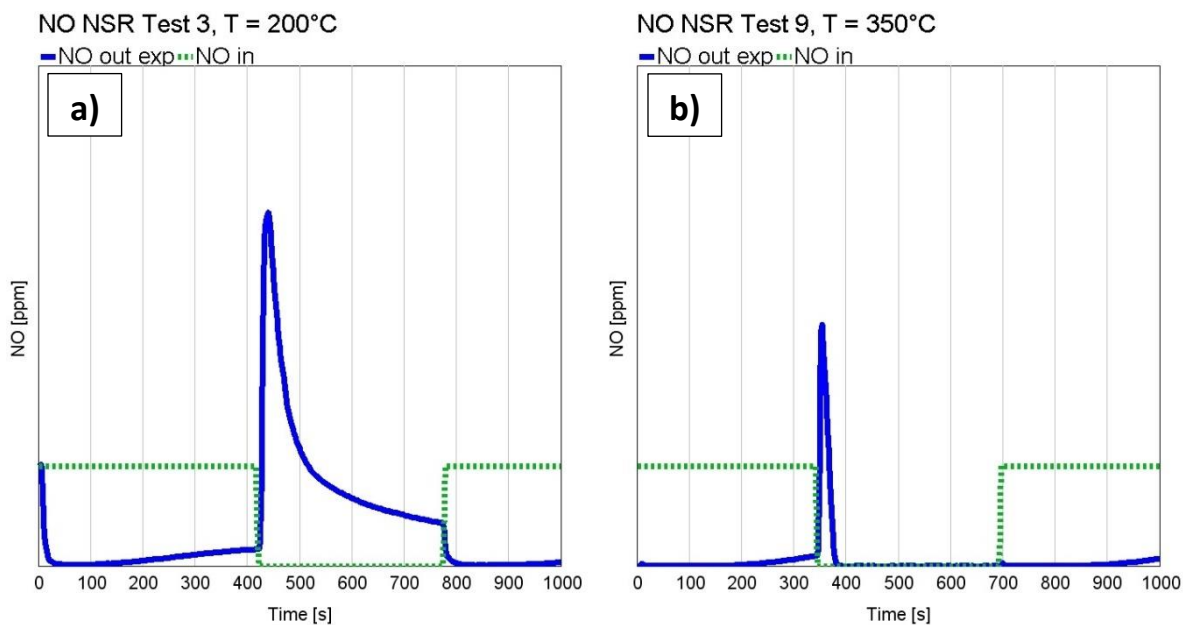


Figure 36 - NSR Test 3 (a), at $T=200^{\circ}C$, and Test 9 (b), at $T=350^{\circ}C$, C_3H_6 as reductant (see Table 14). The blue continuous lines represent the NO outlet concentration traces, while the green dashed ones the inlet NO concentration profiles.

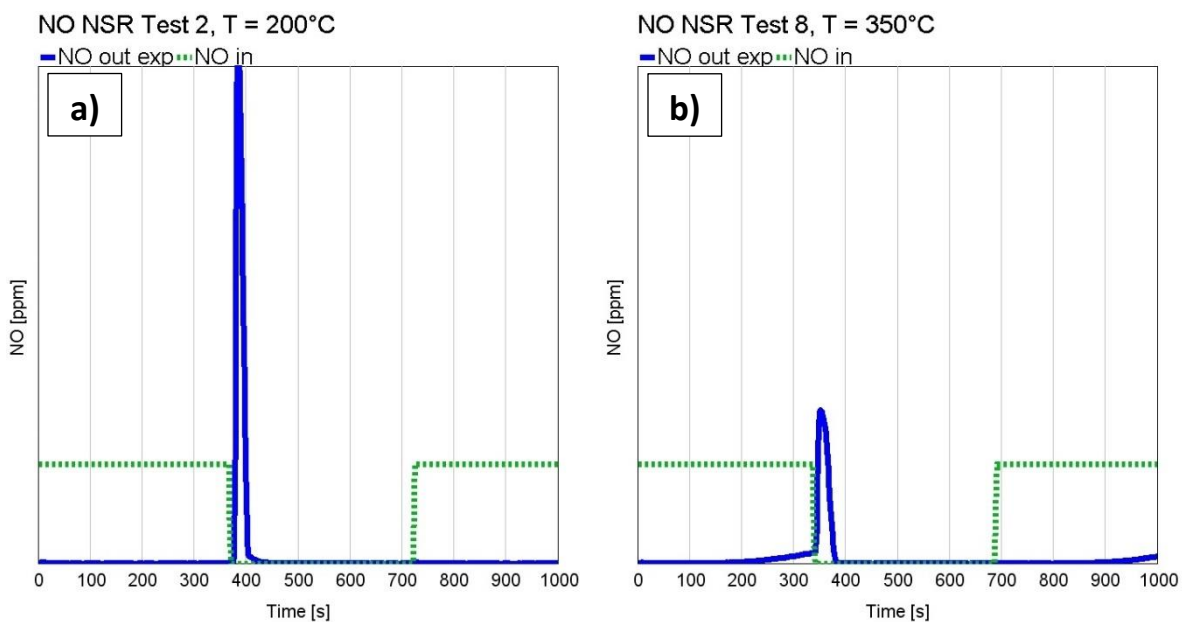


Figure 37 - NSR Test 2 (a), at $T=200^{\circ}C$, and Test 8 (b), at $T=350^{\circ}C$, CO as reductant (see Table 14). The blue continuous lines represent the NO outlet concentration traces, while the green dashed ones the inlet NO concentration profiles.

However, not all the reduction reactions associated with the barium sites were calibrated following the selectivity law previously described. To comply with this kind of calibration every barium site needs at least two reduction reactions for every kind of reductant (for CO and C₃H₆):

- One reaction for the partial reduction, with NO release in the gas flow. The logarithm of rate on the Arrhenius plot should be an almost flat line with positive values in the low temperatures region, having very little increase with rising temperatures;
- One reaction for the complete reduction of stored species, with the consequent N₂ evolution. The logarithm of rate on the Arrhenius plot should be a ramped line, with negative (or very low values) in the low temperatures region, while having higher values with increasing temperatures.

In this work, not all barium sites have all the reaction requested, because increasing the number of reactions implemented causes an undesired stiffness in the simulation activity. Furthermore, in some cases, to agree with experimental results, a different calibration is needed.

The resulting Arrhenius are reported in Figure 38 and Figure 39. As depicted from Figure 38, in case of reduction through C₃H₆ the selectivity previously described does not agree with the calibration found in this work. Conversely, the Arrhenius plots of reduction reactions 31 and 32 shown in Figure 39 give a good example of the selectivity previously mentioned. However, for sake of simplicity, Barium-I and Barium-II sites consider only the complete reduction reaction with N₂ evolution.

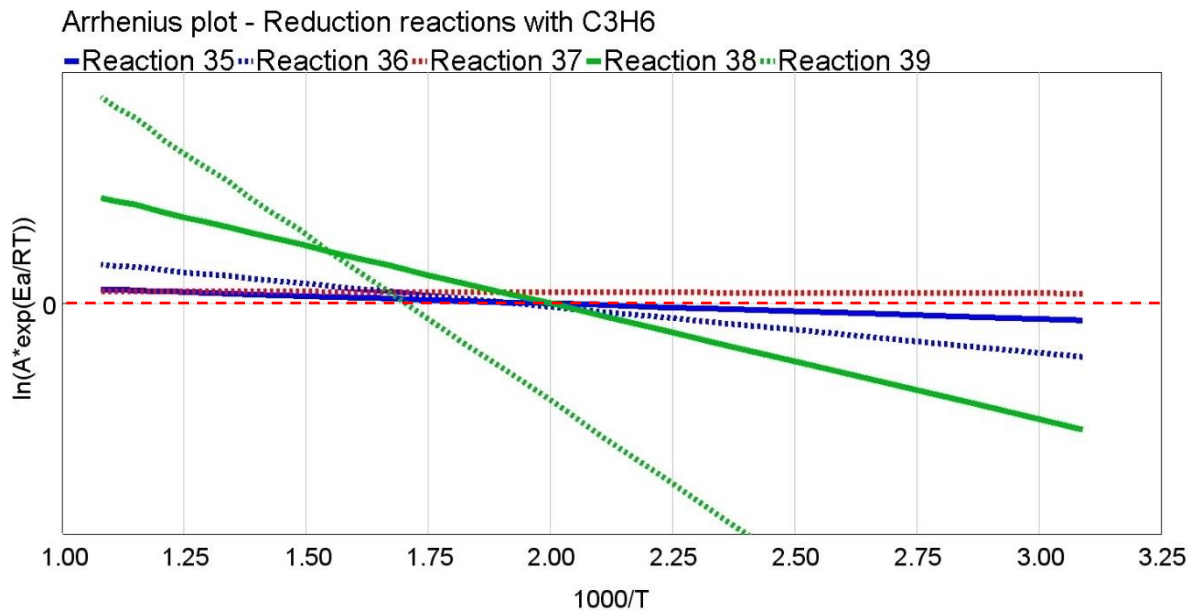


Figure 38 - Arrhenius plot for reduction reactions 35/36 (blue lines, related to Barium-I site), 37 (red line, related to Barium-II site) and 38/39 (green lines, related to Barium-III site), with C₃H₆ as reductant (see Table 21). The continuous lines refer to rate of reactions that lead to complete reduction of barium site with N₂ release, while the dashed ones represent the rate of partial nitrate/nitrite reduction with NO release.

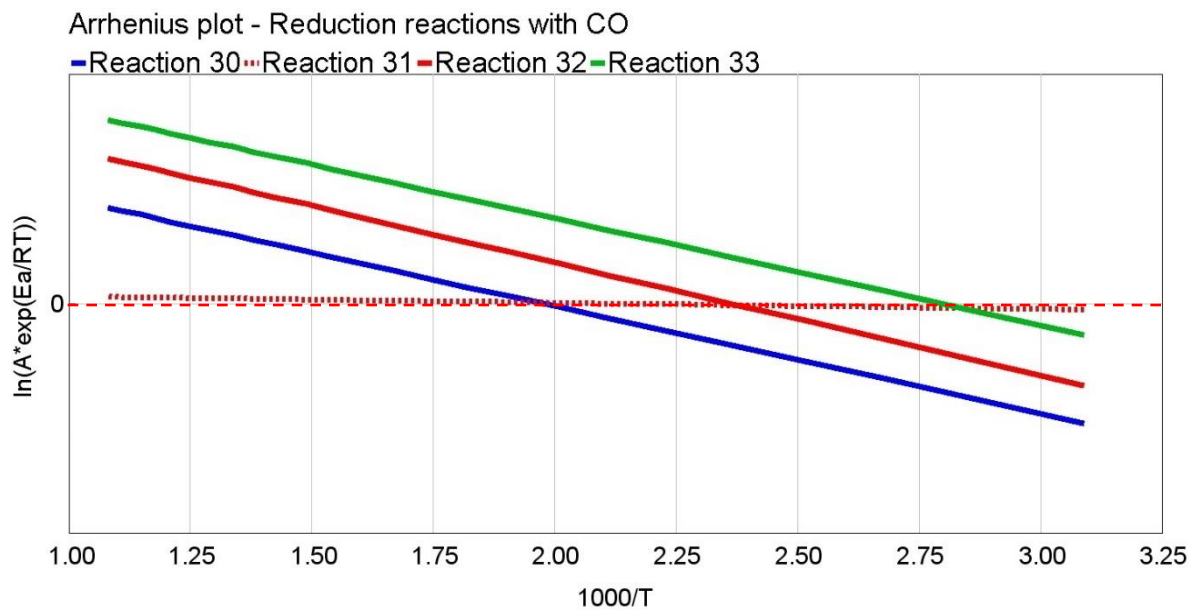


Figure 39 - Arrhenius plot for reduction reactions 30 (blue line, related to Barium-I site), 31/32 (red lines, related to Barium-II site) and 33 (green line, related to Barium-III site), with CO as reductant (see Table 21). The continuous lines refer to rate of reactions that lead to complete reduction of barium site with N₂ release, while the dashed ones represent the rate of partial nitrate/nitrite reduction with NO release.

Figure 40 show the NO out emission in case of NSR experiments performed with H₂.

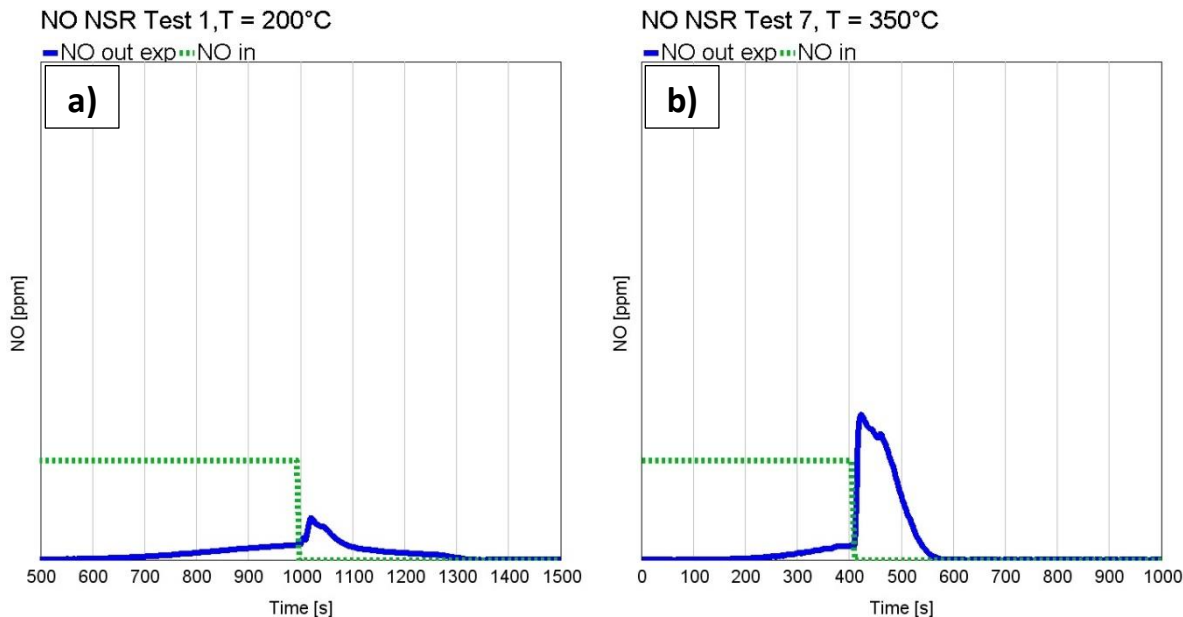


Figure 40 - NSR Test 1 (a), at $T=200^{\circ}\text{C}$, and Test 7 (b), at $T=350^{\circ}\text{C}$, H_2 as reductant (see Table 14). The blue continuous lines represent the NO experimental outlet concentration traces, while the green dashed ones the inlet NO experimental concentration profiles.

In this case, differently from NSR tests performed with C_3H_6 and CO , the NO out emissions increase with rising temperatures. However, it does not mean that the selectivity to N_2 reduces, but this is caused by the different reducing potential of H_2 . In fact, the reducing power is already high starting from low temperature and does not change to much increasing it. On the contrary, the NO free thermal release is boosted by the higher temperatures, leading to increased NO emissions. In case of propylene and CO , the reducing power increases more than the NO free thermal release in the 200°C - 350°C temperature range, leading to lower NO emissions with rising temperature.

Since no H_2 measurement is available, a different calibration procedure was used. When H_2 is involved in reduction process, the products are NO and NH_3 . The NH_3 produced contributes to the complete reduction of nitrates/nitrites with N_2 evolution (SCR mechanism) or to the partial reduction of adsorbed species through release of NO. As for CO and C_3H_6 , in the low temperature region the nitrates/nitrites are partially reduced with NO release, while at high temperatures the reaction between NH_3 and stored species produces N_2 . Based on outlet NO measures, it is possible to detect correctly the phenomena and calibrate properly the Arrhenius laws. The resulting Arrhenius plot are shown in Figure 41 and Figure 42. In Figure 41 is shown the calibration of the first step of reduction through H_2 , with ammonia production. The Figure 42 illustrates the Arrhenius plots for the second step of reduction with H_2 , where the NH_3 reacts with barium stored species. If Arrhenius plots related to reaction 26 and 27 (associated to Barium-II site, red lines in Figure 42) well correlate with the

previously mentioned selectivity law, Arrhenius plots referred to reactions associate to other sites don't.

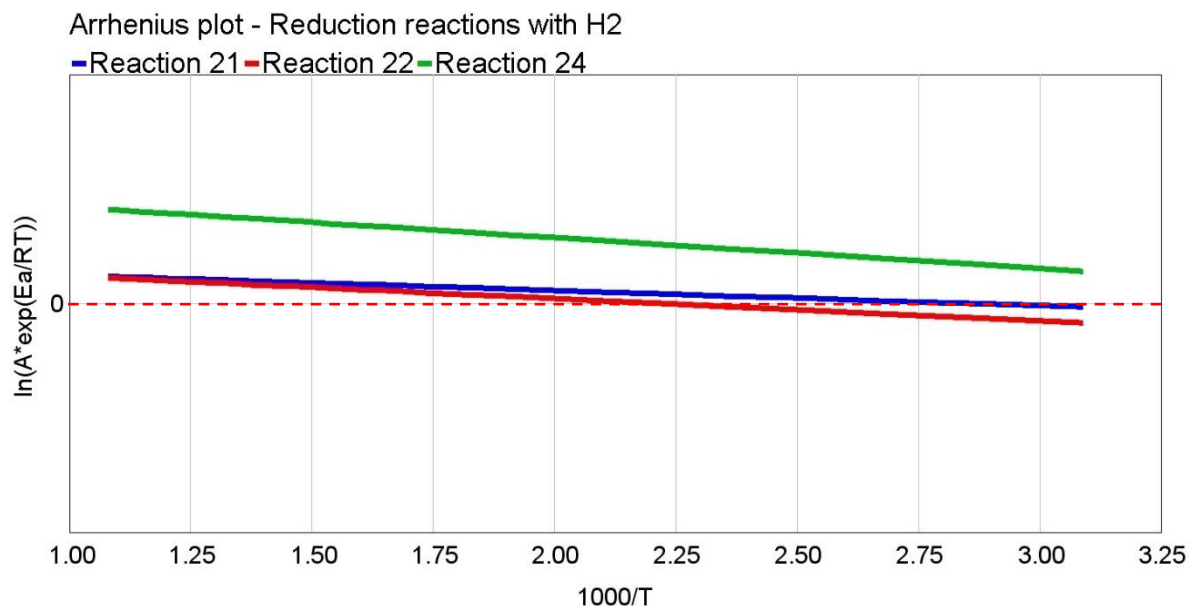


Figure 41 - Arrhenius plot for reduction reactions 21 (blue line, related to Barium-I site), 22 (red line, related to Barium-II site) and 24 (green line, related to Barium-III site), with H₂ as reductant (see Table 21).

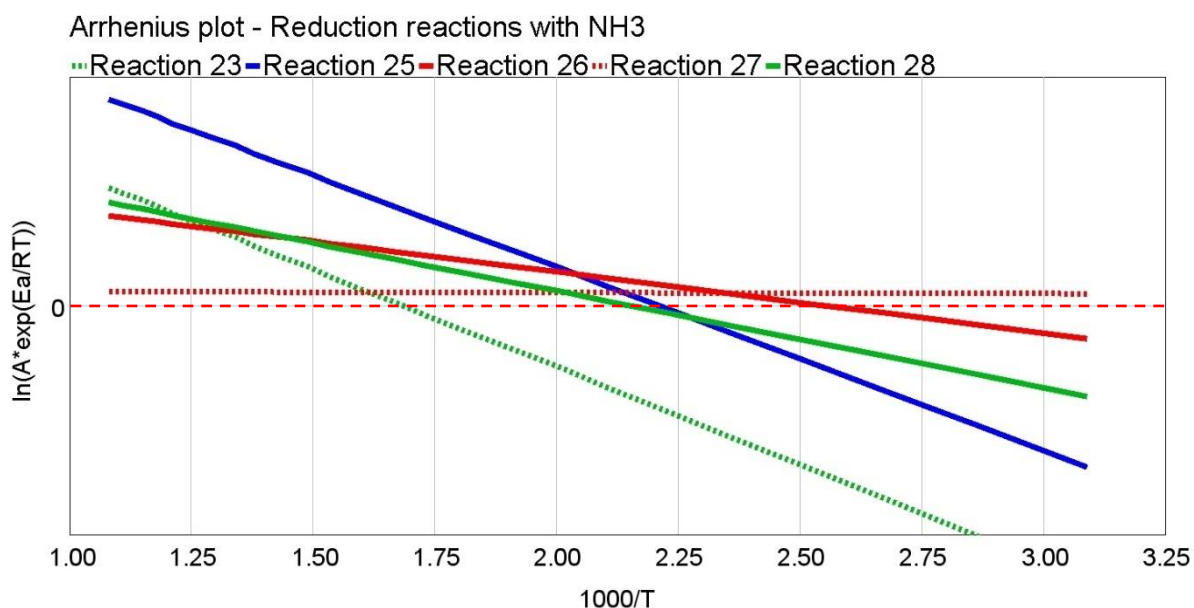


Figure 42 - Arrhenius plot for reduction reactions 25 (blue line, related to Barium-I site), 26/27 (red lines, related to Barium-II site) and 23/28 (green lines, related to Barium-III site), with CO as reductant (see Table 21). The continuous lines refer to rate of reactions that lead to complete reduction of barium site with N₂ release, while the dashed ones represent the rate of partial nitrate/nitrite reduction with NO release.

To strengthen the calibration of NO_x reduction, an inhibition function called G17 was added to all the reactions reported in Table 21. The formula of G17 is visible in equation 24:

$$24 \quad G17 = 1 + e^{-23.382} * e^{\frac{13970}{T}} * \{O_2\}$$

The equation 24 is composed by two terms:

1. The first unitary term ensures that the function does not reach the zero value;
2. The second term is dependent on temperature and oxygen concentration. It assumes higher values with increasing O₂ concentrations, while it decreases with increasing temperature.

This inhibition function prevents the enabling of NO_x reduction in lean atmosphere. An example of the effect of G17 applied to reaction 33 of Table 21 is reported in Figure 43 where the blue continuous curve is representative of the response in rich atmosphere, while the blue dashed one is representative of the lean condition.

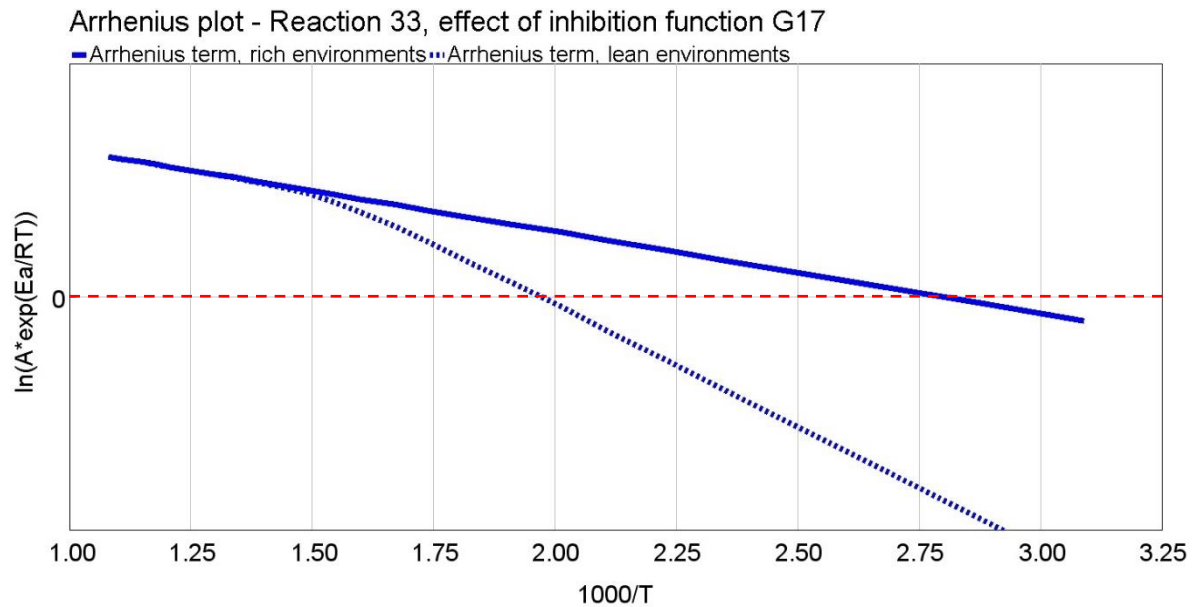


Figure 43 - Effect of inhibition function G17 on reduction reaction 33 of Table 21, in lean atmosphere with high percentages of oxygen. The blue dashed line represents the reduction reaction rate in lean conditions, while the continuous one is the rate profile in rich environments.

Figure 44 shows as example the N₂O out emission during NSR tests performed with H₂. In general, N₂O emissions should decrease with increasing temperatures, because the selectivity to N₂ production rises.

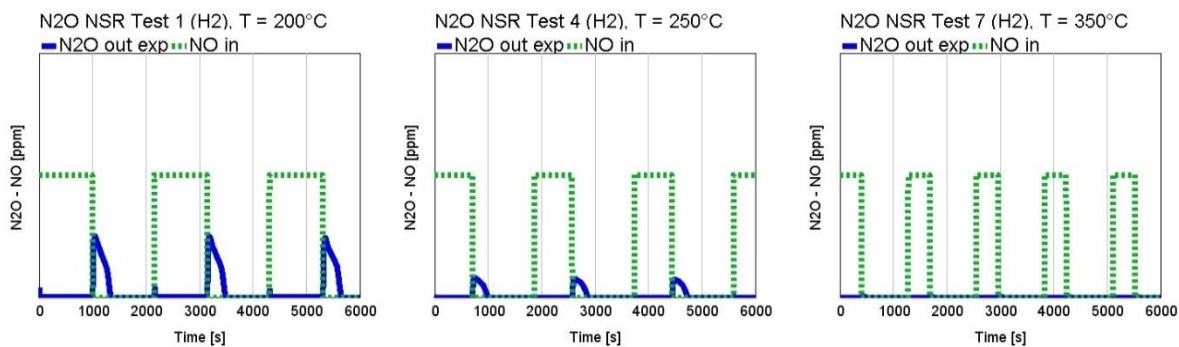


Figure 44 - N₂O out traces from NSR tests of Table 13: Test 1 at T=200°C (Left), Test 4 at T=250°C (Center), Test 7 at T=350°C (Right). The blue lines represent the experimental outlet N₂O and the dashed green lines the inlet NO concentrations.

Figure 45 show the Arrhenius plots for reduction reactions that leads to N₂O production. Reaction 29 and 34 (from Table 21) are related to Barium-I site, and account for reduction through NH₃ and CO respectively, while reaction 41 refers to reduction of gaseous NO through C₃H₆.

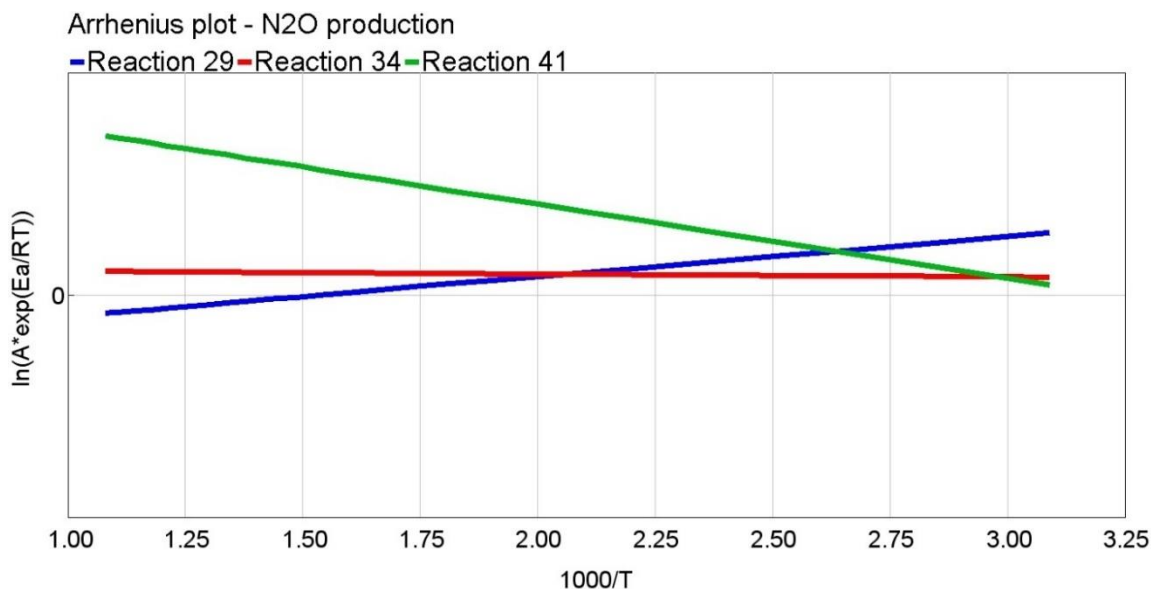


Figure 45 - Arrhenius plot for reduction reactions 29 (blue line, related to Barium-I site) with NH₃ as reductant, 34 (red line, related to Barium-I site) with CO as reductant and 41 (green line) with C₃H₆ as reductant (see Table 21).

4 Model assessment

This chapter presents the assessment of the LT-LNT model based on experimental data from SGB tests at reactor scale level and from chassis dyno tests at full scale level.

Due to the large number of experimental tests both in steady state and transient conditions, only the main results will be presented for sake of brevity.

4.1 Model assessment on SGB tests (reactor scale component)

The model validation at reactor scale level will focus on:

1. **Thermal model:** correlation between experimental and simulated results in terms of outlet temperature;
2. **Chemical model:** the validation will focus on the main driving characteristics of the LNT component: LO, OSC and NO_x reduction.

4.1.1 Thermal model

Usually, in SGB tests the heat loss is expected to be small due to the presence of an insulation layer. This is verified in the majority of the tests (few examples are reported in Figure 46).

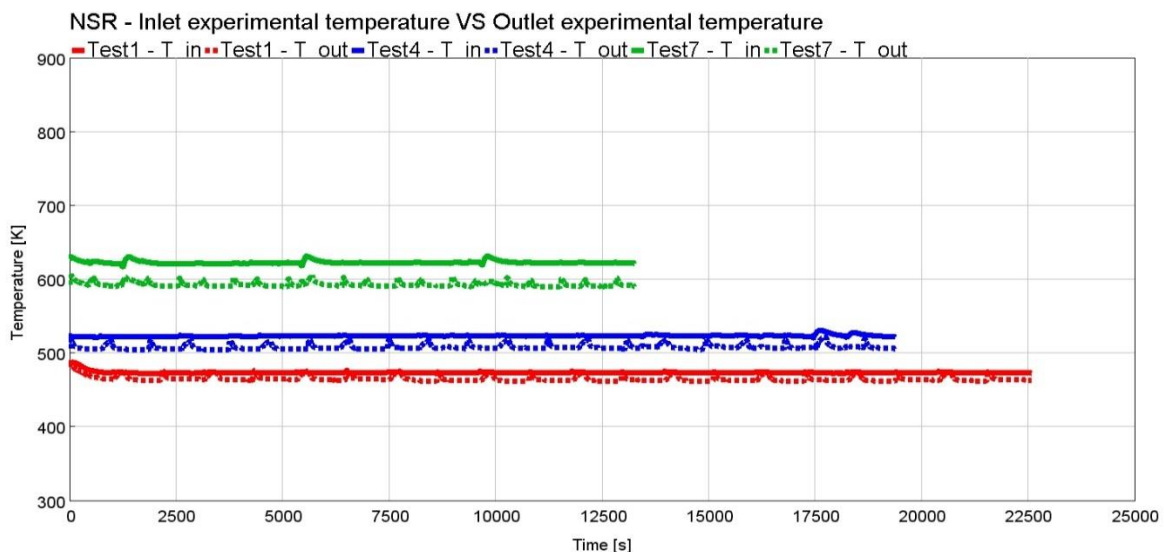


Figure 46 - NSR Test 1 (red), at $T=200^{\circ}\text{C}$, Test 4 (blue), at $T=250^{\circ}\text{C}$, Test 7 (green), at $T=350^{\circ}\text{C}$, H_2 as reductant (see Table 14). Continuous lines represent the inlet experimental temperatures, while dashed ones represent outlet experimental temperatures.

However, NO_x TPD experimental data shown a large discrepancy between inlet and outlet temperature, as depicted in Figure 47. Since in literature no endothermic phenomena were reported in case of adsorption reactions, the temperature difference was attributed to thermal losses. However, it is not excluded that other causes may generate this difference, such as the position of temperature sensor at the sample outlet.

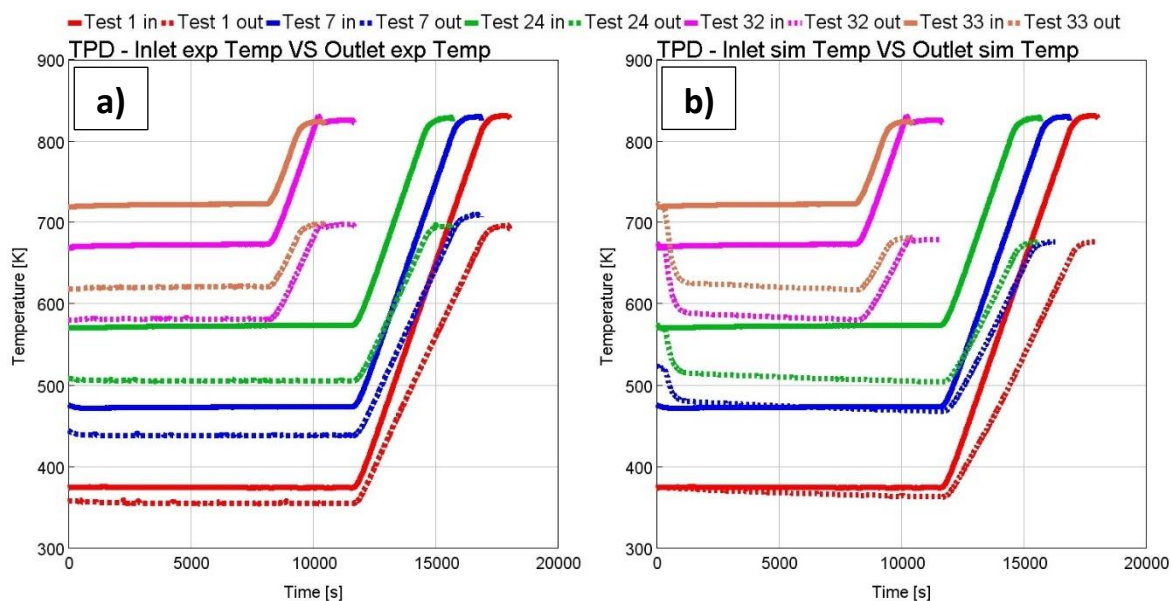


Figure 47 - Example of differences between inlet (continuous lines) and outlet (dashed lines) temperatures for TPD tests. Comparison between experimental temperature traces (left) and between simulated temperature traces (right). All the traces showed refers to TPDs with only medium NO concentrations in lean environment as inlet feeding species (see Table 13).

As showed by Figure 47 b), the implementation of thermal losses from the catalyst sample did not allow to correctly match the thermal behavior at the beginning of the experiments.

4.1.2 LO assessment

The assessment of the LO process was carried out considering two different levels of space velocity (SV): low and high. All the LO simulations were done applying the same boundary condition of the SGB tests (temperature, inlet species concentrations).

Figure 48 shows the LO results for tests 1, 3 and 6 (see Table 11) in case of low SV. The model is capable to predict with good accuracy the self-inhibition effect in low SV conditions, giving good predictions for all CO and NMHC inlet concentrations.

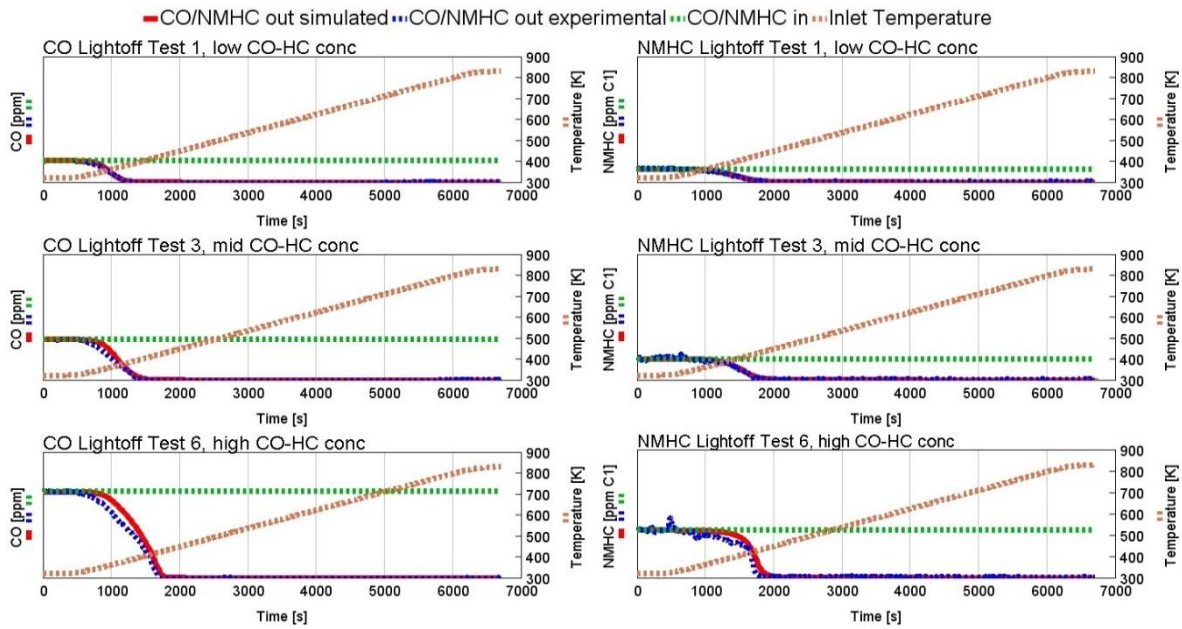


Figure 48 - CO and NMHC traces for Tests 1 - 3 - 6, performed at low Space Velocity. Boundary conditions are depicted in Table 11. The red lines refer to the simulated CO (left) and NMHC (right) outlet emissions, the blue lines to the experimental outlet ones, the green dashed to the inlet emissions and the light orange dashed lines to the inlet temperature profiles.

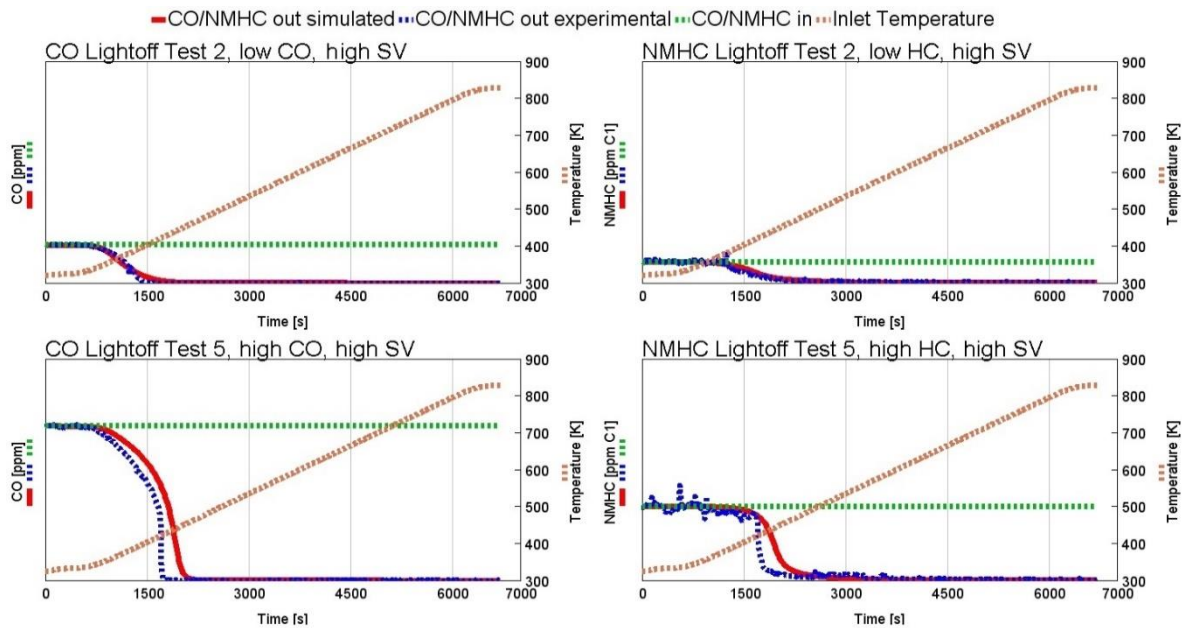


Figure 49 - CO and NMHC traces for Tests 2 - 5, performed at high Space Velocity. Boundary conditions are depicted in Table 11. The red lines refer to the simulated CO (left) and NMHC (right) outlet emissions, the blue lines to the experimental outlet ones, the green dashed to the inlet emissions and the light orange dashed lines to the inlet temperature profiles.

As described in Table 11, different tests were performed with the aim of characterizing the competition between CO, HCs and NO over PGM sites.

As highlighted in Figure 50 the model is capable to predict NO inhibition with satisfactory accuracy for the three different levels of this reductant in the inlet feeding gas (test 9, 12 and 14 of Table 11).

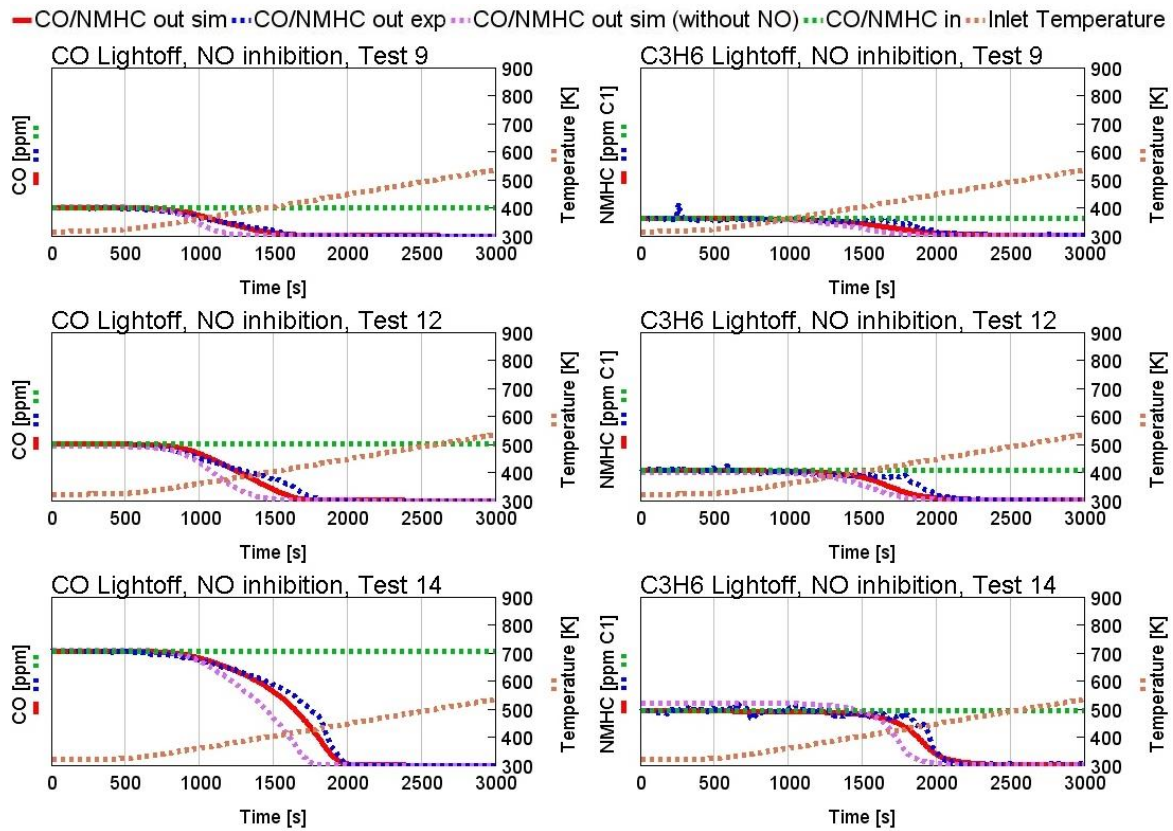


Figure 50 - Test 9 - 12 - 14, NO in the feeding gas, low SV. CO/NMHC simulated traces from tests with same conditions but without NO in the feeding gas have been reported for comparison (pink dashed lines). Boundary conditions are depicted in Table 11. The red lines refer to the simulated outlet emissions, the blue lines to the experimental outlet ones, the green dashed to the inlet emissions and the orange dashed lines to the inlet temperature profiles.

4.1.3 OSC assessment

Due to the lack of experimental data, the model assessment was based on average values calculated according to the methodology based on reaction stoichiometry described in paragraph 2.1.2. The characteristics of OSC tests shown in this chapter are collected in Table 12.

Figure 52 shows the results of OSC for tests 4,10 and 12 in case of CO as reductant, while Figure 51 for tests 5, 11 and 13 with C₃H₆. Both figures highlight that the model overestimates the OSC capacity. This lack of accuracy is caused by:

1. Inaccuracies from the experimental tests: the sampling frequency chosen is 0.5 Hz, which is a reasonable value for chemical reactions with a long-time scale. However, the consumption of O₂ during rich pulses is shorter than the sampling frequency, thus leading to an aliasing error;
2. Methodology used to estimate the OSC, which is based on reaction stoichiometry (see paragraph 2.1.2);
3. Impossibility to discern between reductant oxidation by mean of O₂ consumption, WGS effect (CO consumption) and SR effect (C₃H₆ consumption) in some conditions, during the rich pulses.

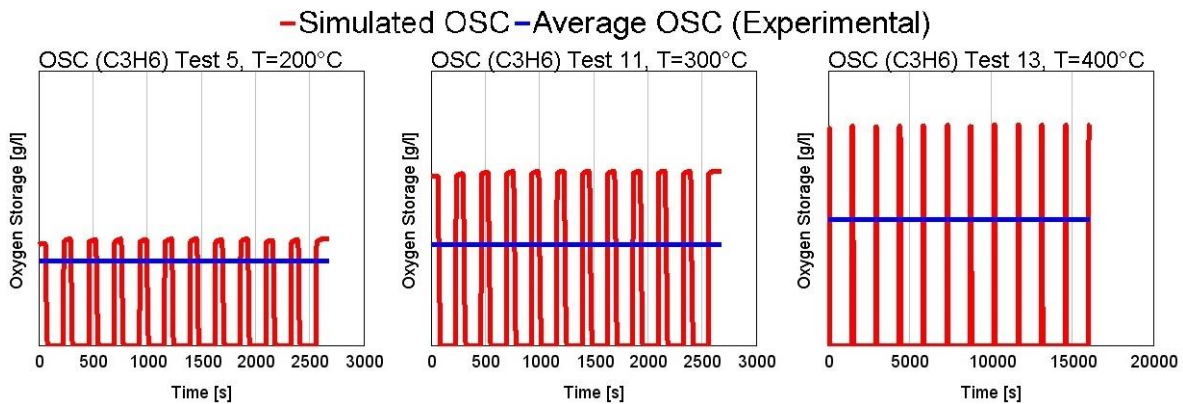


Figure 51 - OSC tests: 5 - 11 - 13 with C₃H₆ as reductant. The blue lines represent the average OSC estimated according the procedure from paragraph 2.1.2, while the red lines represents the simulated OSC.

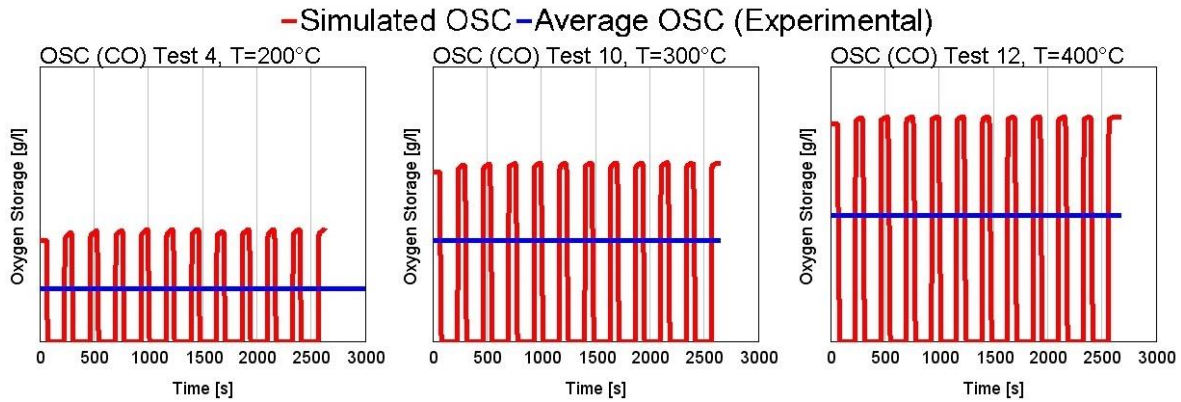


Figure 52 - OSC tests: 4 - 10 - 12 with CO as reductant. The blue lines represent the average OSC estimated according the procedure from paragraph 2.1.2, while the red lines represent the simulated OSC.

The OSC tests in correspondence of rich pulses (high concentrations of CO or C₃H₆ at sample inlet) were used to validate the capabilities of the model to detect the WGS and the SR. The assessment is focused only on tests with CO and C₃H₆ as reductant, because in case of tests with H₂ no outlet measurements of H₂ are available. The list of complete tests is reported in Table 12.

Figure 53 shows the correlation between simulation and experimental results of tests 1, 4, 10 and 12 of Table 12, where CO is the reductant species. In general, the model shows good predictive capabilities, since it is capable to detect correctly the O₂ consumption by means of oxidation (it corresponds to the delay between the inlet and outlet CO traces) and the WGS effect. However, at temperatures below 200°C the model is not capable to reproduce the peculiar shape of the experimental outlet trace.

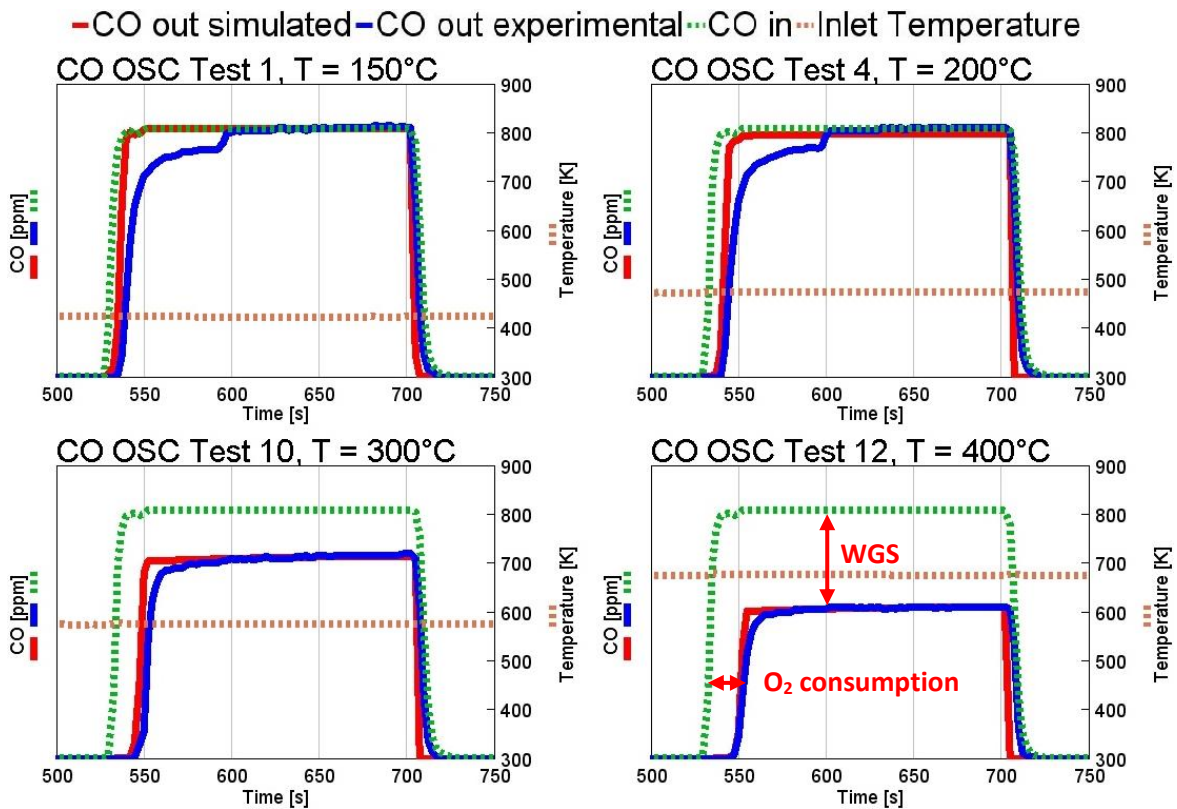


Figure 53 - Zoom between 500s and 750s of OSC tests 1, 4, 10, 12, with CO as reductant. The red line represents the simulation output, the blue line the experimental output, the green dashed line the inlet experimental NO and the orange dashed line the LNT inlet temperature profile.

Figure 54 illustrates the assessment of tests 2, 5, 11 and 13 of Table 12, where the reductant species is C₃H₆. As the CO case, the model shows good correlation with experimental results. In particular, it is capable to detect correctly the O₂ consumption, which is responsible of the delay between the inlet and outlet C₃H₆ trace, and the SR in the high temperature region. However, in the test 13, performed at 400°C, the experimental C₃H₆ outlet trace shows a smoother profile compared to the simulated one.

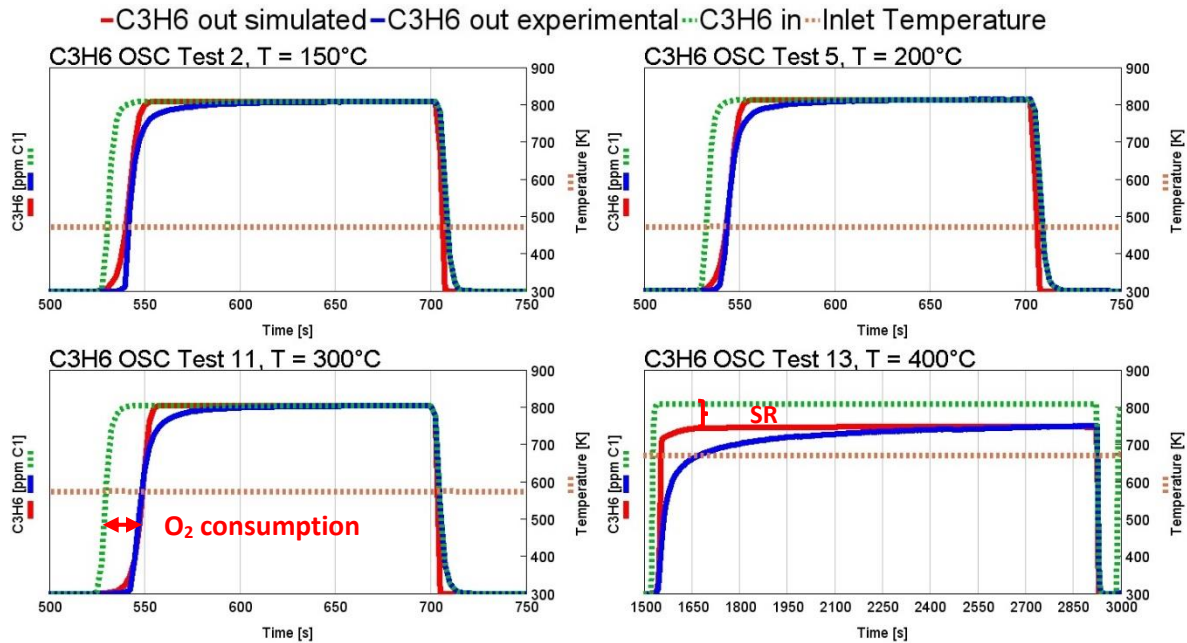


Figure 54 - Zoom between 500s and 750s of OSC tests 2, 5, 11 and between 1500s and 3000s of OSC test 13, with C_3H_6 as reductant. The red line represents the simulation output, the blue line the experimental output, the green dashed line the inlet experimental NO and the orange dashed line the LNT inlet temperature profile.

4.1.4 NO_x adsorption and desorption assessment

The assessment of NO_x adsorption and desorption is based on TPD tests, described in paragraph 2.1.3 and summarized in Table 13. The main focus of the assessment is oriented to tests with only NO in the feeding gas, because the NO_2/NO_x is usually very small and thus they are more representative of normal operating conditions of Diesel engines.

The first part is focused on tests with medium NO concentrations and low SV. Figure 55 shows the results of test 1 and 5 of Table 13, where the inlet temperature is respectively $100^\circ C$ and $150^\circ C$. The model in both cases is capable to capture the adsorption, which is negligible when the temperature is around $100^\circ C$. Moreover, the model is capable to simulate the two desorption peaks, which occur around $200^\circ C$ and $430^\circ C$. Finally, the NO oxidation and the NO_2 desorption are well correlated with the experimental results.

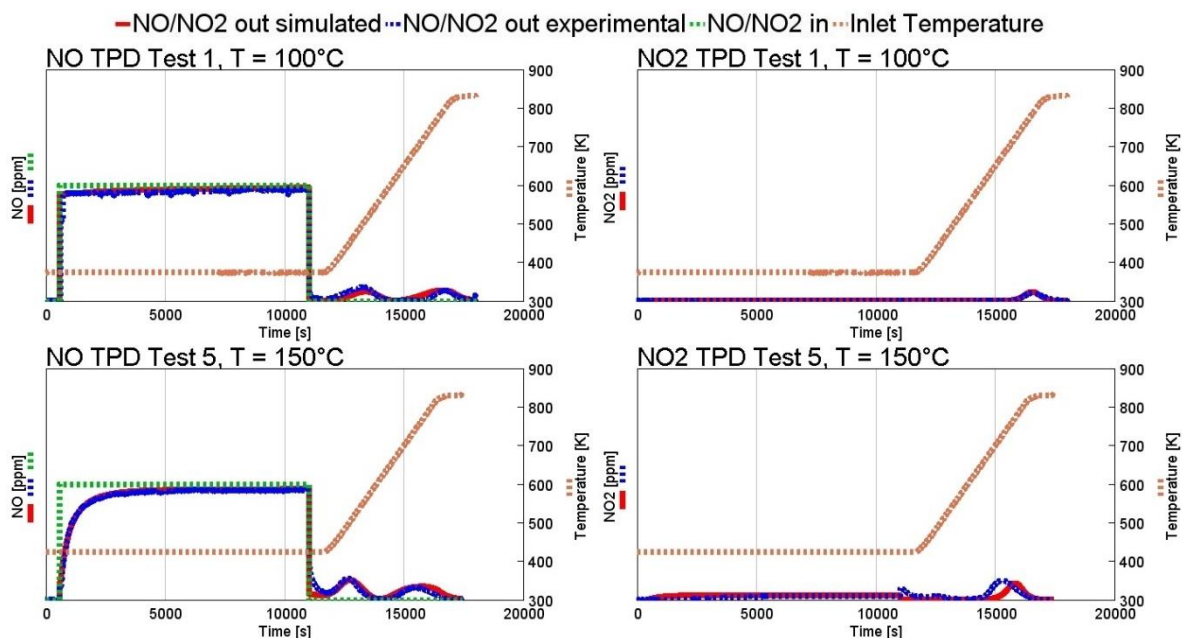


Figure 55 - TPD Test 1: $T=100^{\circ}\text{C}$ and Test 5: $T=150^{\circ}\text{C}$, medium NO concentrations, low SV (see Table 13). NO (left) and NO₂ (right) traces. The red line represents the simulation output, the blue dashed line the experimental output, the green dashed line the inlet NO and the orange dashed line the LNT inlet temperature profile.

Figure 56 shows the assessment of test 7 and 13 from Table 13. Test 7 was carried out with inlet temperature equal to 200°C , while Test 13 at 250°C . Within this temperature range, the NO oxidation becomes active. The model is capable to capture the magnitude of NO oxidation, because once the storage is completed the outlet NO emissions are different to inlet value and they are equivalent to experimental outlet. In this temperature region the LNT catalyst has the maximum storage capacity and the model is capable to capture such behavior for both NO and NO₂. Moreover, during the desorption phase the model identifies correctly the desorption peaks for both species, with a slight underestimation of the peak amplitude detected in some cases (e.g., Test 13).

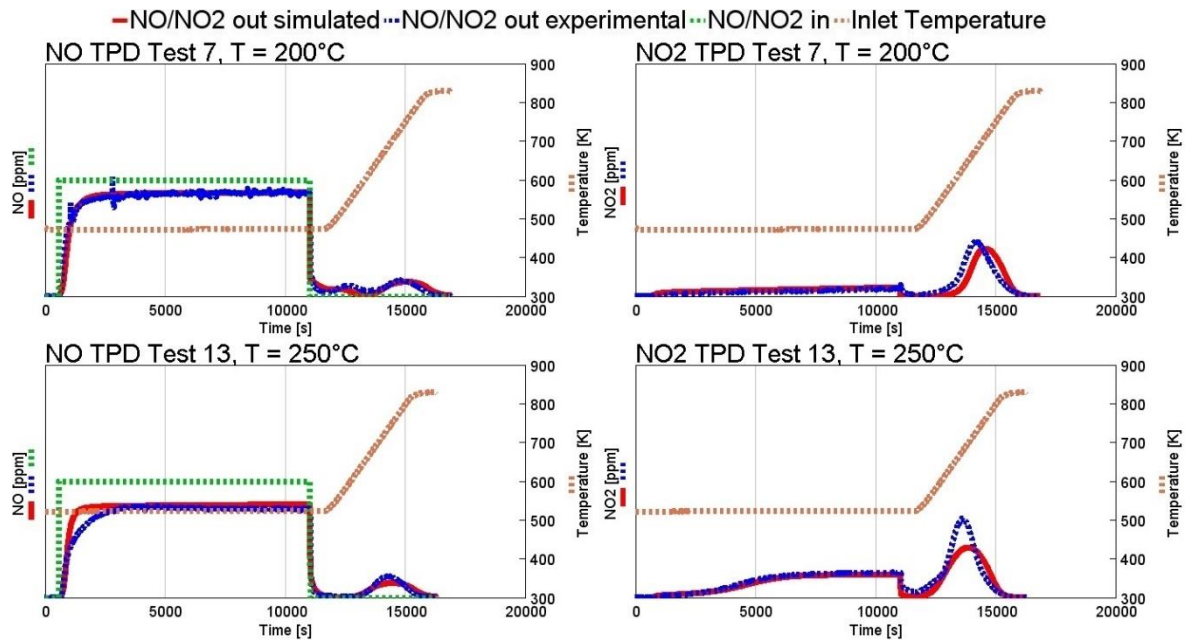


Figure 56 - Test 7: $T=200^{\circ}\text{C}$ and Test 13: $T=250^{\circ}\text{C}$, medium NO concentrations, low SV (see Table 13). NO (left) and NO_2 (right) traces. The red line represents the simulation output, the blue dashed line the experimental output, the green dashed line the inlet NO and the orange dashed line the LNT inlet temperature profile.

As depicted from Figure 57, for the temperature range comprised between 300 and 350°C , the catalyst is still able to store considerable quantities of NO and NO_2 . However, the Barium site available for NO adsorption at low temperature is no longer available. Model results perfectly correlate with experimental ones.

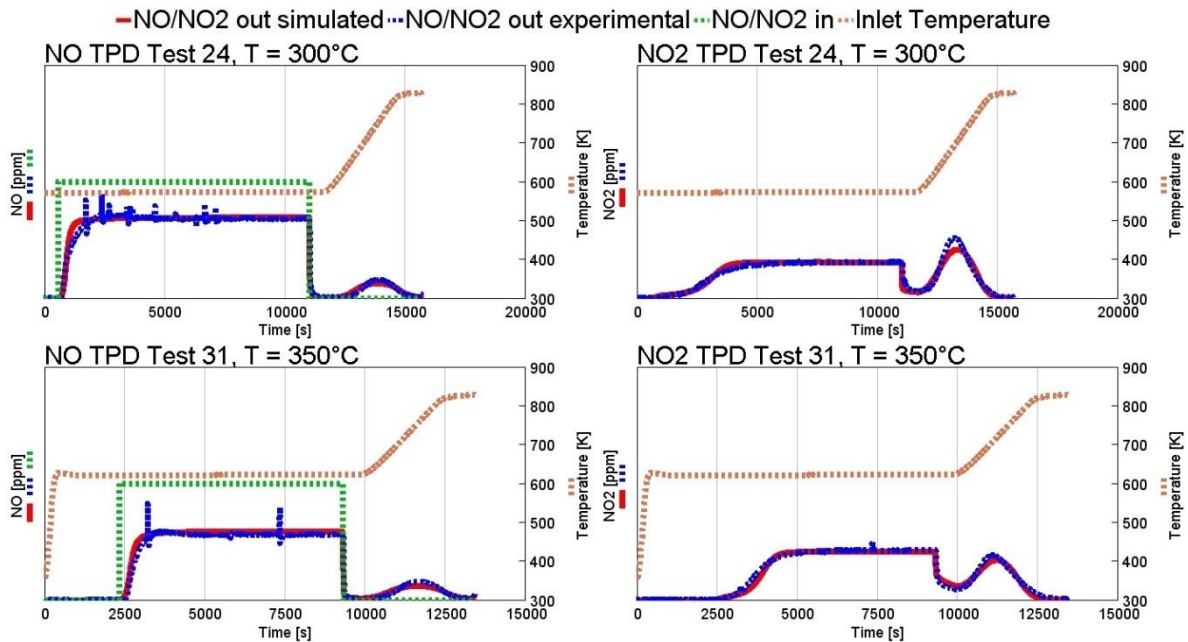


Figure 57 - Test 24: $T=300^{\circ}\text{C}$ and Test 31: $T=350^{\circ}\text{C}$, medium NO concentrations, low SV (see Table 13) . NO (left) and NO_2 (right) traces. The red line represents the simulation output, the blue dashed line the experimental output, the green dashed line the inlet NO and the orange dashed line the LNT inlet temperature profile.

For temperatures higher than 400°C the LNT catalyst shows a reduced adsorption capacity for both NO and NO_2 , as shown in Figure 58. The model is capable to predict this derated storage capacity, giving very low storage efficiency at high temperatures, where barium sites are not stable enough to store nitrogen oxides.

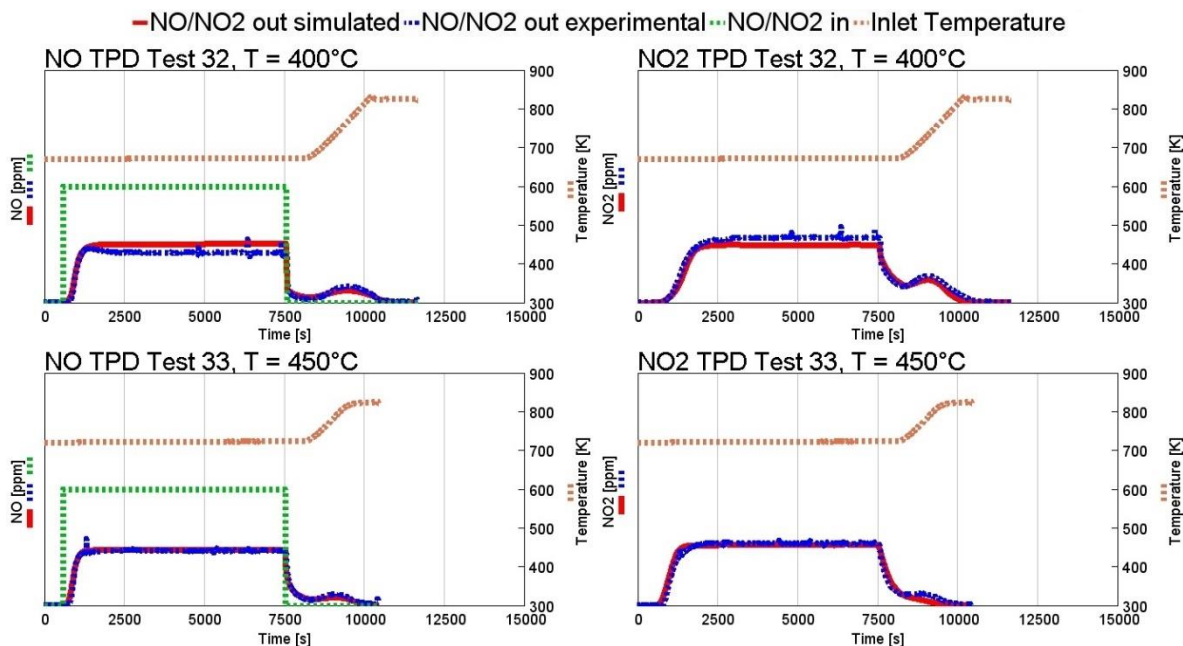


Figure 58 - Test 32: $T=400^{\circ}\text{C}$ and Test 33: $T=450^{\circ}\text{C}$, medium NO concentrations, low SV (see Table 13). NO (left) and NO₂ (right) traces. The red line represents the simulation output, the blue dashed line the experimental output, the green dashed line the inlet NO and the orange dashed line the LNT inlet temperature profile.

The second part of TPD validation is focused on the effect of SV, assuming equivalent concentrations of NO of previous tests (from Figure 55 to Figure 58). Figure 59 shows the results of tests 12 and 13 of Table 13, where the temperature of feeding gas is respectively 250°C and 275°C . The model is capable to capture both the dynamics of adsorption and of desorption, with some gaps in terms of steady state values. Due to the reduced residence time for catalysis of NO on Pt sites, the NO to NO₂ conversion should decrease with increasing SV [18, 40]. Model results seem to be in agreement with this statement, while experimental results show almost no change in NO conversion efficiency, as depicted by the comparison of test 13 (Figure 59) and test 12 (Figure 56).

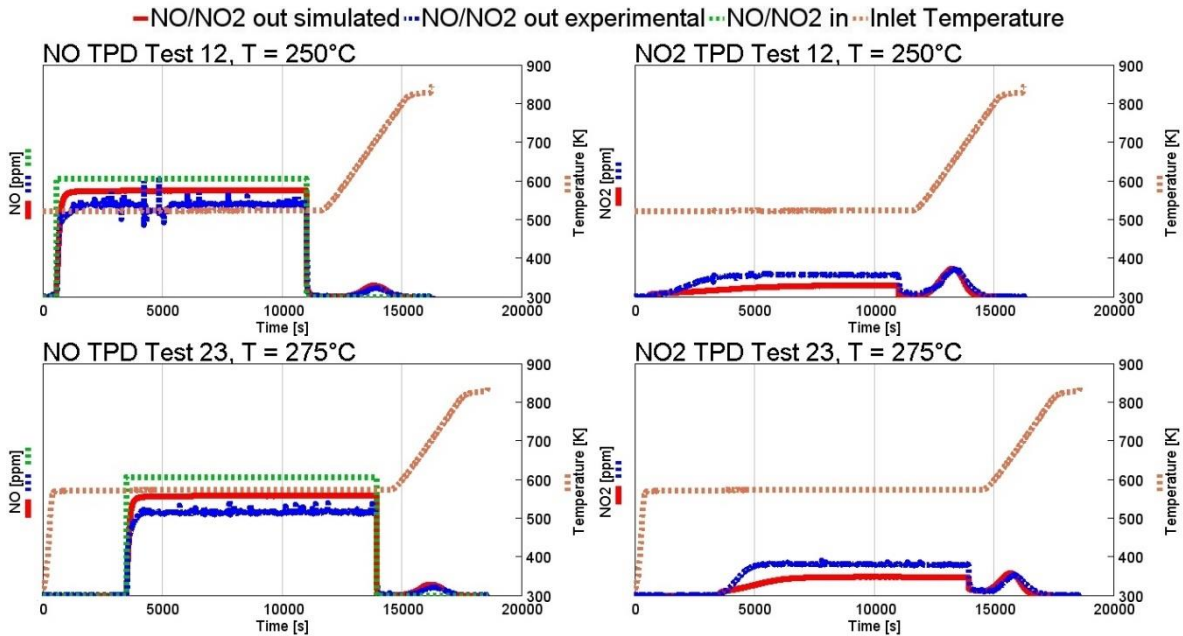


Figure 59 - Test 12: T=250°C and Test 23: T=275°C, medium NO concentrations, high SV (see Table 13). NO (left) and NO₂ (right) traces. The red line represents the simulation output, the blue dashed line the experimental output, the green dashed line the inlet NO and the orange dashed line the LNT inlet temperature profile.

The third step of TPD assessment focused on the effect of NO concentration, assuming a low SV. The results are shown in Figure 60 and Figure 61. In case of high NO concentrations (Figure 60), the model is capable to capture the reduction of NO₂ formation due the less availability of PGM sites compared to previous cases. Moreover, the model is capable to predict correctly the NO adsorption and desorption in the temperature range between 250°C and 300°C. On the contrary, the simulation slightly underestimates the NO₂ storage and consequently the amplitude of the desorption peak.

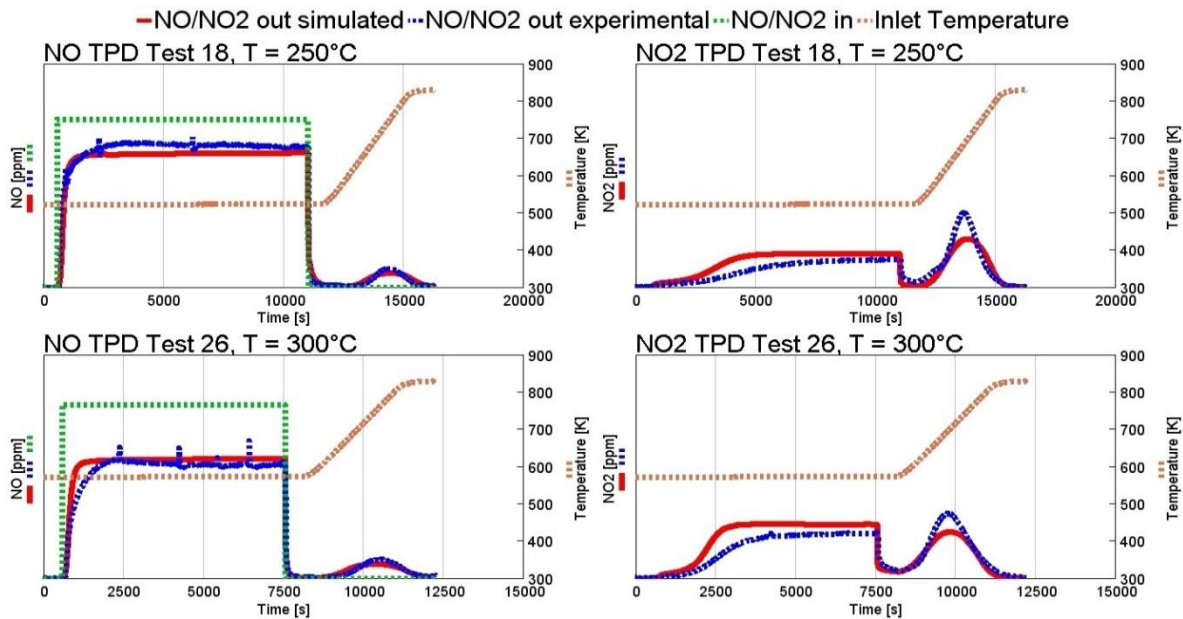


Figure 60 - Test 18: $T=250^{\circ}\text{C}$ and Test 26: $T=300^{\circ}\text{C}$, high NO concentrations, low SV (see Table 13). NO (left) and NO₂ (right) traces. The red line represents the simulation output, the blue dashed line the experimental output, the green dashed line the inlet NO and the orange dashed line the LNT inlet temperature profile.

In Figure 61 it is shown the scenario with low NO concentration in the feeding gas. In this case the model is well correlated for both NO and NO₂.

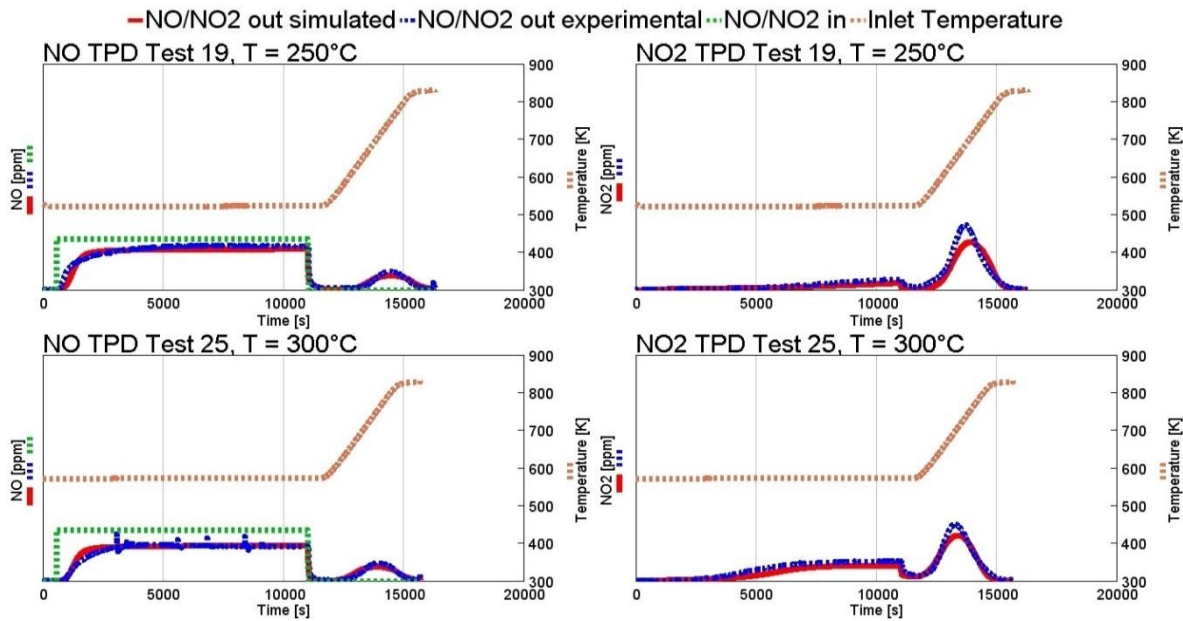


Figure 61 - Test 19: $T=250^{\circ}\text{C}$ and Test 25: $T=300^{\circ}\text{C}$, low NO concentrations, low SV (see Table 13). NO (left) and NO₂ (right) traces. The red line represents the simulation output, the blue dashed line the experimental output, the green dashed line the inlet NO and the orange dashed line the LNT inlet temperature profile.

The fourth assessment step focused on TPD tests with NO_2/NO ratio different from zero. The results are depicted in Figure 62. The analysis of the experimental results highlighted that the outlet NO emissions are higher than inlet ones (blue dashed lines of Figure 62, left). This is probably caused by Nitrate route reactions. This three steps adsorption route is represented by reaction 15 of Table 20. During NO_2 adsorption, this behavior leads to the release of one mole of NO for every three moles of NO_2 adsorbed by barium sites. This phenomenon was not observed during tests with only NO and O_2 in the feeding gas. Due to the lack of tests with different NO/NO_2 ratios, this reaction was made inactive and as a consequence the model is not able to capture such behavior.

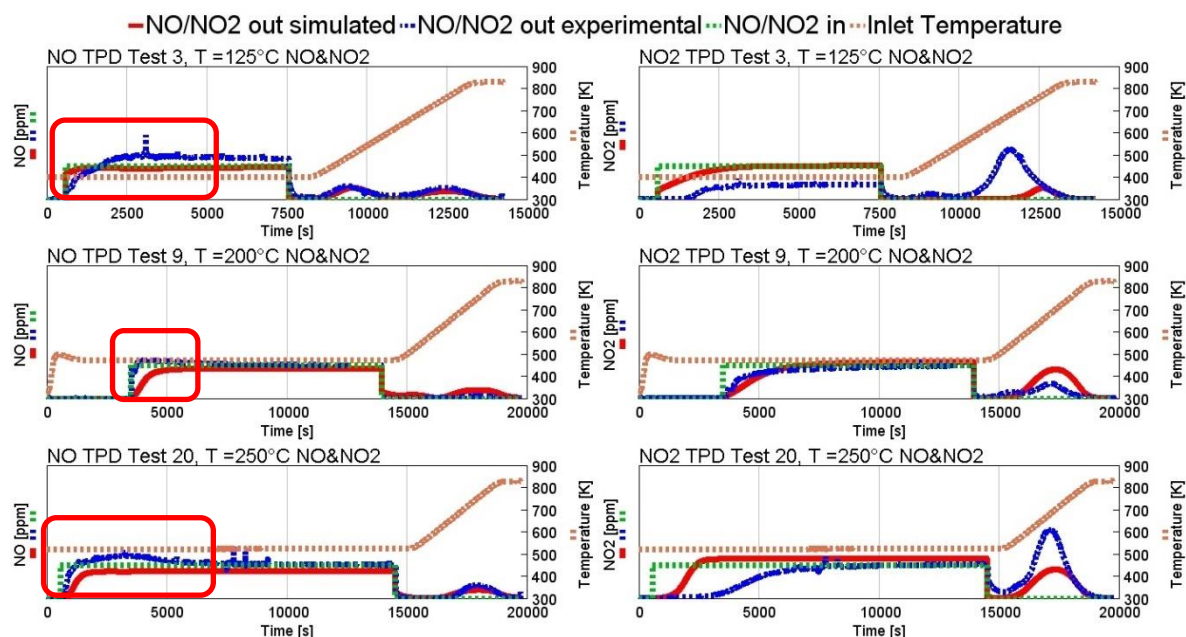


Figure 62 - Test 3: $T=125^{\circ}\text{C}$, Test 9: $T=200^{\circ}\text{C}$ and Test 20: $T=250^{\circ}\text{C}$, low concentrations of NO and NO_2 , low SV (see Table 13). NO (left) and NO_2 (right) traces. The red line represents the simulation output, the blue dashed line the experimental output, the green dashed line the inlet NO and the orange dashed line the LNT inlet temperature profile.

Finally, the TPD assessment was done based on tests with reducing species in the feeding gas, as depicted in Figure 63. The model is capable to predict with satisfactory accuracy experimental results. However, as showed in Figure 63 (plot relative to test 21) despite the NO_2 trace agrees with experimental results, model overestimates the NO outlet emissions during the constant temperature phase.

This discrepancy can be caused by:

1. The concentration of NO in the feeding gas is different from the nominal value;
2. The presence of a reduction mechanism that involve NO₂ and the rich species in the feeding gas (CO and HCs), leading to NO evolution.

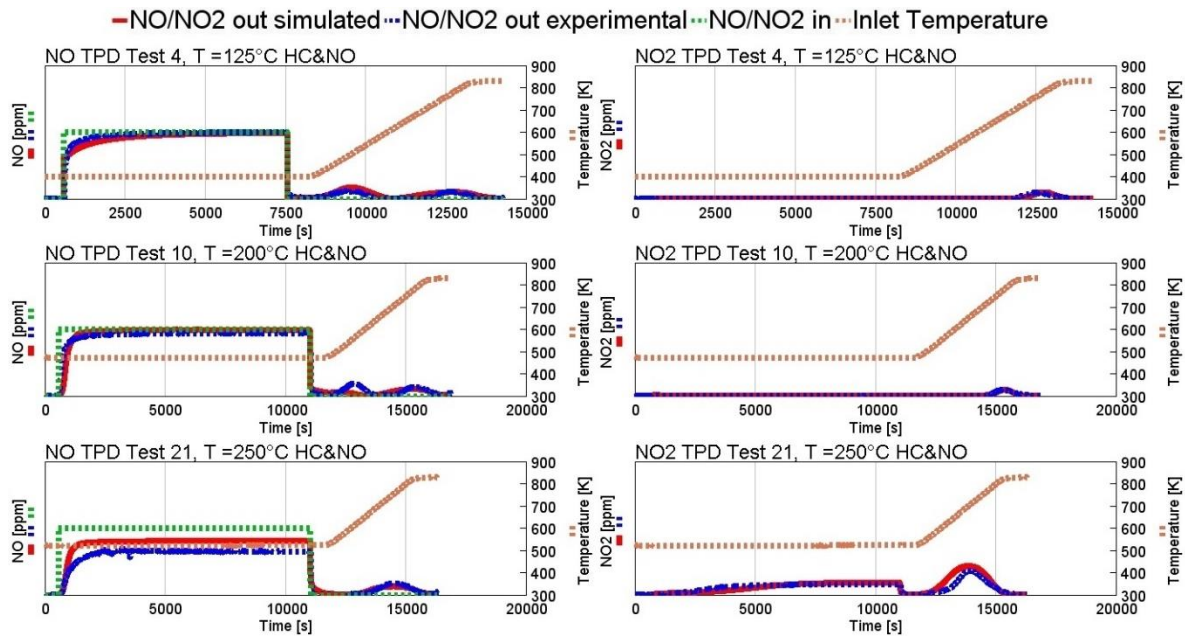


Figure 63 - Test 4: T=125°C, Test 10: T=200°C and Test 21: T=250°C, medium NO concentrations, low concentrations of CO and HCs, low SV (see Table 13). NO (left) and NO₂ (right) traces. The red line represents the simulation output, the blue dashed line the experimental output, the green dashed line the inlet NO and the orange dashed line the LNT inlet temperature profile.

4.1.5 NO_x reduction assessment

The assessment of NO_x reduction was carried out based on the NSR tests described in Table 14. The comparison between simulation results and experimental tests highlighted some discrepancies during the adsorption phase. This result was unexpected, because the TPDs analysis highlighted the good predictive capabilities of the model in a large interval of operating conditions. This chapter will present in the first part a brief comparison between the simulation results from NSR and TPD tests with the aim of identifying the reasons behind the divergences in the adsorption mechanisms. The last sections will focus on the assessment of the reduction mechanism with different reductants.

4.1.5.1 NSR adsorption phase

The experimental characterization of the adsorption mechanism with NSR and TPD tests was done based on homogeneous boundary conditions:

1. Inlet temperature from 200°C to 350°C;
2. Low SV;
3. Medium NO concentrations;
4. NO₂/NO equal to zero;
5. CO₂ Medium concentrations, H₂O Medium concentrations, O₂ High concentrations.

The analysis of the adsorption phase during the TPD and NSR tests is reported in Figure 64. The comparison between the TPD and NSR tests highlights:

1. A large discrepancy between the experimental outlet NO traces, which is representative of a different storage behavior (in case of TPD tests the NO storage capacity seems to be lower than NSRs, on the other hand, the NO₂ storage capacity during TPDs shows higher performance);
2. The inability of the model, calibrated on NO_x TPD tests, to capture the adsorption mechanism as from the NSR tests.

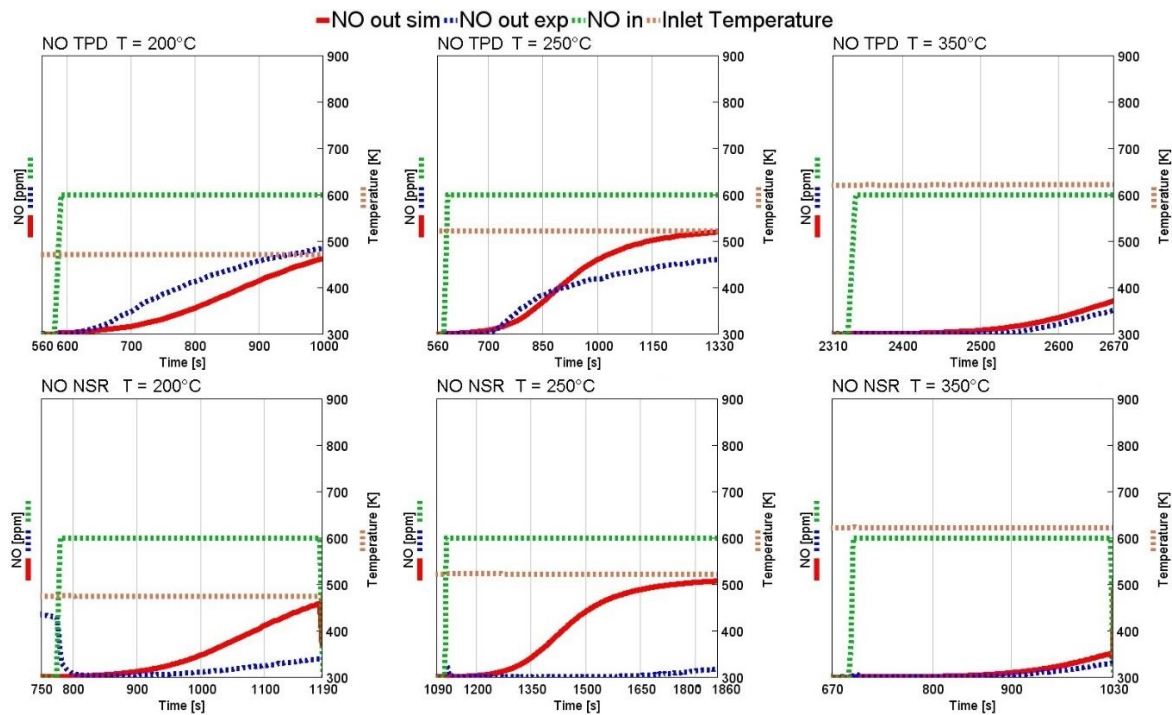


Figure 64 - Comparison between the NO loading phase sampled during TPD tests (Top) and NSR experiments (Bottom), with same atmosphere and temperature conditions. Red line is representative of simulated outlet NO, blue dashed line is the experimental outlet NO, green dashed line represents the inlet NO and orange dashed line is the inlet temperature profile.

Some assumptions were initially listed to explain the divergence between the TPD and NSR tests:

1. Different aging status of the samples;
2. Different initial coverages of barium sites between the two samples;
3. Different barium dispersion in the washcoat of the two samples;
4. Different preconditioning conditions for the two samples.

The first and third hypotheses are unlikely and should be discarded, because the samples were cored from the same full scale LNT and aged in the same way/conditions.

A different initial coverage on barium sites could be the explanation about the different storage capacity observed in the TPD and NSR tests. However, in case of TPD tests at high temperatures a residual storage capacity of NO_x should lead to a free desorption before the adsorption phase. Moreover, a short rich purge is applied on the sample at the end of the temperature ramp of the TPD tests to ensure the complete regeneration of the trap. Therefore, the zero-initial coverage on barium site should be fulfilled for all TPD tests.

The preconditioning procedure could be a reasonable explanation of the divergence between the TPD and NSR tests. As previously mentioned, between each TPD test a short rich purge was done at the end of the test to ensure the correct surface cleaning prior to the start of the next experiment. However, if this procedure can ensure the removing of all stored species, it is not sure that it is enough to recover all the catalytic activity of Pt sites. On the contrary, in case of NSR tests no rich pulses at the end of each test was planned. However, the experiment protocol consists of several lean/rich cycling, which should ensure the complete regeneration of the trap.

Different studies highlighted discrepancies in the NO_x loading between tests with long duration as TPDs and experiments with lean/rich cycling as NSRs [42,43,44]. This difference is probably caused by Pt particles oxidation (PtO_x) in lean environment, promoted in case of TPD tests by long NO_x loading in presence of high O_2 concentrations, which reduces the catalytic power of the LNT in terms of NO oxidation. Moreover, the formation of PtO_x is promoted by the high dispersion of Pt in the washcoat, which leads to the formation of small particles less resistant to the PtO_x formation. To reduce the formation of PtO_x sites, these studies highlighted that the use of NO as reductant at temperatures below 200°C is very effective, while, at higher temperatures, a rich pulse is the only way to restore the catalytic activity.

Based on such evidences from literature, the analysis of Figure 65 highlights:

1. In the high temperature region (above 350°C) the divergence between TPD and NSR test is negligible, because the NO oxidation is limited by thermodynamic equilibrium;
2. The deterioration of the catalytic activity caused by PtO_x is evident in the temperature range between 200°C and 350°C in TPD tests, because the NO is not active as reductant to limit the formation of PtO_x sites and the thermodynamic equilibrium does not limit the oxidation reaction as in case of the high temperature tests. On the contrary, in case of NSR tests, the shorter duration of NO_x loading phase and the succession of lean/rich events ensure the reduction of PtO_x sites, which leads to higher NO conversion to NO_2 .

The complete surface cleaning during NSR tests leads to an increase of the Pt catalytic activity, which results in higher NO_2/NO ratios. Therefore, in case of NSR tests the adsorption behavior changes, because with higher NO_2 concentrations the saturation of dedicated barium sites occurs in a lower amount of time than in TPD tests, as highlighted in Figure 65. Since the model calibration was oriented to capture the adsorption during the TPD tests, the model (red line in Figure 65) is not capable to capture such behavior.

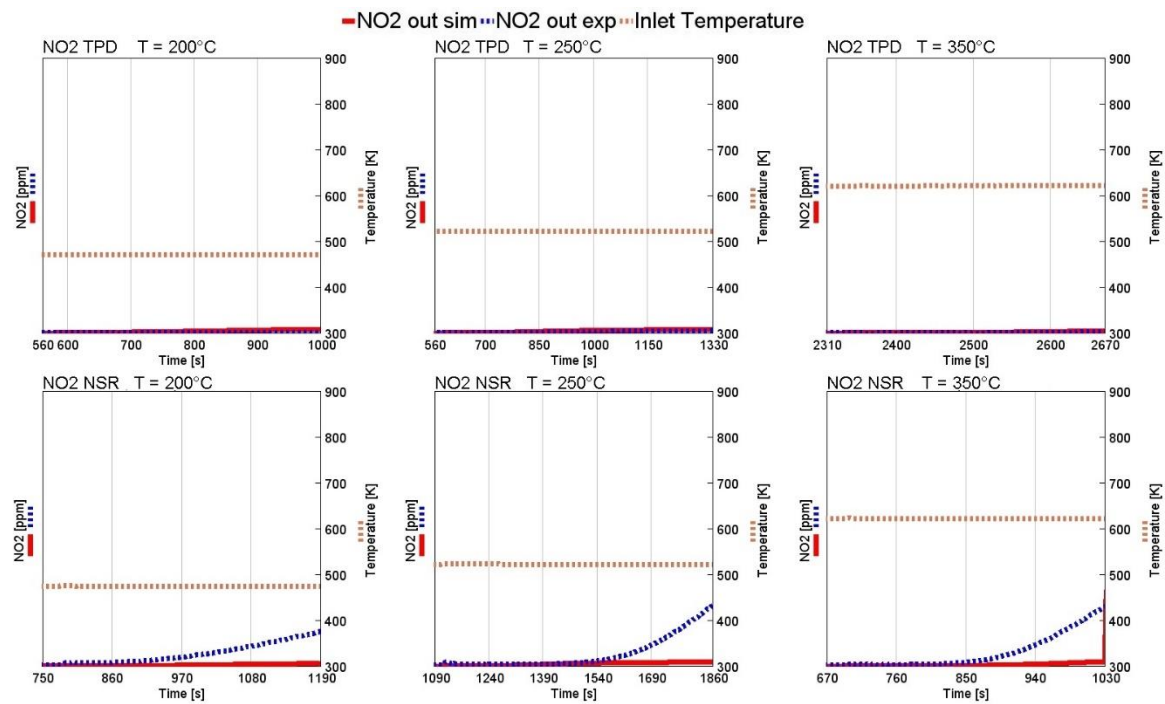


Figure 65 - Comparison between the NO₂ loading phase sampled during TPD tests (Top) and NSR experiments (Bottom), with same atmosphere and temperature conditions. The red line represents the simulated outlet NO₂ emissions, the blue dashed line is referred to the experimental outlet NO₂ and the orange dashed line is the inlet temperature profile.

4.1.5.2 NO_x reduction with CO as reductant

This section analyzes the main results of NSR tests with CO as reductant. Figure 66 illustrates the comparison between simulation and experimental results at 200°C. Three NSR tests are available with CO as reductant, performed at 200°C, 250°C and 350°C.

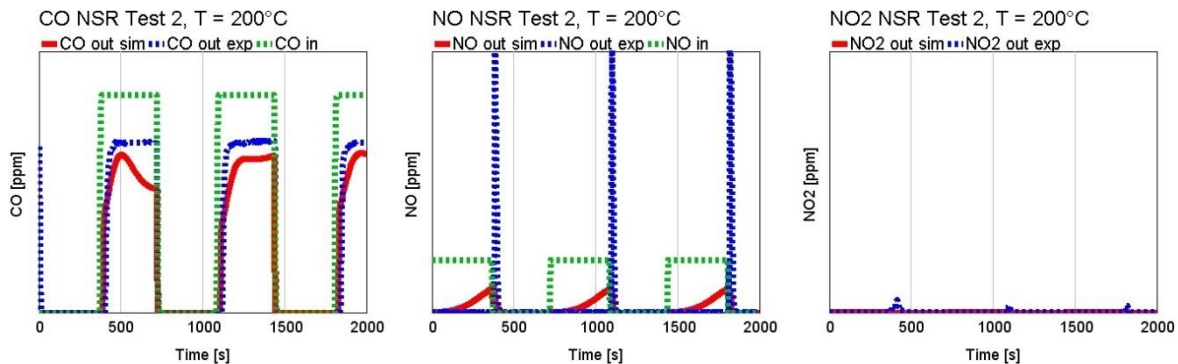


Figure 66 - CO (Left), NO (Center) and NO₂ (Right) out traces for NSR test 2 from Table 14, performed at T=200°C. Zoom in the 0-2000s time range. The red lines represent the simulated outlet emissions, the blue dashed ones the experimental outlet emissions and the dashed green lines the inlet concentrations.

The analysis of simulation results highlights that at 200°C the model underestimates the NO storage. The model simulates a fast saturation of barium sites, leading to higher NO outlet emissions than experimental ones. Moreover, the model cannot detect the NO spikes in correspondence of lean/rich transitions. Both the model and the experimental results show almost null values of NO₂ out emissions. This suggest that almost all NO₂ produced by NO oxidation is adsorbed and then reduced during rich phases.

Looking at Figure 67, the time delay between CO inlet and outlet traces, which is representative of the consumption of O₂ stored on cerium sites, is predicted with satisfactory accuracy. The WGS effect, which is the difference between the inlet and outlet CO curves during the plateau phase, is predicted with good precision. However, the model shows a strange behavior in the first rich phase. Differently from OSC tests, the WGS is already active at 200°C. This is probably caused by the higher catalytic activity of Pt sites already discussed in paragraph 4.1.5.1.

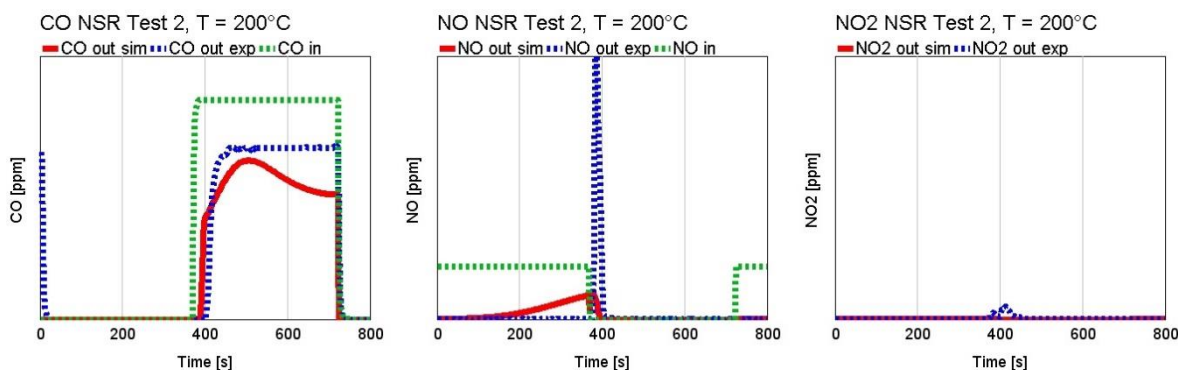


Figure 67 - CO (Left), NO (Center) and NO₂ (Right) out traces for NSR test 2 from Table 14, performed at T=200°C. Zoom in the 0-800s time range. The red lines represent the simulated outlet emissions, the blue dashed ones the experimental outlet emissions and the dashed green lines the inlet concentrations.

In case of the NSR test at 250°C, reported in Figure 68, the model shows a quite evident inaccuracy in capturing the WGS effect. This is probably due to the calibration of the high number of inhibition functions related to the WGS reaction, which leads to an overconsumption of CO. The underestimation of NO to NO₂ conversion is probably the main reason for the storage disagreement. If the model underestimates the NO to NO₂ conversion, this will lead to high NO concentrations and consequently to an early saturation of barium sites by means of NO and to a limited adsorption of NO₂. NO₂ desorption spikes are well predicted.

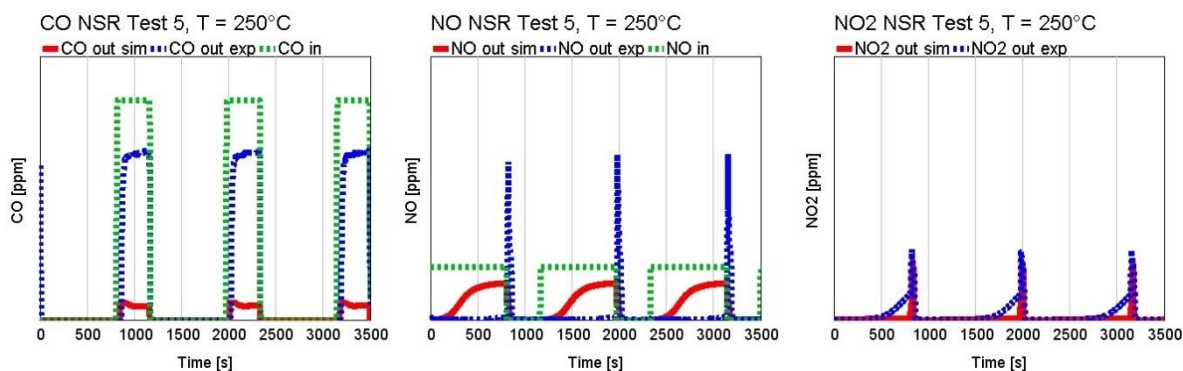


Figure 68 - CO (Left), NO (Center) and NO₂ (Right) out traces for NSR test 5 from Table 14, performed at T=250°C. Zoom in the 0-3500s time range. The red lines represent the simulated outlet emissions, the blue dashed ones the experimental outlet emissions and the dashed green lines the inlet concentrations.

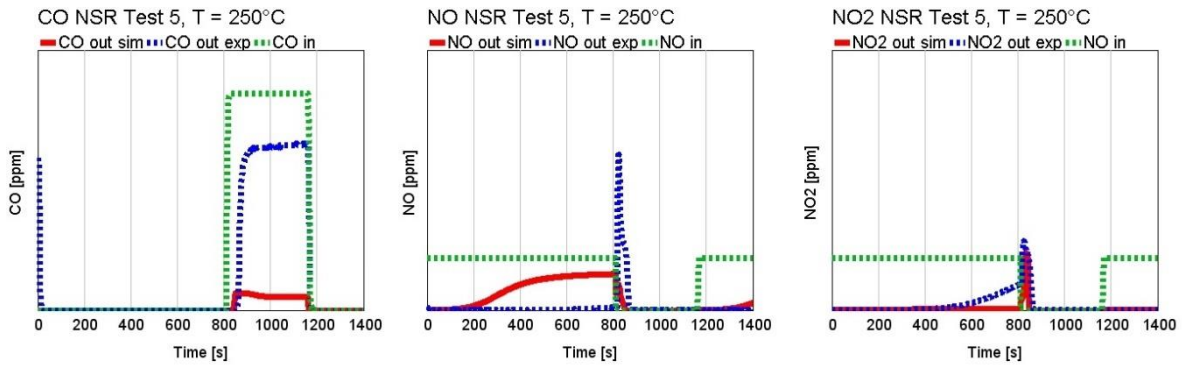


Figure 69 - CO (Left), NO (Center) and NO₂ (Right) out traces for NSR test 5 from Table 14, performed at $T=250^{\circ}\text{C}$. Zoom in the 0-1400s time range. The red lines represent the simulated outlet emissions, the blue dashed ones the experimental outlet emissions and the dashed green lines the inlet concentrations.

As shown in Figure 70 and Figure 71, at 350°C , despite the overestimation of the desorption peaks, the simulated NO storage agrees with experimental one. At this temperature the NO conversion is affected by thermodynamic equilibrium, thus the differences between the TPD based model and the experimental results decreases.

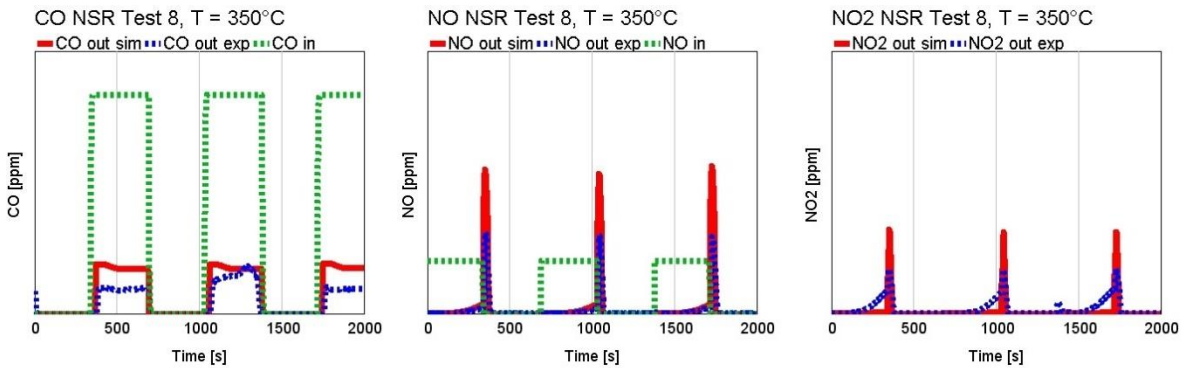


Figure 70 - CO (Left), NO (Center) and NO₂ (Right) out traces for NSR test 8 from Table 14, performed at $T=350^{\circ}\text{C}$. Zoom in the 0-2000s time range. The red lines represent the simulated outlet emissions, the blue dashed ones the experimental outlet emissions and the dashed green lines the inlet concentrations.

As depicted in Figure 71, the model overestimates the storage capacity of NO₂ compared to the experimental results. The WGS effect is slightly underestimated, but CO breakthrough curve have a good correlation with experimental one.

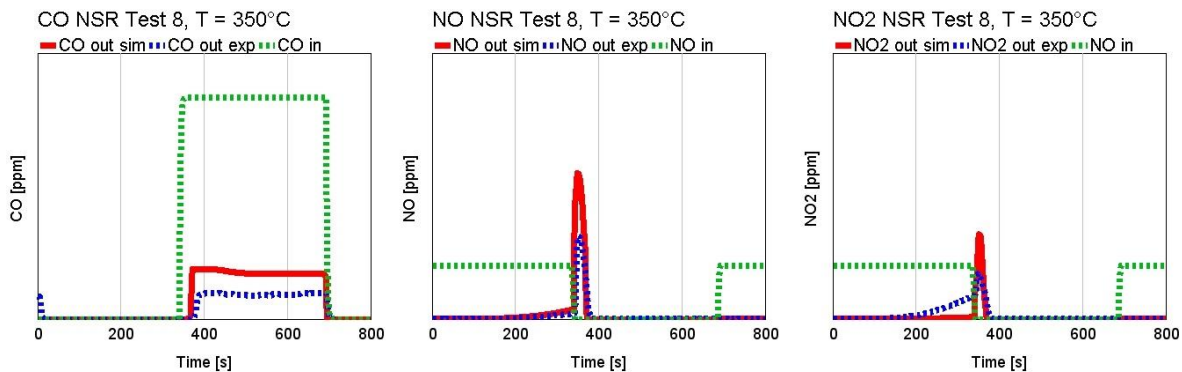


Figure 71 - CO (Left), NO (Center) and NO₂ (Right) out traces for NSR test 8 from Table 14, performed at T=350°C. Zoom in the 0-800s time range. The red lines represent the simulated outlet emissions, the blue dashed ones the experimental outlet emissions and the dashed green lines the inlet concentrations.

Since WGS reaction is already active at 200°C, NH₃ production is active because enough H₂ is available to reduce nitrites and nitrates. As depicted from Figure 72, the model is not capable to catch the ammonia production during NSR tests with CO as reductant.

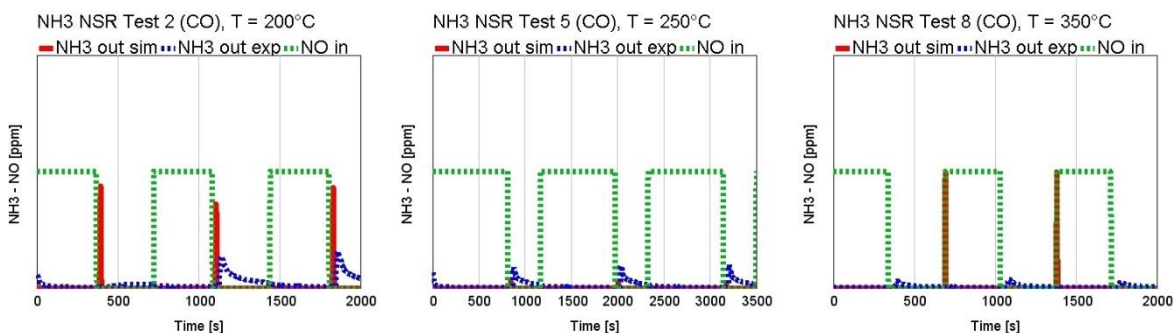


Figure 72 - NH₃ out traces from NSR tests of Table 14. From left to the right: Test 2 at T=200°C, Test 5 at T=250°C, Test 8 at T=350°C. The red lines represent the simulated NH₃ outlet emissions, the blue dashed ones the experimental NH₃ outlet emissions and the dashed green lines the NO inlet concentrations.

Figure 73 shows N₂O out emissions. According to experimental results, the simulated N₂O out decreases with increasing temperatures. However, outlet values are overestimated in the test performed at 200°C.

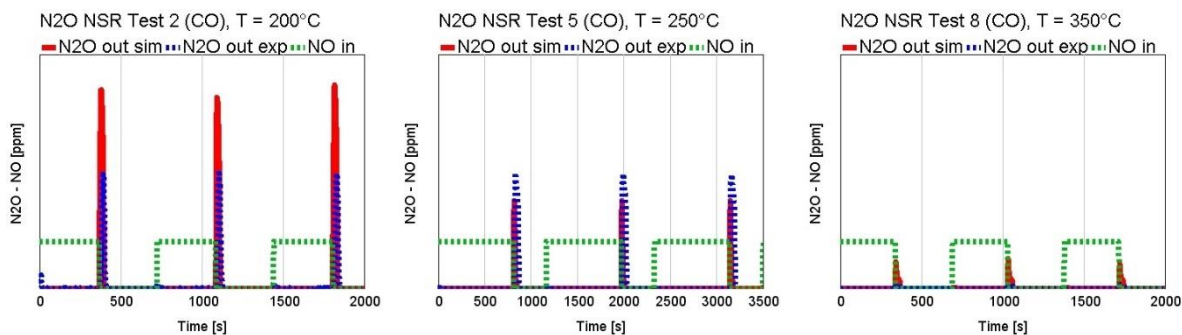


Figure 73 - N_2O out traces from NSR tests of Table 14 at different inlet temperature. From left to the right: Test 2 at $T=200^\circ C$, Test 5 at $T=250^\circ C$, Test 8 at $T=350^\circ C$. The red lines represent the simulated N_2O outlet emissions, the blue dashed ones the experimental N_2O outlet emissions and the dashed green lines the inlet NO concentration.

4.1.5.3 NO_x reduction with C_3H_6 as reductant

This section illustrates the results from NSR test with C_3H_6 as reductant. Three NSR tests are available with propylene as reductant, performed at $200^\circ C$, $250^\circ C$ and $350^\circ C$, as described in Table 14.

Figure 74 represents the results at $200^\circ C$. Compared to other NSR tests at $200^\circ C$, in case of C_3H_6 as reductant it is possible to observe that the outlet NO emissions are different from zero during the rich pulses. At this temperature the reduction reactions are still not completely active, leading to partial nitrates/nitrites reduction with NO evolution combined with the free thermal desorption of NO_x stored species into the flow. Compared to TPD the desorption occurs at lower temperature, because the rich atmosphere increases the desorption rate destabilizing nitrates and nitrites chemical bonds.

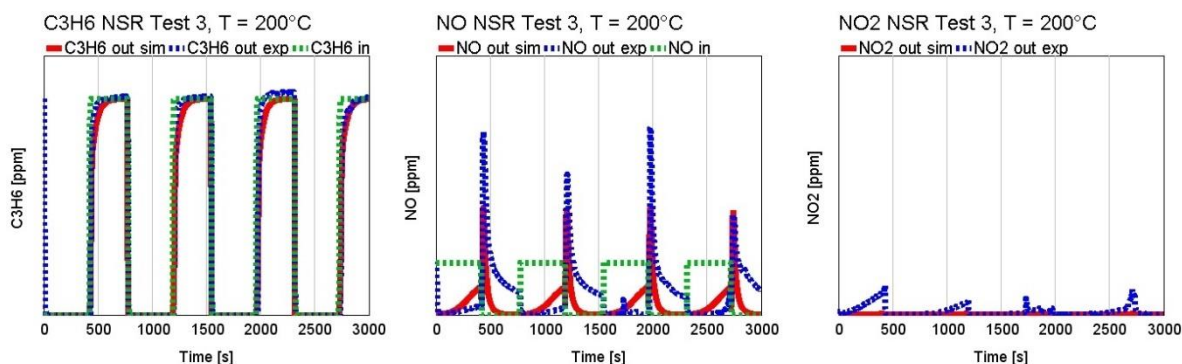


Figure 74 - C_3H_6 (Left), NO (Center) and NO_2 (Right) out traces for NSR test 3 from Table 14, performed at $T=200^\circ C$. Zoom in the 0-3000s time range. The red lines represent the simulated outlet emissions, the blue dashed ones the experimental outlet emissions and the dashed green lines the inlet concentrations.

Despite the implementation of a specific inhibition function to increase free thermal desorption in rich conditions, the simulated NO emissions are underestimated during the rich event, as depicted from Figure 75. On the contrary, during rich events the model is predictive of the C₃H₆ oxidation by means of O₂ stored in ceria sites.

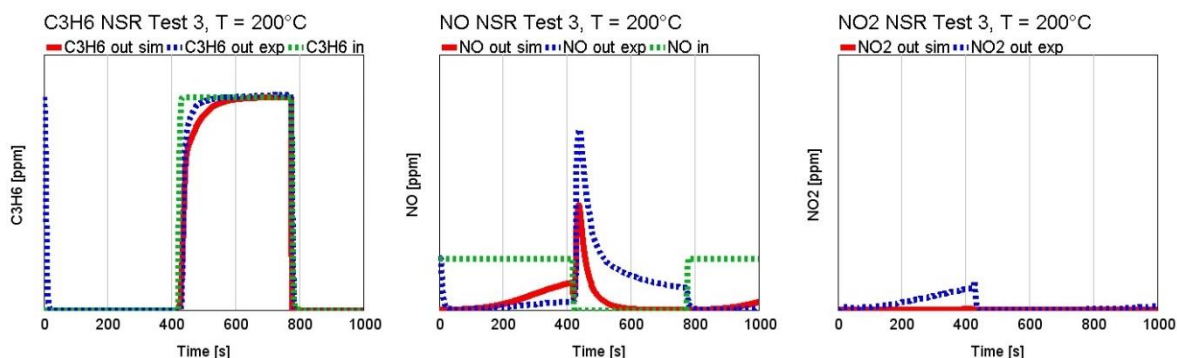


Figure 75 - C₃H₆ (Left), NO (Center) and NO₂ (Right) out traces for NSR test 3 from Table 14, performed at T=200°C. Zoom in the 0-1000s time range. The red lines represent the simulated outlet emissions, the blue dashed ones the experimental outlet emissions and the dashed green lines the inlet concentrations.

In case of test at 250°C reported in Figure 76, the simulation results show some similarity to the model results with CO as reductant, depicted in Figure 68. As for the CO case, the model underestimates the NO oxidation to NO₂, which leads to the early saturation of NO barium sites and consequently to an overestimation of NO in the exhaust flow. Moreover, the model underestimates both the NO and NO₂ spikes in correspondence of lean/rich transition. On the contrary, the model predicts correctly the C₃H₆ oxidation during the rich events, as depicted in Figure 77.

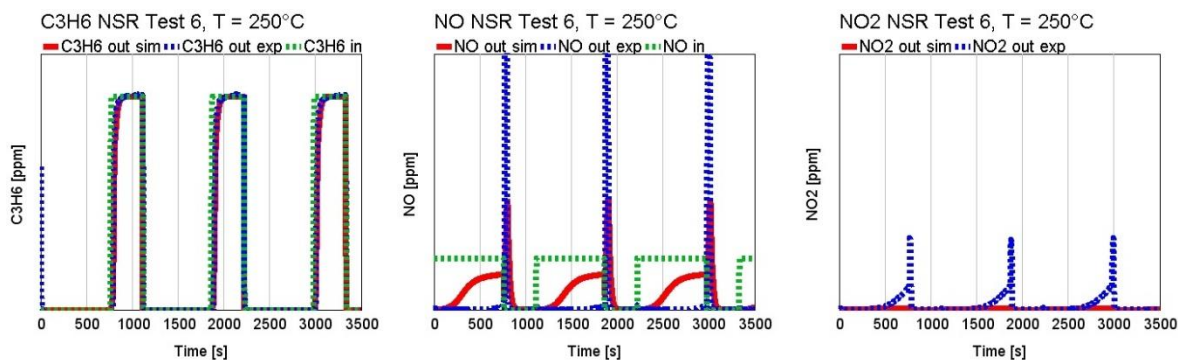


Figure 76 - C₃H₆ (Left), NO (Center) and NO₂ (Right) out traces for NSR test 6 from Table 14, performed at T=250°C. Zoom in the 0-3500s time range. The red lines represent the simulated outlet emissions, the blue dashed ones the experimental outlet emissions and the dashed green lines the inlet concentrations.

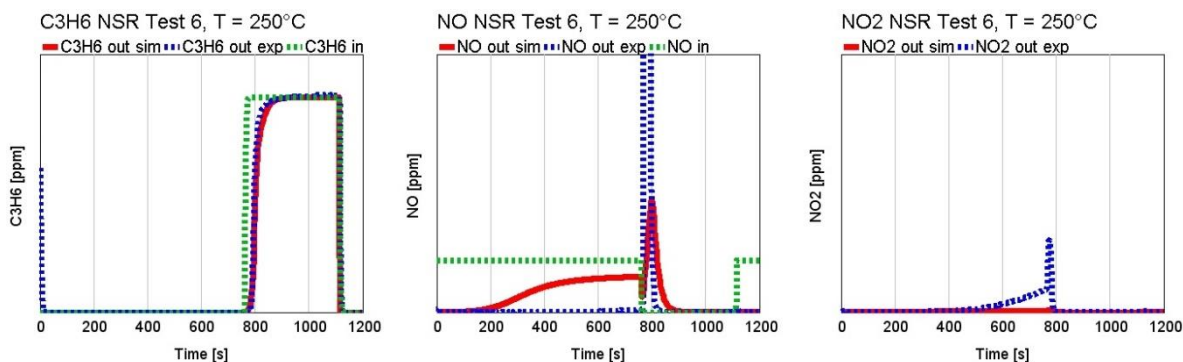


Figure 77 - C_3H_6 (Left), NO (Center) and NO_2 (Right) out traces for NSR test 6 from Table 14, performed at $T=250^\circ C$. Zoom in the 0-1200s time range. The red lines represent the simulated outlet emissions, the blue dashed ones the experimental outlet emissions and the dashed green lines the inlet concentrations.

Considering the test performed at 350°C, shown in Figure 78, model prediction agrees with the experimental one. In case of C_3H_6 the model is capable to predict with high accuracy the SR and the oxidation by means of OSC, as highlighted in Figure 79. Moreover, the NO adsorption and desorption are well correlated with experimental results. This happens because the storage of NO is limited by the thermodynamic equilibrium as in the TPD tests. On the contrary, the model overestimates the NO_2 adsorption.

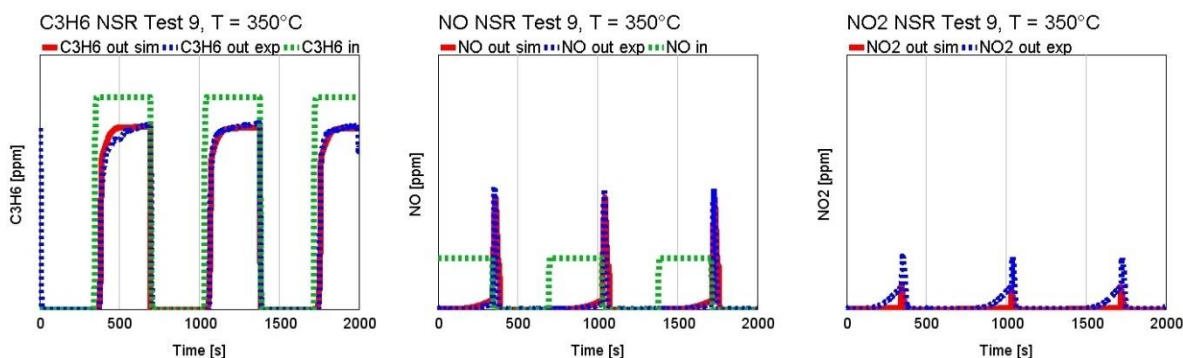


Figure 78 - C_3H_6 (Left), NO (Center) and NO_2 (Right) out traces for NSR test 9 from Table 14, performed at $T=350^\circ C$. Zoom in the 0-2000s time range. The red lines represent the simulated outlet emissions, the blue dashed ones the experimental outlet emissions and the dashed green lines the inlet concentrations.

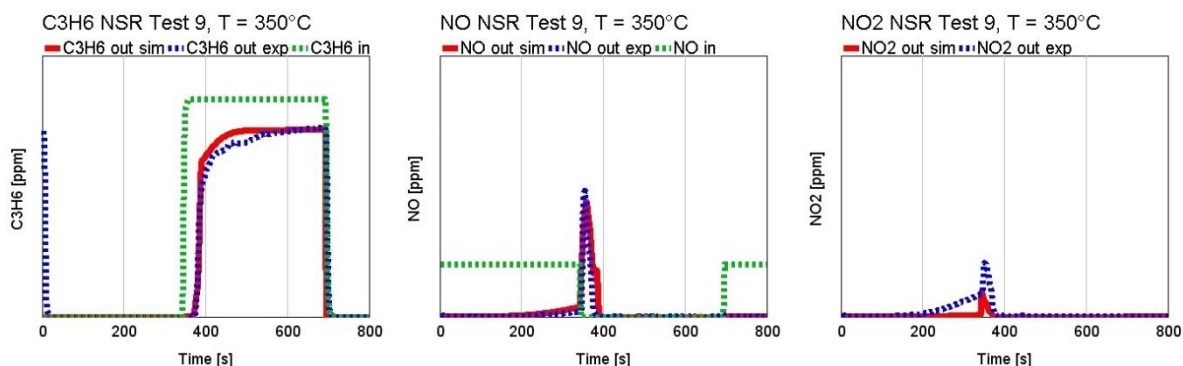


Figure 79 - C_3H_6 (Left), NO (Center) and NO_2 (Right) out traces for NSR test 9 from Table 14 performed at $T=350^\circ C$. Zoom in the 0-800s time range. The red lines represent the simulated outlet emissions, the blue dashed ones the experimental outlet emissions and the dashed green lines the inlet concentrations.

As highlighted in Figure 80, no NH_3 formation is highlighted when C_3H_6 is used as reductant at $200^\circ C$. On the other hand, despite the model is capable to predict SR within the considered temperature range, in the high temperature region (above $250^\circ C$) the model is not capable to catch the NH_3 production.

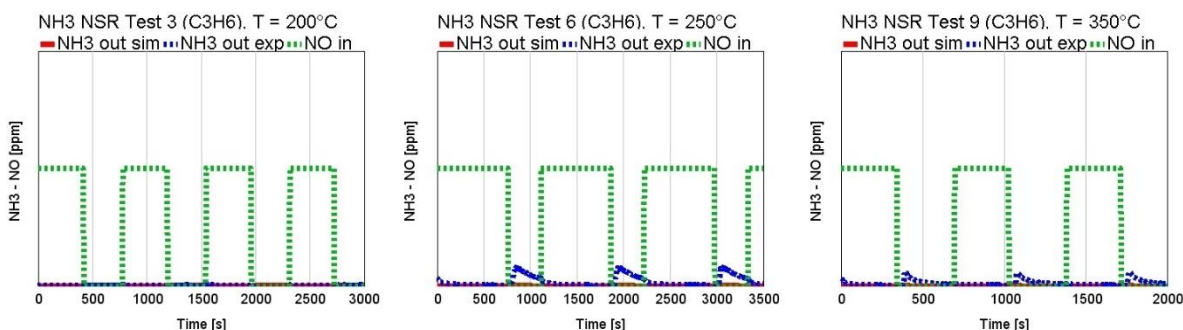


Figure 80 - NH_3 out traces for NSR test from Table 14: Test 3 at $T=200^\circ C$ (left), Test 6 at $T=250^\circ C$ (Center), Test 9 at $T=350^\circ C$ (Right). The red lines represent the simulated NH_3 outlet emissions, the blue dashed ones the experimental NH_3 outlet emissions and the dashed green lines the NO inlet concentrations.

The capability of the model to predict N_2O formation is shown in Figure 81. The analysis of the experimental results highlights that on average the N_2O formation occurs at the end of the NO/O_2 loading phases. However, observing results below $250^\circ C$, the formation of N_2O is clearly evident also at the beginning of the lean phases. Probably, these peaks are produced by the reaction between gaseous NO with the residual propylene from the previous rich phase. The model is well correlated with experimental N_2O trace in correspondence of lean/rich transitions, but it is not capable to predict the N_2O formation at the beginning of the lean phase.

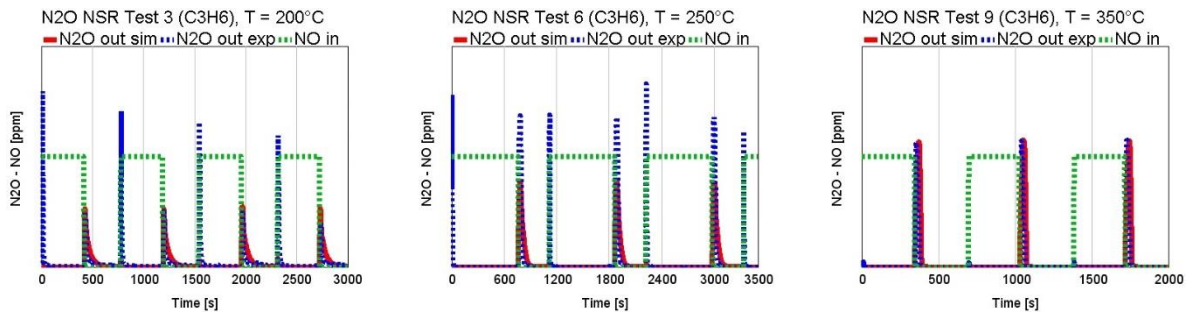


Figure 81 - N_2O out traces from NSR tests of Table 14: Test 3 at $T=200^\circ C$ (Left), Test 6 at $T=250^\circ C$ (Center), Test 9 at $T=350^\circ C$ (Right). The red lines represent the simulated N_2O outlet emissions, the blue dashed ones the experimental N_2O outlet emissions and the dashed green lines the inlet NO concentrations.

4.1.5.4 NO_x Reduction with H_2 as reductant

According to Table 14, three NSR tests with H_2 as reductant are available at $200^\circ C$, $250^\circ C$ and $350^\circ C$. Unfortunately, the H_2 breakthrough curves are not available. Therefore, the calibration was performed with aim to match outlet NO and NO_2 traces, as described in paragraph 3.3.4. The model results from the considered NSR test are depicted in Figure 82 and Figure 83.

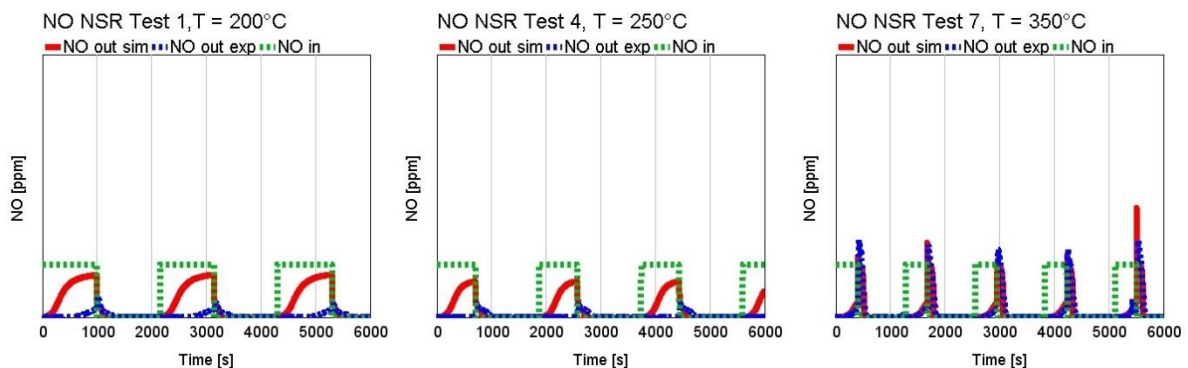


Figure 82 - NO out traces for NSR test from Table 14: Test 1 at $T=200^\circ C$ (Left), Test 4 at $T=250^\circ C$ (Center), Test 7 at $T=350^\circ C$ (Right). The red lines represent the simulated outlet emissions, the blue dashed ones the experimental outlet emissions and the dashed green lines the inlet concentrations.

The storage behavior is underestimated by the model during the lean phases at low temperatures (below $250^\circ C$). Moreover, the analysis of experimental results highlights that the NO slip does not occur in correspondence of lean/rich transition at temperatures between

200°C and 250°C, because the adsorbed species are instantaneously reduced by means of H₂ and NH₃.

In case of experiments at 350°C depicted in Figure 82, model prediction agrees with experimental results both during the adsorption and desorption phases.

Moving to the analysis of outlet NO₂ emissions illustrated in Figure 83, the experimental results highlight that the catalyst shows better NO to NO₂ conversion compared to test with CO and C₃H₆ as reductant. This is probably caused by the higher reduction efficiency of H₂ than CO and C₃H₆, which is more capable to regenerate the catalyst surface and, thus, oxidized Pt sites, boosting the NO oxidation. Model results are well correlated with experimental ones at 250°C. However, for the test performed at higher temperature, the model overestimates both the NO₂ storage and the desorption spikes.

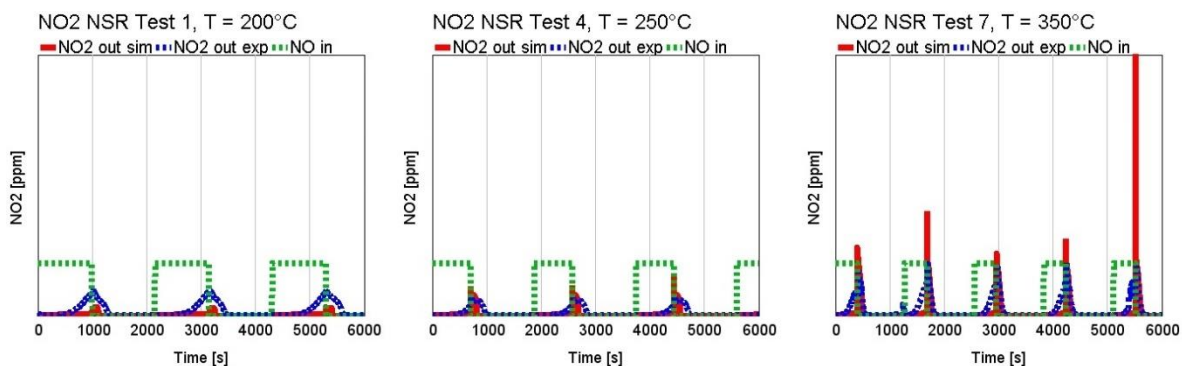


Figure 83 - NO₂ out traces for NSR test of Table 14: Test 1 at T=200°C (Right), Test 4 at T=250°C (Center), Test 7 at T=350°C (Left). The red lines represent the simulated outlet emissions, the blue dashed ones the experimental outlet emissions and the dashed green lines the inlet concentrations.

Figure 84 represents the NH₃ formation in case of NSR tests with H₂ as reductant. As described in paragraph 3.3.4, the use of H₂ as reductant leads to the formation of NH₃, which reduces the NO_x stored in the LNT. This mechanism is confirmed by the experimental evidence in Figure 84, because during this phase no NH₃ slip is observed. Once the NO_x stored is consumed, the NH₃ slip is observed at the outlet of the catalyst. The model is capable at 200°C to detect the amount of ammonia slipped, but it can be observed a delay between the experimental and the simulated outlet NH₃ emissions. At high temperatures, no formation of ammonia is observed for both experimental and simulated results.

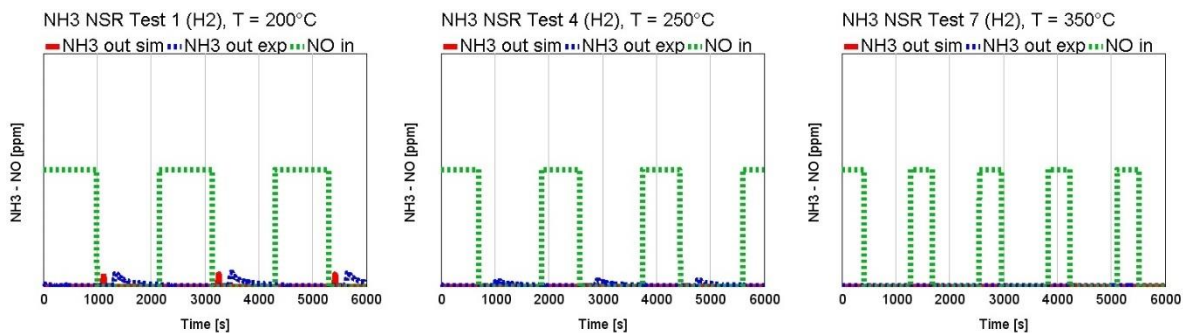


Figure 84 - NH_3 out traces from NSR tests of Table 14: Test 1 at $T=200^\circ\text{C}$ (Left), Test 4 at $T=250^\circ\text{C}$ (Center), Test 7 at $T=350^\circ\text{C}$ (Right). The red lines represent the simulated NH_3 outlet emissions, the blue dashed ones the experimental NH_3 outlet emissions and the dashed green lines the NO inlet concentration.

The capability of the model to predict N_2O formation in case of H_2 as reductant is reported in Figure 85. The DeNO_x by means of NH_3 production (2 steps mechanism described in paragraph 3.3.4) leads to the production of N_2O at low temperatures. The model can predict with acceptable accuracy the formation of N_2O at the end of lean phases, but it underestimates the produced quantity.

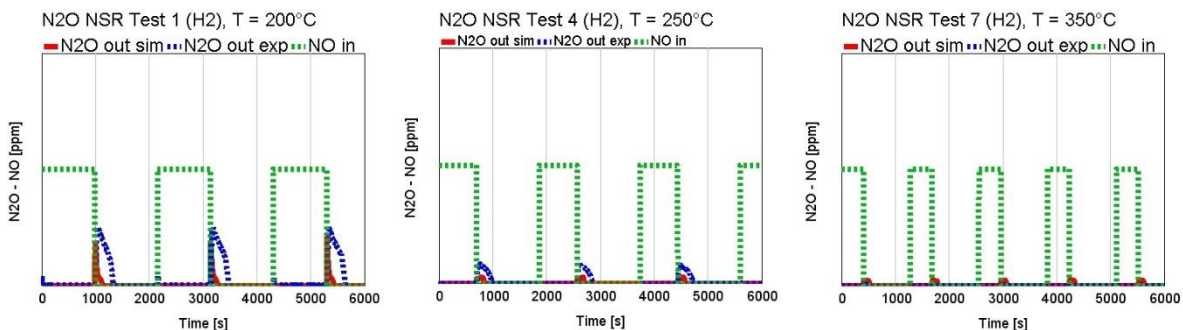


Figure 85 - N_2O out traces from NSR tests of Table 13: Test 1 at $T=200^\circ\text{C}$ (Left), Test 4 at $T=250^\circ\text{C}$ (Center), Test 7 at $T=350^\circ\text{C}$ (Right). The red lines represent the simulated N_2O outlet emissions, the blue dashed ones the experimental N_2O outlet emissions and the dashed green lines the inlet NO concentrations.

4.2 Model assessment on full scale tests

The assessment of the full-size LT-LNT model was done based on chassis dyno measurements over the WLTC and the RDE cycles. The model used for SGB validation was updated increasing the volume, adding the insulation material and the canning. A first loop of simulations was carried out using the calibration of the chemical model as determined from the analysis of the SGB testing results. Based on the achieved results, some refinements were applied to that calibration in order to improve the matching between simulations results and experimental data.

The main goals of the assessment in transient conditions are:

1. Verify the capabilities of the model to predict the catalyst outlet temperature and the outlet emissions (CO, NMHC, NO_x, NO and NO₂);
2. If needed, update the model calibration to improve the matching with measurements in transient conditions.

Reported results already consider, for both the WLTC and the RDE cycles, the calibration refinements mentioned above. The refining procedure is explained in paragraph 4.2.2, which is focused on RDE cycles.

4.2.1 WLTP cycles results

The complete list of WLTC cycles considered for the full-scale model validation is reported in Table 16. For sake of brevity, the detailed analysis of simulation results from two WLTC cycles will be shown:

1. **WLTC 18**: it is representative of a “Cold Start” WLTC with a DeNO_x event. The preconditioning of the cycle consisted into a DPF regeneration followed by a series of DeNO_x events;
2. **WLTC 17**: It is referred to a “Hot Start” WLTC with a DeNO_x. The preconditioning consisted of a “Cold Start” WLTC.

Considering the cold WLTC, the cycle starts almost at ambient temperature. Temperatures sampled at the catalyst outlet are predicted with satisfactory results. However, in some conditions are slightly underestimated. Simulated temperature peak in correspondence of rich pulse is in good agreement with experimental values. Figure 86 shows the comparison between simulated and experimental outlet temperature referred to WLTC 18.

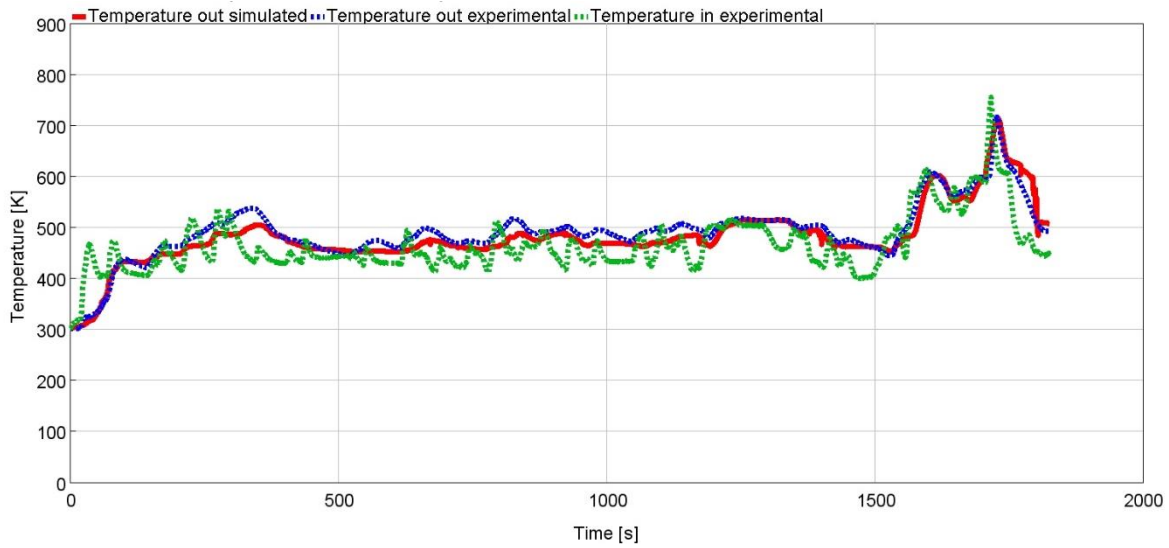


Figure 86 - Comparison between simulated and experimental outlet temperatures referred to Cold WLTC 18. The red line is referred to the simulated trace, the blue dashed line to the experimental one and the green dashed line to the catalyst inlet temperature.

Figure 87 shows the comparison between the simulated and the experimental outlet emissions, focusing on NMHC and CO. In case of CO the model underestimates the conversion efficiency during the DeNO_x event.

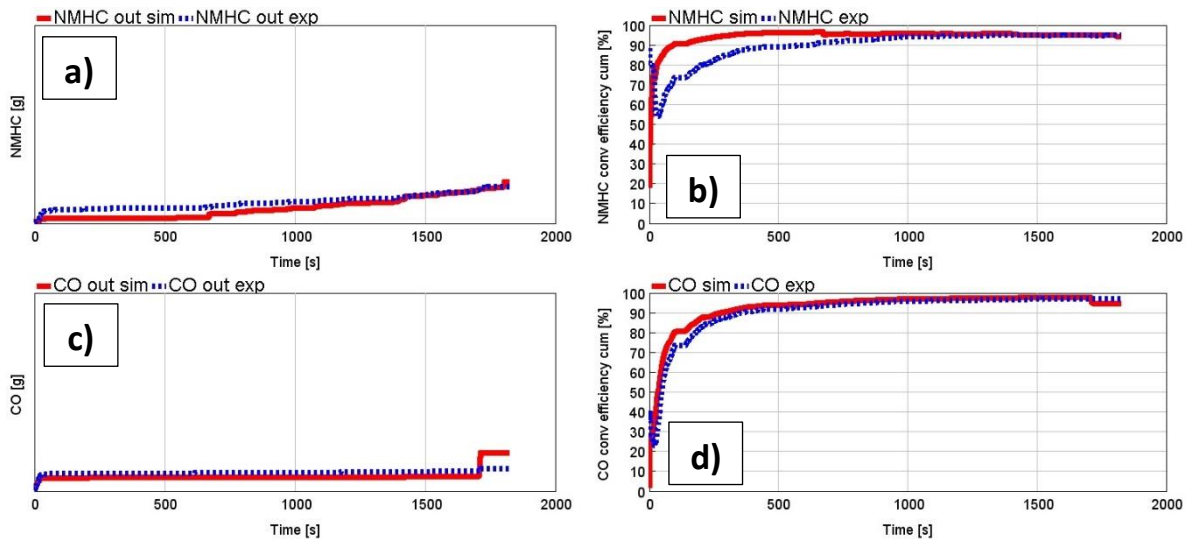


Figure 87 - Simulation results from WLTC 18: a) NMHC cumulated emissions, b) NMHC conversion efficiency, c) CO cumulated emissions, d) CO conversion efficiency. The red line represents the simulated value and the dashed blue is referred to the experimental result.

The comparison between simulated and experimental NO_x emissions in case of WLTC 18 is reported in Figure 88. The model is capable to estimate correctly the cumulated NO_x emissions over the WLTC cycle, depicted in Figure 88 c). However, the detailed analysis of NO and NO_2 cumulated emissions, Figure 88 a) and b), highlights that the model slightly overestimates the catalytic activity in terms of NO oxidation to NO_2 .

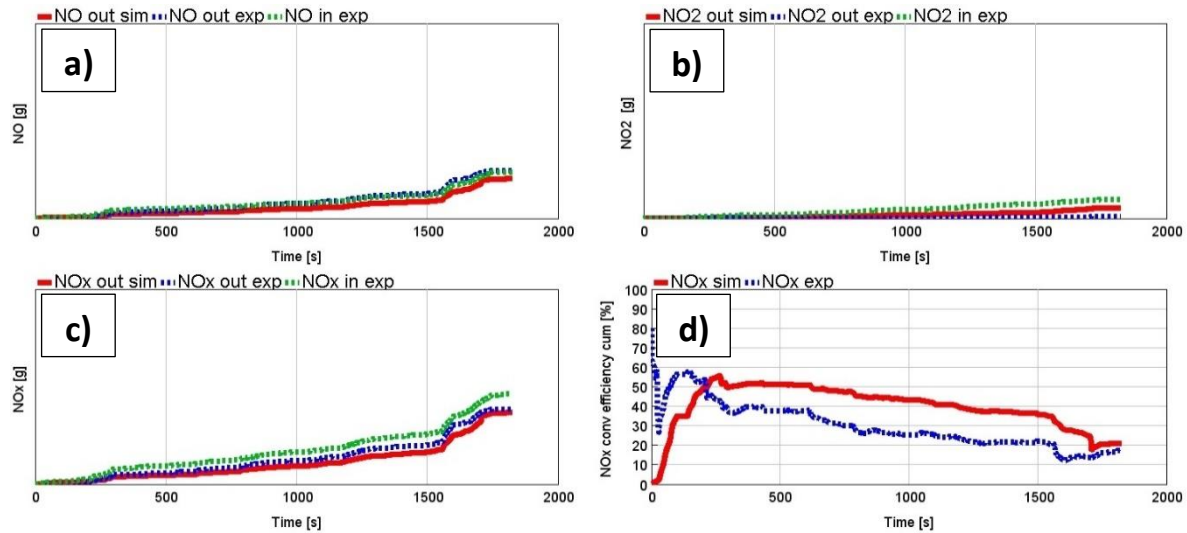


Figure 88 - Simulation results from WLTC 18: a) NO cumulated emissions, b) NO_2 cumulated emissions, c) NO_x cumulated emissions, d) NO_x conversion efficiency. The red line represents the simulated value, the dashed blue is referred to the experimental result and the dashed green to the inlet emissions.

The comparison between simulation and experimental outlet temperature is reported in Figure 89 in case of WLTC 17. The model is capable to predict with good accuracy the catalyst outlet temperatures during all the cycle.

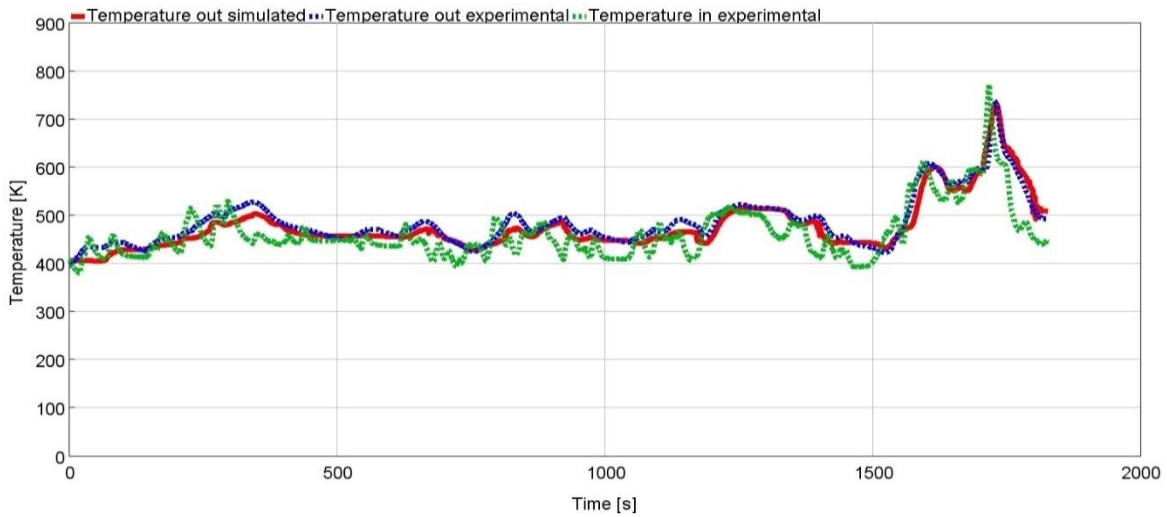


Figure 89 - Comparison between simulated and experimental outlet temperatures referred to Hot WLTC 17. The red line is referred to the simulated trace, the blue dashed line to the experimental one and the green dashed line to the catalyst inlet temperature.

The capability of the model to predict the NMHC and CO emissions in case of “Hot Start” WLTC is reported in Figure 90. In this case the model overestimates the conversion efficiency, in particular along the “Mid” phase of WLTC.

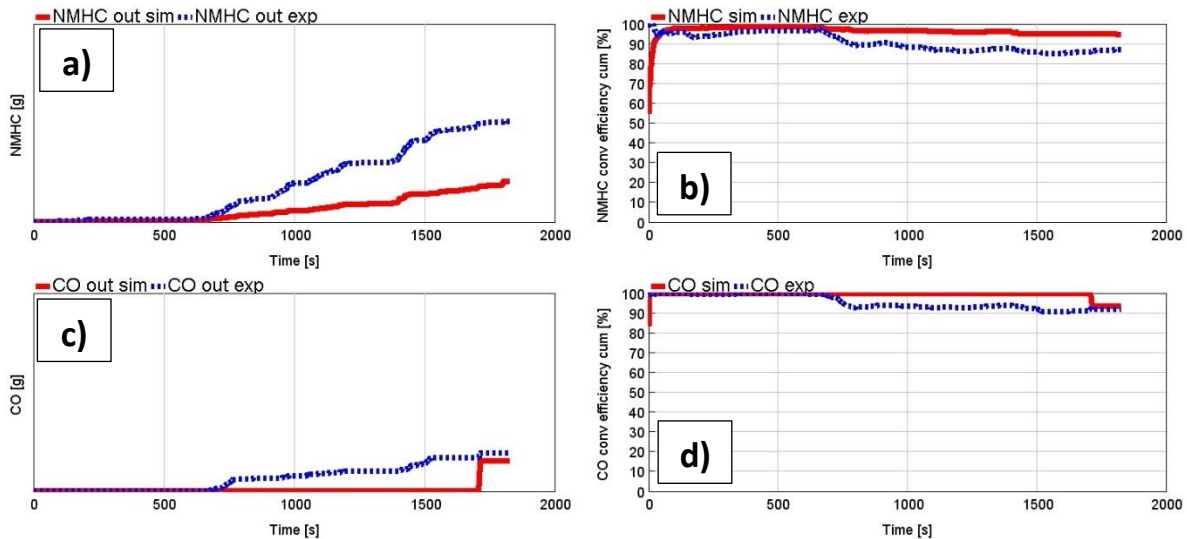


Figure 90 - Simulation results from WLTC 17: a) NMHC cumulated emissions, b) NMHC conversion efficiency, c) CO cumulated emissions, d) CO conversion efficiency. The red line represents the simulated value and the dashed blue one is referred to the experimental result.

The analysis of NO_x performance is reported in Figure 91. As highlighted for the “Cold Start” case, the model is overall capable to predict correctly the cumulated NO_x emissions.

However, the detailed analysis of NO_x performance points out that the model overestimates NO₂ outlet values.

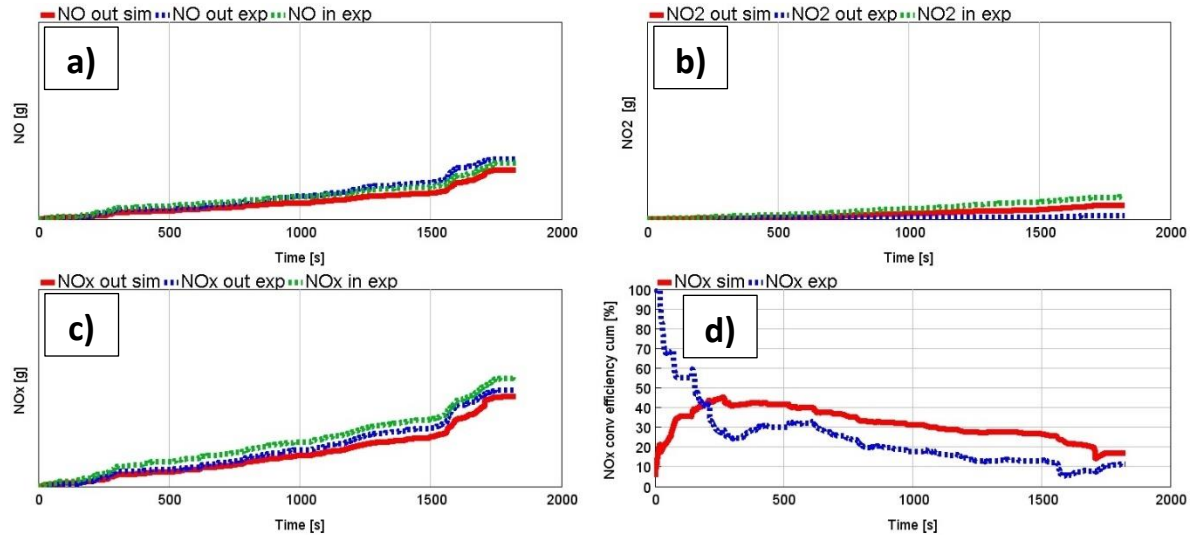


Figure 91 - Simulation results from WLTC 17: a) NO cumulated emissions, b) NO₂ cumulated emissions, c) NO_x cumulated emissions, d) NO_x conversion efficiency. The red line represents the simulated value, the dashed blue is referred to the experimental result and the dashed green to the inlet emissions.

4.2.2 RDE cycles results

The complete list of RDE cycles considered for the LNT assessment is reported in Table 17. For sake of brevity, the detailed analysis of simulation results from two RDE cycles will be shown:

1. **RDE 2:** it is a “Cold Start” cycle without DeNO_x events. The preconditioning of the cycle consisted into a DPF regeneration followed by a series of DeNO_x events;
2. **RDE 3:** it is a “Cold Start” cycle, but in this case the DeNO_x strategy is enabled. The preconditioning consisted into a DPF regeneration followed by a series of DeNO_x events.

In Figure 92 it is reported the thermal validation in case of RDE 2. As in the case of WLTC, the temperature at the catalyst outlet is predicted with good accuracy.

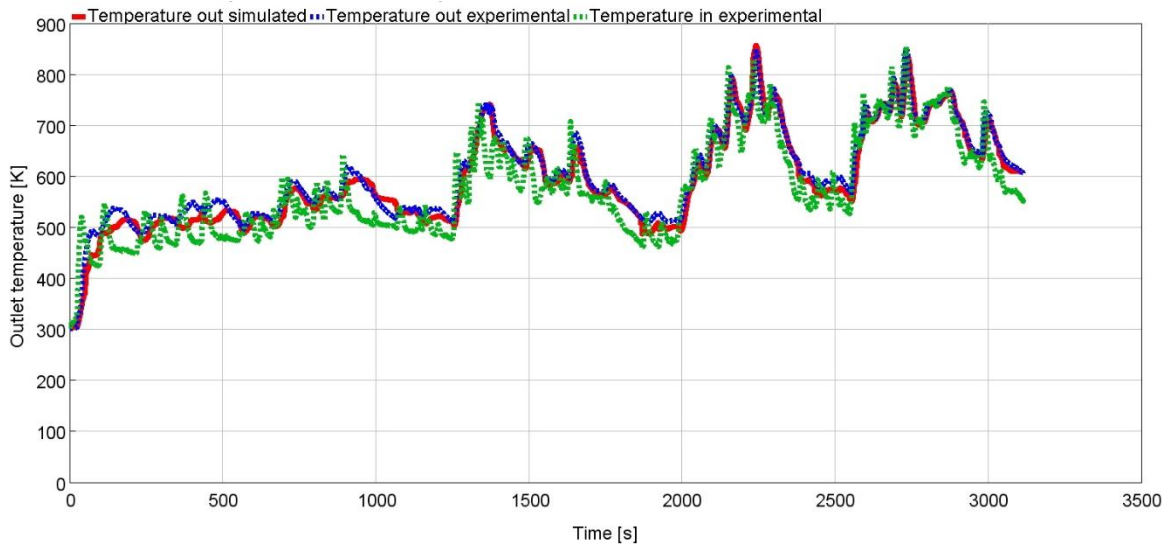


Figure 92 - Simulated and experimental outlet temperature referred to RDE 2. The red line is referred to the simulated trace, the blue dashed line to the experimental one and the green dashed line to the catalyst inlet temperature.

The model assessment over the RDE cycle requested the refinement of the calibration to improve the estimation of NMHC and CO emissions. In particular, the improvement focused on the calibration of the Arrhenius terms to increase the oxidation rates for both NMHC and CO. Moreover, the inhibition term of NO related to CO oxidation was reduced. The results from the updated model calibration are reported in Figure 93. The analysis of simulation results highlights that the model predicts with high accuracy the CO emissions, as depicted in Figure 93 c) and d). In case of NMHC the model overestimates the cumulated outlet emissions, but it is capable to simulate with high accuracy the LNT performance during the “Cold Start” phase of the RDE. Despite no DeNO_x events were expected during RDE 2 cycle, as depicted from Figure 93 the presence of two steps in CO and NMHC out emissions suggests that two rich events were performed.

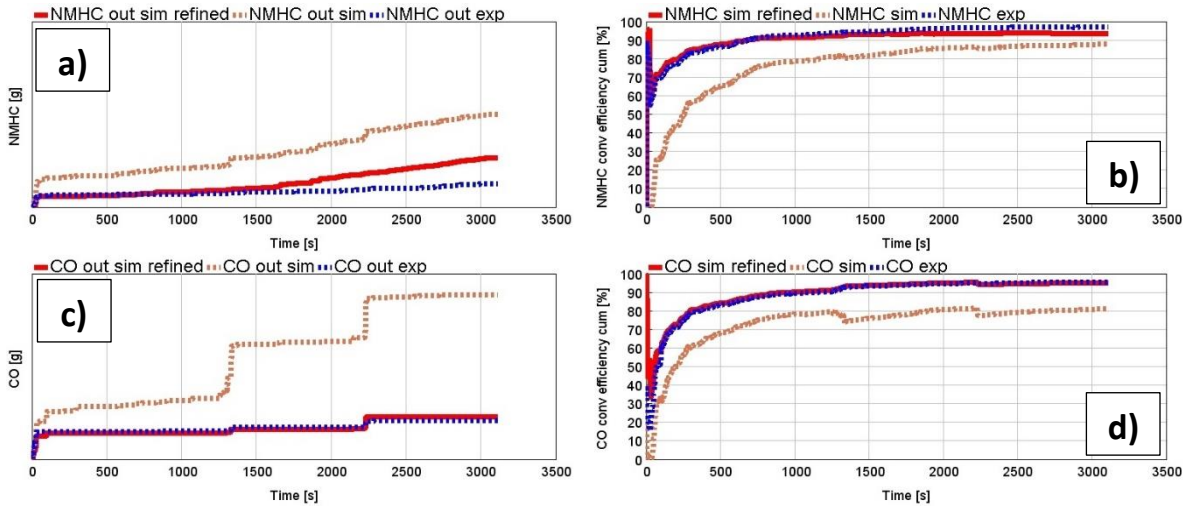


Figure 93 - Simulation results from RDE 2: a) NMHC cumulated emissions, b) NMHC conversion efficiency, c) CO cumulated emissions, d) CO conversion efficiency. The red line represents the simulated value from updated calibration, the orange dashed one is referred to the original calibration and the dashed blue line is referred to the experimental result.

The assessment of NO_x emissions in case of RDE 2 is reported in Figure 94. In this case no corrections were added to the calibration of NO_x . However, the calibration updates applied to CO and NMHC oxidation led to limited changes on model predictions, as highlighted in Figure 94 by the comparison of red line (updated calibration) and the orange dashed line (SGB calibration). NO and NO_2 simulated traces are in good agreement with experimental results for the whole cycle.

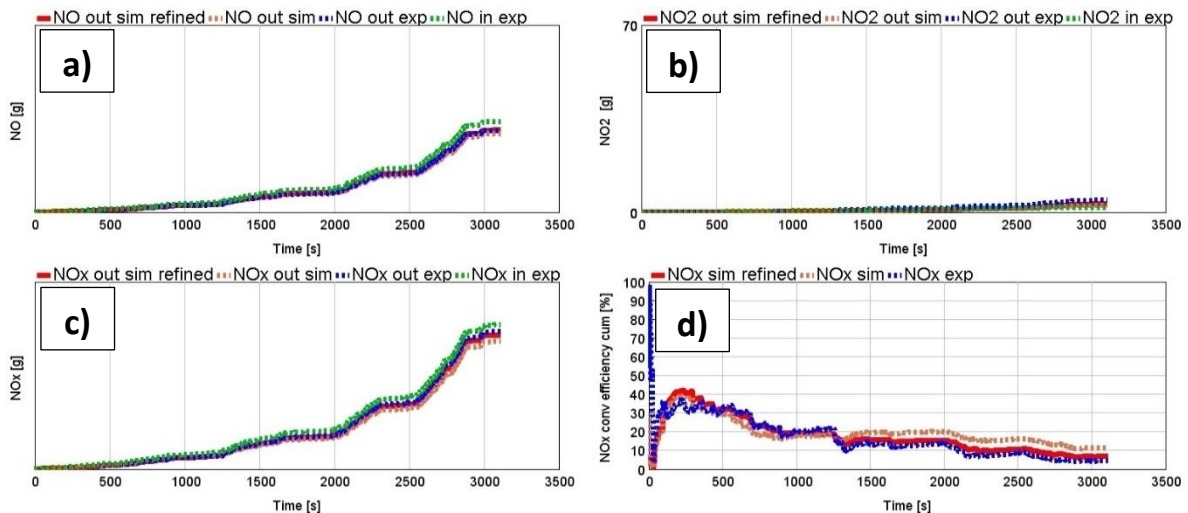


Figure 94 - Simulation results from RDE 2: a) NO cumulated emissions, b) NO_2 cumulated emissions, c) NO_x cumulated emissions, d) NO_x conversion efficiency. The red line represents the simulated value from updated calibration, the orange dashed one is referred to the original calibration, the blue dashed line is referred to the experimental result and the green dashed one to the inlet emissions.

The thermal model validation in case of RDE 3 is reported in Figure 95. As for the previous cases, the model is well correlated with the experimental results.

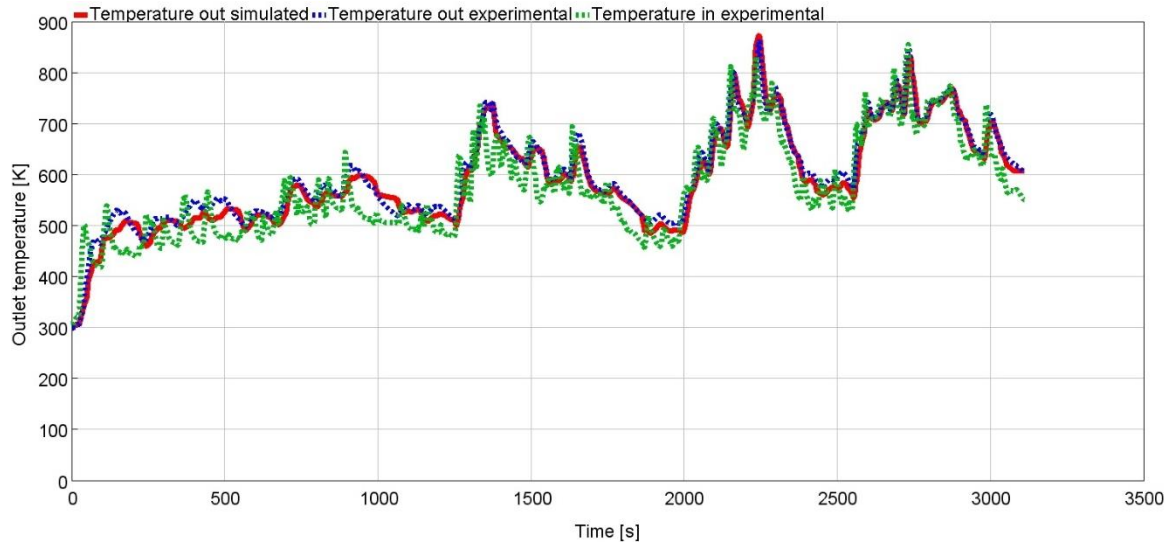


Figure 95 - Simulated and experimental outlet temperature referred to RDE 3. The red line is referred to the simulated trace, the blue dashed line to the experimental one and the green dashed line to the catalyst inlet temperature.

The comparison between simulated and experimental outlet NMHC and CO emissions is reported in Figure 96. The model overestimates both the conversion efficiency during the “Cold Start” for both CO and NMHC. The model estimates equivalent conversion efficiencies to the previous RDE case (Figure 93).

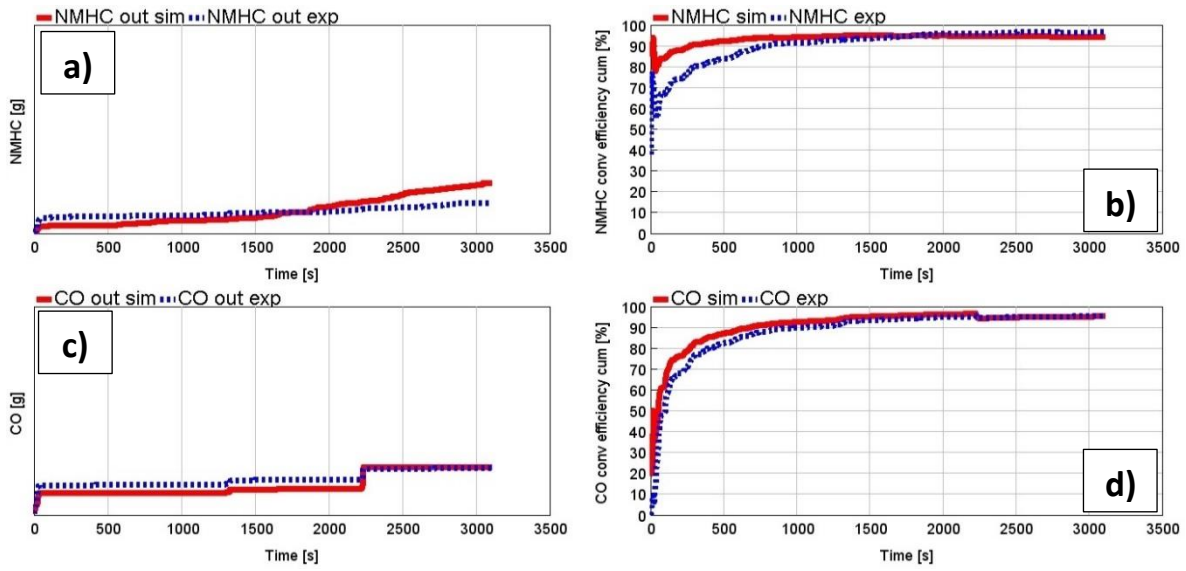


Figure 96 - Simulation results from RDE 3: a) NMHC cumulated emissions, b) NMHC conversion efficiency, c) CO cumulated emissions, d) CO conversion efficiency. The red line represents the simulated value and the blue dashed one is referred to the experimental result.

The model prediction of NO_x emissions in case of RDE 3 is reported in Figure 97. As for the previous cases, the cumulated NO_x emissions from simulation are well correlated with the experiments, as confirmed by the NO_x conversion efficiency trace depicted in Figure 97 d). However, the model slightly underestimates the LNT catalytic activity in terms of NO oxidation to NO_2 .

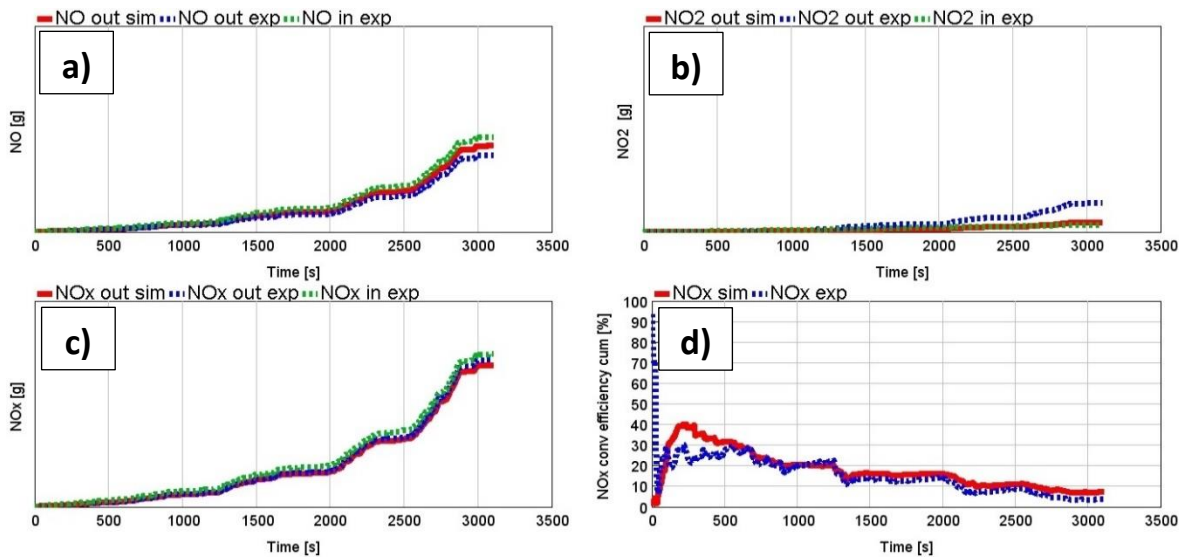


Figure 97 - Simulation results from RDE 3: a) NO cumulated emissions, b) NO_2 cumulated emissions, c) NO_x cumulated emissions, d) NO_x conversion efficiency. The red line represents the simulated value, the blue dashed one is referred to the experimental result and the green dashed line to the inlet emissions.

5 Conclusions

The object of this thesis work was the development of a 1-D simulation model for a LT-LNT catalyst capable to capture the main features of the component behavior on both the thermal and the chemical domain. To this purpose, characterization data measured at the synthetic gas bench and transient data measured at the engine on the real component were used.

The chemical model was developed using a global kinetic approach in GT-Suite, where the catalyst is modelled as a set of chemical reactions and inhibition functions representative of the experimental evidence. A large portion of this project was dedicated to the calibration of the reaction parameters based on SGB data, aiming to the correct implementation of the main physical mechanisms that take place on an LNT catalyst: LO, OSC, NO_x storage and reduction. The final part was dedicated to the calibration refinement based on driving cycles data measured on a chassis-dyno bench.

Even though a large amount of experimental data was available for the development of the chemical model, some important measurements were missing and consequently this introduced some inaccuracies in the model calibration. The most important examples are the unavailability of H₂ measurements at the LNT outlet, the lack of measurements of inlet concentrations in NSR tests and the absence of TPD tests with NO₂/NO_x = 1 for the characterization of the nitrates route. Furthermore, the experimental thermal behavior seemed to be affected by excessive thermal losses in some tests. Another important lesson learned was the unexpected catalytic deactivation mechanism highlighted during long time scale adsorption tests, such as TPDs. This phenomenon caused an important disagreement between TPDs and NSRs adsorption behaviors, likely impacting the calibration of the reduction reactions parameters.

Despite the shortcomings in the experimental data, a reasonable accuracy was obtained in both steady state and transient conditions. In particular, the model was capable to predict with satisfactory accuracy the NO_x storage mechanisms in transient conditions over both the WLTC and RDE cycle. This is also valid in case of CO oxidation. On the contrary, the model shown some inaccuracies in the estimation of NMHC over Hot WLTC.

Based on the insights gained during the development of this study, the next steps of the project should be focused on the calibration of NO_x storage behavior using the NSR tests instead of the TPDs. Since no deactivation mechanisms were detected during NSRs, this should ensure a more reliable characterization of the phenomenon. Furthermore, after the NO_x storage calibration adjustment on the base of NSR tests, other improvements should be focused on the refinement of the model calibration in terms of NO_x reduction, filling the weakness underlined during this study.

6 References

1. Delphi Technologies, “2019-2020 Passenger Car and Light-Duty Vehicles Worldwide emissions standards”. Available on: <https://www.delphi.com/newsroom/press-release/delphi-technologies-releases-2019-2020-worldwide-emissions-standards-booklet>
2. Continental, “Worldwide Emission Standard and Related Regulations, Emission Booklet Continental”, (2019). Available on: https://www.continental-automotive.com/getattachment/8f2dedad-b510-4672-a005-3156f77d1f85/EMISSIONBOOKLET_2019.pdf
3. DieselNet, “United States: Heavy-Duty Onroad Engines”, Web. 15 March 2020. Available on: <https://dieselnet.com/standards/us/hd.php#y2007>.
4. Johnson, T. and Joshi, A., "Review of Vehicle Engine Efficiency and Emissions", SAE Technical Paper 2017-01-0907, 2017, doi:10.4271/2017-01-0907.
5. Claudio Cubito, 2019, “Vehicle Emission and Performance Analysis”. Training Course Material, GM, 30th October.
6. Cubito, Claudio. “A policy-oriented vehicle simulation approach for estimating the CO₂ emissions from Hybrid Light Duty Vehicles.” Diss. Ph. D. Thesis, Politecnico di Torino, Torino, Italy, 2017.
7. Rafigh, Mahsa. "Exhaust Aftertreatment Modeling for Efficient Calibration in Diesel Passenger Car Applications." Politecnico di Torino (2017).
8. Dr. Ameya Joshi, 2020, “Review of Regulations & Technologies pertinent to vehicular emissions”. Corning Webinar, 5th May.
9. Posada, Francisco, Aaron Isenstadt, and Huzeifa Badshah. "Estimated cost of diesel emission-control technology to meet future California low NO." (2020).
10. Ji, Yaying, et al. "Pd-promoted WO₃-ZrO₂ for low temperature NO_x storage." *Applied Catalysis B: Environmental* 264 (2020): 118499.
11. Ji, Yaying, Shuli Bai, and Mark Crocker. "Al₂O₃-based passive NO_x adsorbents for low temperature applications." *Applied Catalysis B: Environmental* 170 (2015): 283-292.

12. Theis, Joseph R., and Christine K. Lambert. "*Mechanistic assessment of low temperature NO_x adsorbers for cold start NO_x control on diesel engines.*" *Catalysis Today* 320 (2019): 181-195.
13. Vaclavik, Marek, et al. "*Effect of diffusion limitation on the performance of multi-layer oxidation and lean NO_x trap catalysts.*" *Catalysis Today* 273 (2016): 112-120.
14. Sharp, C., Webb, C., Neely, G., Sarlashkar, J. et al., "*Achieving Ultra Low NO_x Emissions Levels with a 2017 Heavy-Duty On-Highway TC Diesel Engine and an Advanced Technology Emissions System - NO_x Management Strategies*", SAE Int. J. Engines 10(4):2017, doi:10.4271/2017-01-0958.
15. Johnson, T. and Joshi, A., "*Review of Vehicle Engine Efficiency and Emissions*", SAE Technical Paper 2017-01-0907, 2017, doi:10.4271/2017-01-0907.
16. Pereda-Ayo, Beñat, and Juan R. González-Velasco. "*NO_x storage and reduction for diesel engine exhaust aftertreatment.*" *Diesel Engine—Combustion Emissions and Condition Monitoring*; Bari, S., Ed (2013): 161-196.
17. W. Addy Majewski, "*NO_x Adsorbers*". DieselNet, February 2020 (last revision). Web. 15 July 2020.
Available on: https://dieselnet.com/tech/cat_nox-trap.php
18. Epling, William S., et al. "*Overview of the fundamental reactions and degradation mechanisms of NO_x storage/reduction catalysts.*" *Catalysis Reviews* 46.2 (2004): 163-245.
19. Millo, Federico, et al. "*Modeling NO_x Storage and Reduction for a Diesel Automotive Catalyst Based on Synthetic Gas Bench Experiments.*" *Industrial & Engineering Chemistry Research* 57.37 (2018): 12335-12351.
20. Mahzoul, H., J. F. Brillhac, and P. Gilot. "*Experimental and mechanistic study of NO_x adsorption over NO_x trap catalysts.*" *Applied Catalysis B: Environmental* 20.1 (1999): 47-55.
21. Xu, Jin, Michael P. Harold, and Vemuri Balakotaiah. "*Modeling the effects of Pt loading on NO_x storage on Pt/BaO/Al₂O₃ catalysts.*" *Applied Catalysis B: Environmental* 104.3-4 (2011): 305-315.
22. Lindholm, Anna, et al. "*Detailed kinetic modeling of NO_x storage and reduction with hydrogen as the reducing agent and in the presence of CO₂ and H₂O over a Pt/Ba/Al catalyst.*" *Journal of catalysis* 258.1 (2008): 273-288.

23. Nova, Isabella, et al. "On the dynamic behavior of "NO_x-storage/reduction" Pt–Ba/Al₂O₃ catalyst." *Catalysis Today* 75.1-4 (2002): 431-437.
24. Koop, Jan, and Olaf Deutschmann. "Modeling and simulation of NO_x abatement with storage/reduction catalysts for lean burn and diesel engines". No. 2007-01-1142. SAE Technical Paper, 2007.
25. Nova, Isabella, et al. "NO_x adsorption study over Pt–Ba/alumina catalysts: FT-IR and pulse experiments." *Journal of catalysis* 222.2 (2004): 377-388.
26. Kim, Hakyong, "Characterizing Monolithic Lean NO_x Trap Catalysts Using A Bench-Flow Reactor." Master's Thesis, University of Tennessee, 2006.
27. Katare, Santhoji R., and Paul M. Laing. "Hydrogen in diesel exhaust: effect on diesel oxidation catalyst flow reactor experiments and model predictions." *SAE International Journal of Fuels and Lubricants* 2.1 (2009): 605-611.
28. Kočí, Petr, et al. "Global kinetic model for the regeneration of NO_x storage catalyst with CO, H₂ and C₃H₆ in the presence of CO₂ and H₂O." *Catalysis today* 147 (2009): S257-S264.
29. Nova, Isabella, Luca Lietti, and Pio Forzatti. "Mechanistic aspects of the reduction of stored NO_x over Pt–Ba/Al₂O₃ lean NO_x trap systems." *Catalysis Today* 136.1-2 (2008): 128-135.
30. Kočí, Petr, et al. "Dynamics and selectivity of NO_x reduction in NO_x storage catalytic monolith." *Catalysis Today* 137.2-4 (2008): 253-260.
31. DiGiulio, Christopher D., et al. "NH₃ formation over a lean NO_x trap (LNT) system: Effects of lean/rich cycle timing and temperature." *Applied Catalysis B: Environmental* 147 (2014): 698-710.
32. Li, Junhui, et al. "Impact of Rh Oxidation State on NO_x Reduction Performance of Multi-Component Lean NO_x Trap (LNT) Catalyst." *SAE International Journal of Engines* 9.3 (2016): 1615-1622.
33. Bedrane, Sumeya, Claude Descorme, and Daniel Duprez. "Investigation of the oxygen storage process on ceria-and ceria–zirconia-supported catalysts." *Catalysis Today* 75.1-4 (2002): 401-405.
34. Khossusi, Touraj, Geoffrey McCullough, and Roy Douglas. "Investigation of oxygen storage in three-way automotive catalysts." *SAE transactions* (2004): 805-817.

35. Epling, William S., et al. "Overview of the fundamental reactions and degradation mechanisms of NO_x storage/reduction catalysts." *Catalysis Reviews* 46.2 (2004): 163-245.
36. Ji, Yaying, Todd J. Toops, and Mark Crocker. "Effect of ceria on the sulfation and desulfation characteristics of a model lean NO_x trap catalyst." *Catalysis letters* 127.1-2 (2009): 55-62.
37. Koop, Jan, and Olaf Deutschmann. "Modeling and simulation of NO_x abatement with storage/reduction catalysts for lean burn and diesel engines". No. 2007-01-1142. SAE Technical Paper, 2007.
38. Yang, Liuhanzi, et al. "Control technologies for euro 6 Diesel passenger cars." *Communications* 49.30 (2015): 847129-102.
39. Spessa E., "Controllo delle emissioni inquinanti" course. Politecnico di Torino, 2018.
40. GT-SUITE v2018, "Aftertreatment calibration manual". Gamma Technologies, 2018.
41. GT-SUITE v2018, *Aftertreatment 1D model examples*. Gamma Technologies, 2018.
42. Hauff, K., et al. "Platinum oxide formation and reduction during NO oxidation on a diesel oxidation catalyst—Experimental results." *Applied Catalysis B: Environmental* 123 (2012): 107-116.
43. Schmeißer, V., et al. "Experimental results concerning the role of Pt, Rh, Ba, Ce and Al_2O_3 on NO_x -storage catalyst behaviour." *Topics in Catalysis* 42.1-4 (2007): 15-19.
44. Fridell, Erik, et al. "Platinum oxidation and sulphur deactivation in NO_x storage catalysts." *Topics in catalysis* 30.1-4 (2004): 143-146.